

Intercalibration of QuikSCAT and OSCAT Land Backscatter

John Colin Barrus

A thesis submitted to the faculty of  
Brigham Young University  
in partial fulfillment of the requirements for the degree of  
Master of Science

David G. Long, Chair  
Richard W. Christiansen  
Dah Jye Lee

Department of Electrical and Computer Engineering  
Brigham Young University  
December 2013

Copyright © 2013 John Colin Barrus

All Rights Reserved

## ABSTRACT

### Intercalibration of QuikSCAT and OSCAT Land Backscatter

John Colin Barrus

Department of Electrical and Computer Engineering

Master of Science

The Ku-band SeaWinds-on-QuikSCAT scatterometer (QuikSCAT) operated continuously from 1999 to 2009. Though its primary mission was to estimate global ocean winds, QuikSCAT has proven useful in a variety of geophysical studies using land backscatter measurements. The end of the primary QuikSCAT mission in 2009 has prompted interest for continuing the QuikSCAT land dataset with other scatterometers. The Oceansat-2 scatterometer (OSCAT), launched in 2009, is a viable candidate for continuing the QuikSCAT time series because of the similarities of both sensors in function and design. An important difference in the sensors is that they operate at slightly different incidence angles. Continuing the time series requires careful cross-calibration of the two sensors. Because the sensor datasets overlapped by only a few weeks in late 2009, the amount of simultaneous data is insufficient to describe temporal and locational variations in the relative calibration, or difference between QuikSCAT and OSCAT measurements. To overcome this limitation, we perform direct and model-based comparisons of temporally-disjoint QuikSCAT and OSCAT global land measurements to describe the relative calibration. Using homogeneous rainforest targets, we also identify drift and azimuthal biases in the OSCAT dataset and present suggestions for removing them. The relative calibration is found to vary locationally by several tenths of a decibel over certain regions. Evidence is presented that suggests the relative calibration is dependent on environmental factors such as vegetation density and freeze-thaw status and results from the different incidence angles of the measurements.

Keywords: QuikSCAT, OSCAT, scatterometer, calibration

## ACKNOWLEDGMENTS

Many people have helped me in my education and to complete this thesis. A special thanks to Dr. Long for his advice in both research and life. Thank you to the rest of the faculty of the Electrical Engineering Department at BYU. I am blessed to have gained an education from you. Lastly, thank you to my family for the love and support.

# Table of Contents

<b>List of Tables</b>	<b>vii</b>
<b>List of Figures</b>	<b>viii</b>
<b>1 Introduction</b>	<b>1</b>
1.1 Research Outline . . . . .	3
1.2 Motivation . . . . .	4
1.3 Thesis Organization . . . . .	4
<b>2 Background</b>	<b>6</b>
2.1 Scatterometry . . . . .	6
2.2 Radar Scattering . . . . .	7
2.3 QuikSCAT and OSCAT Scatterometers . . . . .	9
2.4 Datasets . . . . .	11
2.5 Scatterometer Image Reconstruction . . . . .	12
2.6 Summary . . . . .	13
<b>3 Intercalibration Model and Methodology</b>	<b>14</b>
3.1 Measurement Model . . . . .	14
3.2 Methodology of Estimating $G'$ . . . . .	16
3.3 Contributions to $F$ . . . . .	19
3.4 Methodology of Estimating $F$ . . . . .	21

3.4.1	Methods . . . . .	21
3.5	Summary . . . . .	22
<b>4</b>	<b>OSCAT Measurement Bias</b>	<b>24</b>
4.1	Inter-annual Drift . . . . .	24
4.2	Azimuthal Bias . . . . .	26
4.2.1	Temporal Variation . . . . .	28
4.2.2	Locational Variation . . . . .	30
4.2.3	Correction . . . . .	34
4.3	Summary . . . . .	36
<b>5</b>	<b>QuikSCAT/OSCAT Relative Calibration</b>	<b>38</b>
5.1	Direct Comparison . . . . .	39
5.1.1	Short-Term Comparison . . . . .	39
5.1.2	Long-Term Comparison . . . . .	43
5.2	Model-Based Approach . . . . .	51
5.2.1	Seasonal Effects of Vegetation on Relative Calibration . . . . .	51
5.2.2	Effects of Freeze-Thaw on Relative Calibration . . . . .	59
5.3	Summary . . . . .	64
<b>6</b>	<b>Conclusion</b>	<b>66</b>
6.1	Contributions . . . . .	67
6.2	Future Work . . . . .	68
	<b>Bibliography</b>	<b>70</b>
<b>A</b>	<b>Geographic Regions that Exhibit Anisotropy and Diurnal Phenomena</b>	<b>75</b>

A.1	Procedure . . . . .	75
A.2	Anisotropic Regions . . . . .	76
A.3	Regions with Diurnal Phenomena . . . . .	76
A.4	Summary . . . . .	76
<b>B</b>	<b>QuikSCAT Azimuth Response</b>	<b>80</b>
B.1	Temporal and Locational Variability . . . . .	80
B.2	Summary . . . . .	80

## List of Tables

2.1	Comparative summary of major characteristics of QuikSCAT and OSCAT . . . . .	10
2.2	Versions of OSCAT L1B data and their temporal coverage. . . . .	11
3.1	Statistics of QuikSCAT backscatter over calibration targets. . . . .	19
4.1	Drop in OSCAT backscatter between 2010 and 2012. . . . .	25
4.2	2012 OSCAT mean and year calibration offsets. . . . .	26
4.3	Comparison of Fourier model orders. . . . .	28
4.4	Global 2012 Fourier model coefficients. . . . .	35
5.1	Regions of interest for short-term direct comparison. . . . .	40
5.2	Relative calibration numbers for several regions. . . . .	51
5.3	Regions of interest for vegetation study. . . . .	53
5.4	Correlation coefficients between NDVI and backscatter. . . . .	56
5.5	Summary of H-pol relative calibration as a function of NDVI. . . . .	58
5.6	Summary of V-pol relative calibration as a function of NDVI. . . . .	58
5.7	Regions of interest for freeze-thaw study. . . . .	60

## List of Figures

2.1	An example of the relationship between backscatter and incidence angle. . .	8
2.2	OSCAT and QuikSCAT observation geometry. . . . .	9
2.3	Approximate 3-dB contours of OSCAT slice measurements. . . . .	12
2.4	Example SIR images of South America generated by QuikSCAT and OSCAT.	13
3.1	Regional data selection masks. . . . .	17
3.2	Azimuthal response of QuikSCAT over the Amazon. . . . .	18
3.3	20-day mean QuikSCAT $\sigma^0$ over the Amazon. . . . .	18
4.1	Mean and standard deviation of OSCAT $\sigma^0$ over the Amazon. . . . .	25
4.2	Azimuth response of OSCAT over the Amazon. . . . .	27
4.3	Azimuth bias of OSCAT 2012 data over Amazon. . . . .	29
4.4	Inter-annual variation of OSCAT azimuth bias. . . . .	30
4.5	Locational variation of OSCAT azimuth bias. . . . .	31
4.6	Data selection mask over Siberia. . . . .	32
4.7	Locational variation of Fourier model coefficients. . . . .	33
4.8	Uncorrected and corrected OSCAT 2012 backscatter. . . . .	35
4.9	Uncorrected, corrected and differenced OSCAT SIR images. . . . .	36
5.1	Regions of interest for short-term direct comparison. . . . .	40
5.2	OSCAT and QuikSCAT backscatter over regions of interest. . . . .	41

5.3	Difference in backscatter over regions of interest. . . . .	42
5.4	Global difference of QuikSCAT and OSCAT H-pol backscatter. . . . .	45
5.5	Global difference of QuikSCAT and OSCAT V-pol backscatter. . . . .	46
5.6	Global difference of QuikSCAT and corrected OSCAT H-pol backscatter. . .	47
5.7	Global difference of QuikSCAT and corrected OSCAT V-pol backscatter. . .	48
5.8	Inter-annual variability of global QuikSCAT H-pol backscatter. . . . .	49
5.9	Inter-annual variability of global QuikSCAT V-pol backscatter. . . . .	50
5.10	Regions of interest for vegetation study. . . . .	52
5.11	Seasonal NDVI response for region 6. . . . .	55
5.12	Seasonal backscatter mean for region 6. . . . .	55
5.13	Seasonal backscatter variability for region 6. . . . .	55
5.14	Scatterplots of NDVI and sensor backscatter. . . . .	57
5.15	Regions of interest for freeze-thaw study. . . . .	60
5.16	QuikSCAT and OSCAT backscatter according to freeze-thaw state. . . . .	62
5.17	Difference in backscatter according to freeze-thaw state. . . . .	63
A.1	Map of QuikSCAT H-pol anisotropy. . . . .	77
A.2	Map of QuikSCAT V-pol anisotropy. . . . .	78
A.3	Maps of QuikSCAT diurnal behavior. . . . .	79
B.1	Seasonal variations of QuikSCAT azimuth response. . . . .	81
B.2	Inter-annual variations of QuikSCAT azimuth response. . . . .	82
B.3	Locational variations in QuikSCAT azimuth response. . . . .	83

# Chapter 1

## Introduction

For the past 35 years, spaceborne scatterometers have provided useful datasets of radar backscatter measurements to the scientific community. These datasets range from a few months to many years in length, depending on the sensor. From these measurements, a number of important geophysical parameters can be inferred, such as ocean wind speed [1], sea ice extent and age [2, 3], and soil moisture content [4].

To increase the scientific value of the scatterometer datasets and promote a consistent and continuous record, intercalibration between the various datasets is warranted [5]. We define intercalibration as the quantification of biases between sensor measurements. By removing intersensor biases, a consistent dataset is created which spans the lifetimes of the individual sensors, thereby facilitating long-term geophysical studies.

Several land and ocean-based techniques exist for scatterometer intercalibration. These methods were first developed to intercalibrate multiple beams aboard a single instrument. Land-based techniques include comparing backscatter measurements over homogeneous, isotropic land targets such as tropical rainforests to determine relative biases between the individual beams of fan-beam scatterometers [6–9]. Ocean-based techniques include using open-ocean backscatter measurements and wind-to-backscatter geophysical model functions (GMF) to identify relative fan-beam biases [10, 11]. These techniques have become standard practice for post-launch calibration and validation of scatterometer data. Although land and ocean-based methods do not provide information about the absolute calibration of an instrument, they ensure consistency of measurements among different beams, which is essential for accurate wind retrieval and land studies.

More recently, work has been done to intercalibrate scatterometers operating on different platforms. For example, land-based techniques were employed to intercalibrate

NASA’s Ku-band SeaWinds-on-QuikSCAT (QuikSCAT) and SeaWinds-on-ADEOS-2 (SeaWinds) scatterometers [12]. Consistency between the Seawinds datasets has enabled them to be used in tandem for several studies [13–15]. Both land and ocean-based techniques also aided in intercalibrating the C-band ERS-1, ERS-2, and ASCAT scatterometers [16]. Cross-platform intercalibrations such as these are similar in that they identify biases between scatterometers which share a common range of incidence angles. Specifically, SeaWinds and QuikSCAT are pencil-beam scatterometers that operate at identical incidence angles, and the ERS and ASCAT scatterometers have fan beams that cover a range of common incidence angles. Because of this commonality, identifying biases that result from instrument gain differences is a relatively straightforward task.

The process of intercalibration is more difficult for scatterometers that do not have common incidence angles. The Oceansat-2 scatterometer (known as OSCAT), for example, is a Ku-band scatterometer similar in operation and design to QuikSCAT, with the exception of a difference in incidence angle of approximately 3 degrees for each beam. A QuikSCAT/OSCAT intercalibration must consider not only the measurement biases of the individual sensors, but also the dependence of backscatter on incidence angle, or incidence response, of the calibration target. Moreover, the appropriate choice of intercalibration technique depends on the desired output. For example, ocean-based techniques are appropriate if the desired output is a consistent wind vector dataset between the sensors. This is because the GMF used in intercalibration generally accounts for measurements made at different incidence angles. Land-based techniques may not be appropriate for generating a consistent wind vector dataset since the incidence response of the land calibration target can differ over time and location. Similarly, if the desired output is a consistent set of over-land backscatter measurements, land-based techniques are more appropriate since ocean-based techniques assume an incidence response dependent only on ocean wind.

Through its unparalleled 10 years of continuous operation from 1999 to 2009, QuikSCAT has proven its utility in numerous land and ocean studies [17–20]. In contrast, OSCAT is a relatively new sensor, launched in 2009 shortly before the end of QuikSCAT’s mission. Intercalibration of the QuikSCAT and OSCAT datasets is a worthwhile goal as it may extend the utility of OSCAT data and provide the scientific community with a consistent, multi-

decadal Ku-band dataset to facilitate geophysical research. Previous work has been done to intercalibrate QuikSCAT and OSCAT backscatter. Jaruwatanadilok and Stiles [21] sorted ocean backscatter data from each sensor by wind speed and direction and compared the resulting histograms to determine the calibration as a function of wind. Because the incidence response and scattering characteristics of the ocean differs from those of land, their results are generally not applicable to land measurements. Bhowmick, et al. performed an initial comparison of QuikSCAT and OSCAT land measurements over stable, homogeneous land regions [22]. The study used data from the one-month overlap of the sensor mission lives in 2009. The results showed consistency between QuikSCAT and OSCAT land measurements within  $\pm 0.25$  dB over the study regions, though because of the limited data, temporal and spatial variations in the calibration were not considered in detail.

## 1.1 Research Outline

A more thorough understanding of the differences between QuikSCAT and OSCAT land backscatter will facilitate increased use of OSCAT data in geophysical research and continue the climate record started by QuikSCAT. In this thesis, we utilize land-based techniques for intercalibrating QuikSCAT and OSCAT backscatter. We build on the work of previous land calibration studies [23] and explore possible temporal and locational variation in the relative calibration between sensors. To overcome the limitation of a short temporal overlap of QuikSCAT and OSCAT data, we use temporally-disjoint data from the entire sensor datasets in statistical comparisons to determine the relative calibration.

As part of the process of intercalibration, we first consider measurement error in each sensor’s dataset. QuikSCAT has been found to be well calibrated so we assume that no corrections to its data are needed [24, 25]. In contrast, previous research has noted several inconsistencies in OSCAT backscatter data including an azimuth-dependent bias and a time-dependent drift [21, 22]. Land-based techniques are especially useful in identifying these errors and describing their temporal and locational variability. We examine the OSCAT-measured backscatter over homogeneous, isotropic rainforest targets. Using the corresponding QuikSCAT backscatter data as a reference, we detect temporal and locational

dependence in the OSCAT measurement errors. Low-order models are used to describe the error and aid in its removal.

In addition to the measurement errors inherent in the OSCAT system, we consider several variables that give rise to the observed differences in QuikSCAT and OSCAT backscatter. Among these are differences in sensor incidence and azimuth angles, diurnal phenomena in surface scattering, and the inherent temporal and locational variability of the surface due to seasonal effects and differences in terrain. To estimate the relative calibration between sensor measurements, we make direct and model-based comparisons of the data. Depending on the region and comparison method, the temporal variation in the relative calibration may be resolved.

## 1.2 Motivation

The motivation for this thesis is to incorporate high-resolution, OSCAT backscatter images into the NASA Scatterometer Climate Record Pathfinder (SCP) project located at <http://www.scp.byu.edu>. The SCP contains land backscatter images derived from other sensors such as the NASA Scatterometer (NSCAT), SeaWinds, ERS, and ASCAT. The addition of OSCAT image data will contribute to the large Ku-band image set already available. Knowledge of the relative calibration, or difference, between QuikSCAT and OSCAT data may facilitate new and continued use of the image sets in geophysical research and possibly encourage the use of the image sets in tandem.

## 1.3 Thesis Organization

This thesis is organized as follows: Chapter 2 provides background on the fundamentals of scatterometry, the operation and design of the QuikSCAT and OSCAT scatterometers, as well as the datasets that are used in intercalibration procedures. Chapter 3 presents a measurement model relating QuikSCAT and OSCAT backscatter, and describes the methods of intercalibration. Here, we identify several variables which give rise to differences in the sensors' backscatter. In Chapter 4, we identify measurement biases in OSCAT backscatter data and examine their temporal and locational variation using homogeneous, isotropic land targets. Corrections to the OSCAT data are suggested which make the dataset more

self-consistent and offer improvements in backscatter imagery. In Chapter 5, direct and model-based comparisons of QuikSCAT and OSCAT backscatter are performed and seasonal and locational trends in the relative calibration are noted. A conclusion is given in Chapter 6.

## Chapter 2

### Background

This chapter presents background material for understanding the work presented in this thesis. We review fundamental concepts in scatterometry, scattering characteristics of the Earth, the function and design of the QuikSCAT and OSCAT scatterometers, and details about the datasets used in this thesis.

#### 2.1 Scatterometry

A scatterometer is a radar instrument that transmits successive pulses of electromagnetic radiation toward the Earth’s surface and measures the returned power. From these measurements, a number of important geophysical parameters can be estimated. The primary purpose of spaceborne scatterometers is to estimate ocean wind vectors. However, the design of the scatterometer often makes it well suited for other applications. For example, the active nature of the sensor and the frequency of operation generally allow accurate measurement of the surface under cloudy or night-time conditions. In addition, the orbit and swath size allow frequent, global coverage. Many scatterometers are also equipped with multiple beams to measure the surface at different azimuth and elevation angles.

The relationship between the transmitted and received power by the scatterometer is described in the monostatic radar equation as

$$P_r = \frac{P_t \lambda^2}{(4\pi)^3 L} \int_A \frac{G^2 \sigma^0}{R^4} dA, \quad (2.1)$$

where  $P_r$  is the received power,  $P_t$  is the transmitted power,  $\lambda$  is the radiation wavelength,  $G$  is the antenna gain,  $R$  is the range to the Earth’s surface,  $A$  is the area illuminated by the incident radiation, and  $L$  is the system loss.  $\sigma^0$  is the normalized radar cross section

(NRCS) of the surface. It is a measure of how well the incident radiation is reflected back to the transmitter. If  $\sigma^0$  is assumed constant over the illuminated area, it can be expressed as

$$\sigma^0 = \frac{P_r}{X}, \quad (2.2)$$

where  $X$  is

$$X = \frac{P_t \lambda^2}{(4\pi)^3 L} \int_A \frac{G^2}{R^4} dA. \quad (2.3)$$

Accurate measurement of the received power and knowledge of the parameters of  $X$  allow  $\sigma^0$  to be calculated.

There are several factors that add uncertainty to the measured  $\sigma^0$ . Since a high-level of measurement accuracy is required for wind retrieval, extensive pre- and post-launch calibration operations are necessary to identify and reduce sources of measurement variability. Multiplicative communication noise from the surroundings adds variability to measured  $\sigma^0$ . The noise is a function of the scatterometer design parameters and cannot be removed by calibration [26]. The inherent variability of Earth's surface also contributes to the uncertainty in  $\sigma^0$ . Some of this variability can be modeled to reduce the total variability in the measurements [8]. Systematic errors in the determination of radar equation parameters translate into measurement biases in  $\sigma^0$ . The primary objective of calibration is to identify and remove these measurement biases.

## 2.2 Radar Scattering

There are many factors that affect  $\sigma^0$ , including the wavelength and polarization of the radiation, as well as the dielectric constant, roughness, and orientation of the surface with respect to the scatterometer. Regions that exhibit rough surface or volume scattering typically have large  $\sigma^0$  values. Examples of such regions include tropical rainforests and Greenland's dry snow zone. Smooth, specular surfaces such as sandy deserts or water generally have small  $\sigma^0$  values. For many regions, the dielectric constant and other scattering characteristics of Earth surfaces exhibit temporal variation. For example, a large diurnal change in backscatter occurs over the tropical rainforests because of changes in dew concentration [27]. In high latitudes, backscatter is sensitive to freeze-thaw transitions where

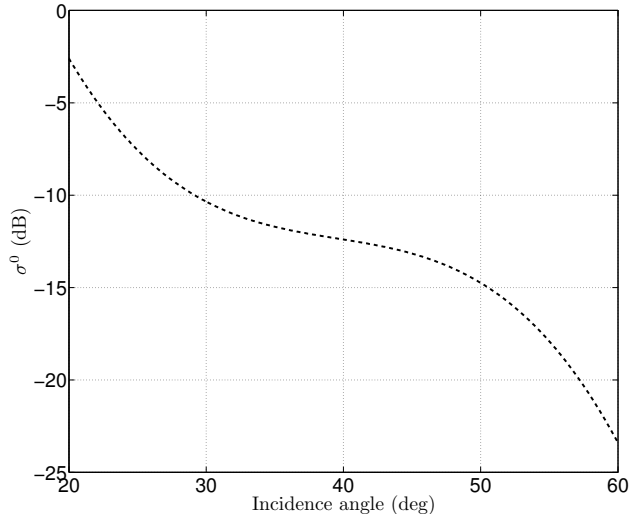


**Figure 2.1:** An example of the generally smooth relationship between the backscatter and incidence angle.

changes in water phase and associated dielectric properties occur [28]. Seasonal vegetation changes can lead to annual cycles in backscatter as well [4].

Many Earth surfaces exhibit azimuthal and incidence dependence in radar backscatter. For example, regions in the Sahara desert and Antarctica exhibit anisotropy, or backscatter that is strongly dependent on azimuth angle [29, 30]. In contrast, tropical rainforests are azimuthally independent, or isotropic [7]. For most land surfaces,  $\sigma^0$  generally decreases smoothly with increasing incidence angle  $\theta$ , as shown in Figure 2.1. This relationship is frequently modeled as a polynomial centered at a nominal incidence angle [8]. For example, the incidence angle dependence of  $\sigma^0$  centered at  $40^\circ$  may be modeled as

$$\sigma^0(\theta) = \mathcal{A} + \mathcal{B}\vartheta + \mathcal{C}\vartheta^2 + \mathcal{D}\vartheta^3 + \dots, \quad (2.4)$$

where  $\vartheta = \theta - 40^\circ$ . The coefficients  $\mathcal{A}, \mathcal{B}, \mathcal{C}, \mathcal{D}, \dots$ , are dependent on the scattering characteristics of the region being measured [31, 32]. The azimuth and incidence dependence of backscatter is especially important over the ocean. Knowledge of the azimuth and incidence responses of the ocean as a function of wind speed and direction allows wind vectors to be estimated from backscatter measurements [1].

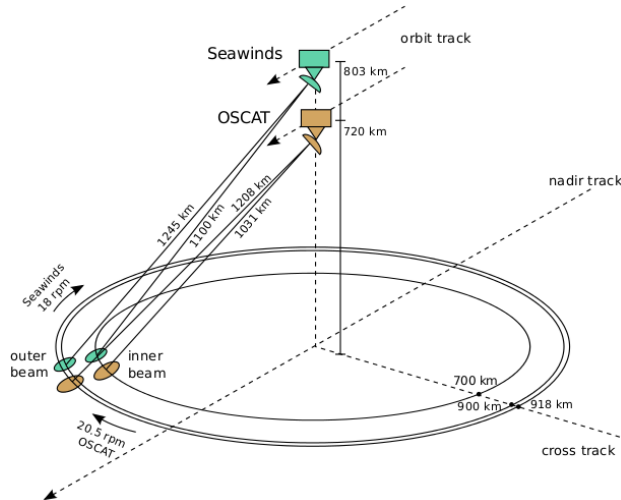


**Figure 2.2:** OSCAT and QuikSCAT observation geometry. OSCAT is depicted in orange and QuikSCAT is depicted in green [33].

### 2.3 QuikSCAT and OSCAT Scatterometers

The QuikSCAT scatterometer was launched by NASA in 1999 and operated continuously until 2009. It is a conically-scanning pencil-beam scatterometer operating in the Ku band. Its rotating 1-meter dish antenna produced a HH-polarized beam at  $46^\circ$  incidence and a VV-polarized beam at  $54^\circ$  incidence. The instrument holds a sun-synchronous orbit at a height of 803 km with a repeat cycle of four days and equator crossings at approximately 6 A.M. (ascending) and 6 P.M. (descending) local time. The orbit and swath size allowed 92% global coverage every 24 hours. The antenna rotated at 18 rpm with a pulse repetition frequency (PRF) of 185 Hz between beams. Each pulse yields a  $\sigma^0$  “egg” measurement, so called because of the footprint shape on the Earth’s surface. The two-way egg size is roughly 25 km in azimuth and 35 km in elevation [34]. Through range and Doppler processing, higher resolution “slice” measurements are extracted from each pulse. Due to QuikSCAT’s conically-scanning operation, each location within its swath was measured up to four times, with fore and aft measurements of both beams. The antenna rotation and PRF allowed dense, overlapping sampling of the surface.

QuikSCAT’s primary mission ended in November 2009 when the antenna rotation system failed. The sensor exceeded its original three-year mission life requirement by seven years [34]. The radar system continues to operate at a fixed azimuth angle and its mea-

**Table 2.1:** Comparative summary of major characteristics of QuikSCAT and OSCAT [33]

Parameter	QuikSCAT		OSCAT	
Antenna Type	1 m dual-feed parabolic		1 m dual-feed parabolic	
Orbital Period	101 min (14.25 orbits/day)		99.31 min (14.5 orbits/day)	
Equator Crossing	6 A.M./6 P.M.		12 A.M./12 P.M.	
Satellite Altitude	803 km at equator		720 km at equator	
Frequency	13.402 GHz		13.515 GHz	
Wavelength	0.0224 m		0.0221 m	
Scan Rate	18 rpm		20.5 rpm	
PRF (per beam)	92.5 Hz		96.5 Hz	
Start Date	June 19, 1999		Sept. 23, 2009	
End Date	Nov. 23, 2009		—	
	Inner Beam	Outer Beam	Inner Beam	Outer Beam
Polarization	HH	VV	HH	VV
Incidence Angle	46°	54°	49°	57°
Slant Range	1100 km	1245 km	1031 km	1208 km
Swath Width	1400 km	1800 km	1400 km	1836 km
One-way Beamwidth (Az x El)	1.8° x 1.6°	1.7° x 1.4°	1.47° x 1.62°	1.39° x 1.72°
One-way Footprint (km) (Az x El)	35.0 x 44.0	37.0 x 52.0	26.8 x 45.1	29.7 x 68.5

measurements are still being used for calibration purposes [21]. In February, 2013 the antenna rotated for a few days, again providing near global coverage before failing again.

The Oceansat-2 scatterometer was launched by ISRO in late 2009. Its design is similar to that of QuikSCAT, with some notable differences. The instrument orbits lower than QuikSCAT at an altitude of 720 km. The incidence angles of OSCAT’s H-pol and V-pol beams are at 49° and 57° respectively, which is 3° higher than the corresponding QuikSCAT beams. The offsetting altitude and incidence angle differences allow OSCAT to have a similar swath width to that of QuikSCAT. The orbit of OSCAT is sun-synchronous with 12 A.M./12 P.M equator crossings and has a two-day repeat cycle. A visual comparison of the sensors’ geometries is given in Figure 2.2 and their major operating parameters are given in Table 2.1. The orbit and design differences of the sensors contribute to the difference in measured backscatter and are explored in the following chapters.

**Table 2.2:** Currently available OSCAT L1B data versions and their temporal coverage.

Time Range	Available Processing Version
JD 309, 2009 - JD 15, 2010	1.2
JD 16, 2010 - JD 181, 2010	1.3
JD 182, 2010 - JD 273, 2010	no data available
JD 274, 2010 - JD 147 2013	1.3
JD 148, 2013 - present	1.4

## 2.4 Datasets

The OSCAT data used in this thesis are obtained from the National Oceanic and Atmospheric Administration (NOAA). The specific dataset used is the Level 1B (L1B) product. L1B data contains  $\sigma^0$  values and corresponding location, orientation and quality information. Several versions of the data currently exist, which are documented in Table 2.2. As ISRO continues to monitor and validate OSCAT’s measurements, previous versions will be reprocessed to a later version. Given the large temporal coverage of version 1.3, we use it almost exclusively in the analyses in the following chapters. Using the quality information provided in the L1B product, any measurements that are flagged as poor or invalid are excluded from the analyses.

An initial correction is made to the OSCAT L1B data prior to the work in this thesis. Because an offset exists between OSCAT’s antenna pointing angle and the reading of the scan-angle encoder [35], the reported antenna azimuth angle is subject to error. To avoid possible inaccuracies in the reported data, we use an estimate of the antenna azimuth angle derived from the reported footprint number [23]. In plotting the location of measurements with  $0^\circ$  azimuth in relation to the swath, we found the derived angle to be more accurate than the original reported value. The antenna azimuth angle is especially important to the analyses of Chapter 4, where we examine OSCAT measurement bias dependencies on the scan angle. All other information provided in the L1B data is used as reported.

We use the most recent version of QuikSCAT L1B data, also obtained from NOAA. The entire dataset spans the period 1999-2009. The complete years of data from 2000 to 2008 are primarily used in comparisons with OSCAT data. Numerous efforts have been

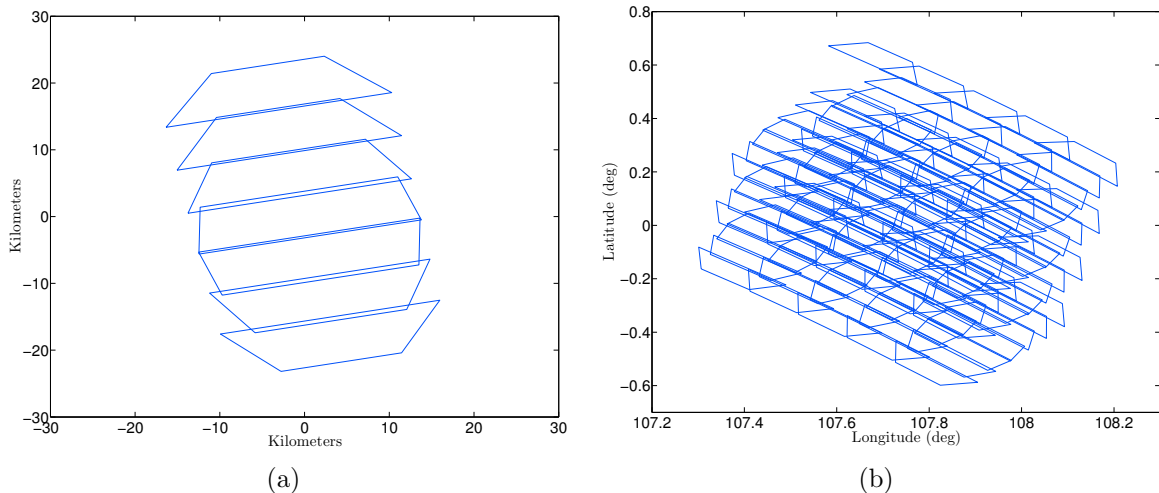


**Figure 2.3:** (a) Approximate 3-dB contours of the slices from an OSCAT measurement. (b) Several overlapping measurements from a swath of OSCAT L1B data.

made to verify and calibrate QuikSCAT  $\sigma^0$  values [24, 25, 34, 36]. We therefore consider it as truth data when comparing it against OSCAT data, and make no efforts to identify internal measurement biases.

Both sensor datasets report egg and slice measurements, however only egg data are used in the analyses that follow. For simplicity, the egg measurements are divided into four groups (“flavors”) depending on the polarization and whether the satellite was in the ascending or descending pass. Where appropriate, analyses are performed on each flavor’s data separately.

## 2.5 Scatterometer Image Reconstruction

The rotation rate and PRF of QuikSCAT and OSCAT enable dense sampling of the Earth’s surface. To illustrate, in Figure 2.3 we show the approximate 3-dB contours of a single OSCAT pulse with individual slices and the overlapping contours of several measurements. The Scatterometer Image Reconstruction (SIR) algorithm can exploit this overlapping nature to achieve finer resolution than the approximate 25-km resolution of the original measurements [37]. The algorithm has been applied to QuikSCAT and OSCAT data to generate  $\sigma^0$  images of land surfaces. Egg images are produced at 4.45 pixel/km resolution and slice images at 2.225 pixel/km resolution. Example images are shown in Figure 2.4.

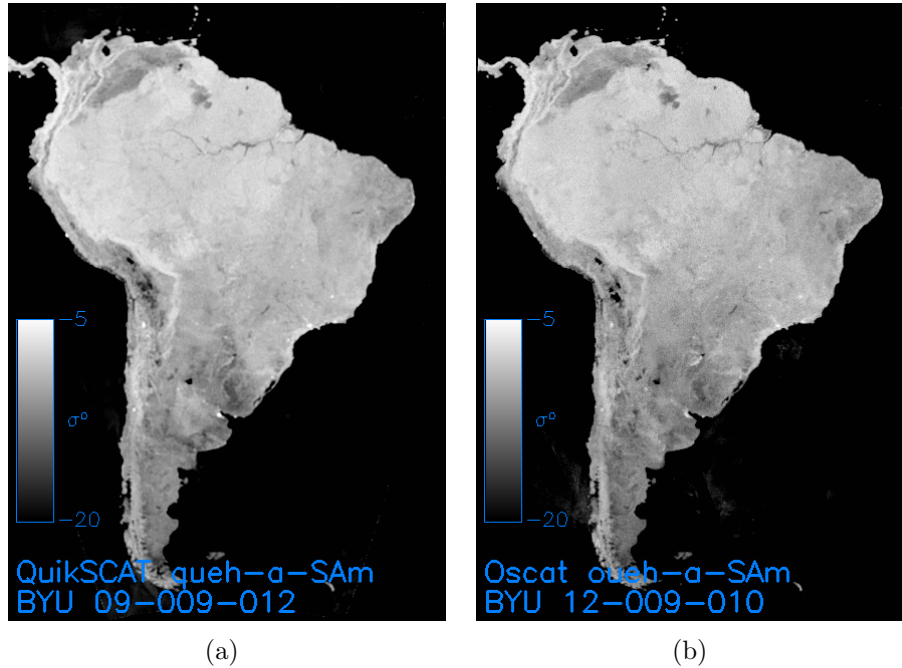


**Figure 2.4:** SIR images of South America generated by (a) QuikSCAT (b) OSCAT. H-pol egg data from ascending and descending passes were used to generate the images.

The SIR algorithm has been applied to the datasets of several scatterometers to produce high-resolution  $\sigma^0$  images. The images sets are available at the SCP website.

SIR images are used in this thesis for data mask formation and illustrative purposes, while all statistical comparisons of QuikSCAT and OSCAT measurements are performed using egg measurements. Though QuikSCAT and OSCAT SIR images are not analyzed directly, the conclusions drawn from this thesis have implications on how OSCAT SIR data may be used, especially when comparisons with QuikSCAT SIR data are made.

## 2.6 Summary

We have reviewed background information important for this thesis. Understanding the radar equation and the operation of QuikSCAT and OSCAT is helpful in Chapter 4 where measurement errors of the OSCAT system are examined. The principles of scatterometry, including the incidence and azimuthal dependencies of  $\sigma^0$  are important for understanding the causes of differences in the sensors' backscatter measurements. These differences are discussed in Chapters 3 and 5 and Appendix A.

## Chapter 3

### Intercalibration Model and Methodology

A primary objective in scatterometer intercalibration is to quantify and remove the relative bias, or difference, between sensor measurements [5]. The ideal scenario for intercalibration includes data produced from two sensors with identical measurement geometries, orbit tracks and measurement times (i.e. coincident data). In this scenario, measurement bias can be attributed to differences in the sensors themselves, rather than the targets being measured. These ideal conditions do not hold for the case of QuikSCAT and OSCAT because of operational differences in the sensors. Careful consideration of these differences must be made to accurately characterize the bias in QuikSCAT and OSCAT measurements. To aid in these considerations, in this chapter we present a simple model that relates QuikSCAT and OSCAT backscatter measurements to each other. Direct-comparison and model-based methods to estimate the parameters of the measurement model are presented. Implications of using temporally-disjoint QuikSCAT and OSCAT data in the estimation are examined, and simplifying assumptions are proposed.

#### 3.1 Measurement Model

As explained in Chapter 2, the main difference between OSCAT and QuikSCAT is measurement geometry. Both sensors are conically-scanning pencil-beam radars, however the incidence angles of QuikSCAT's beams are lower than those of OSCAT by approximately  $3^\circ$ . Because of the incidence response of the Earth's surface (see Figure 2.1), the difference in sensor incidence angles causes OSCAT-measured  $\sigma^0$  to be generally smaller than corresponding QuikSCAT measurements. We model the relationship between QuikSCAT and

OSCAT-measured  $\sigma^0$  in the absence of noise and measurement error as

$$\sigma_{OS}^0(t, l, \phi) = \sigma_{QS}^0(t, l, \phi) + F(\Theta, t, l, \phi), \quad (3.1)$$

where  $\sigma_{OS}^0(t, l, \phi)$  is the normalized radar cross-section in decibels observed by the OSCAT geometry at time  $t$ , location  $l$ , and azimuth angle  $\phi$ ;  $\sigma_{QS}^0(t, l, \phi)$  is the corresponding backscatter observed by the QuikSCAT geometry, and  $F(\Theta, t, l, \phi)$  is the contribution of the backscatter due to the incidence angle difference, where  $\Theta = \theta_{QS} - \theta_{OS}$ .  $F$  is dependent on the scattering characteristics of the target being measured, and is therefore time and location dependent. Note that the incidence contribution is additive, which is consistent with previous models of the incidence response [6, 8, 31].

Both sensors are susceptible to measurement errors that arise from inaccurate determination of radar equation parameters. However, for the purposes of intercalibration, we define QuikSCAT backscatter as the reference or “true” backscatter, and consider only OSCAT measurement errors. To model these errors, the  $n^{\text{th}}$  measurement made by OSCAT,  $z_n$ , is expressed as

$$z_n = \sigma_{QS}^0(t_n, l_n, \phi_n) + F(\Theta_n, t_n, l_n, \phi_n) + G_e(t_n, l_n, \phi_n) + \text{noise}_n, \quad (3.2)$$

where  $G_e$  represents the absolute error in determining the true backscatter for the OSCAT geometry. The measurement error is modeled as additive, since errors in the radar equation (Eq. 2.1) are generally additive in logspace [8]. The noise term represents communication noise and unmodeled errors, and is assumed to be zero-mean and independent of  $F$  and  $G_e$ .

The OSCAT measurement error  $G_e$  can be described as the sum of a fixed error and a variable error, expressed as

$$G_e(t, l, \phi) = G_{abs} + G'(t, l, \phi). \quad (3.3)$$

Without knowledge of the absolute  $\sigma^0$  of the surface, it is not possible to determine the fixed error  $G_{abs}$  [8]. In fact, a non-zero  $G_{abs}$  cannot be distinguished from  $F$  using the relative

calibration methods described in the remainder of this chapter. For simplicity, we assume  $G_{abs} = 0$  and focus on estimating the variable error  $G'$ .

The goal of land-based intercalibration is to determine estimates of  $F$  and  $G_e$  to be applied to OSCAT measurements in order to achieve the corrected  $\sigma^0$  at QuikSCAT's geometry, expressed as

$$\widehat{\sigma_{QS}^0}(t_n, l_n, \phi_n) = z_n - \widehat{F}(\Theta_n, t_n, l_n, \phi_n) - \widehat{G_e}(t_n, l_n, \phi_n), \quad (3.4)$$

where  $\widehat{\sigma_{QS}^0}$ ,  $\widehat{F}$ , and  $\widehat{G_e}$  are estimates of the QuikSCAT backscatter, incidence contribution, and OSCAT measurement error, respectively. The remainder of this chapter outlines the methodologies of using QuikSCAT and OSCAT land backscatter measurements to estimate the terms in the measurement model.

### 3.2 Methodology of Estimating $G'$

Previous research has shown that homogeneous, stable, isotropic land targets, such as tropical rainforests, are effective in identifying relative measurement biases [7, 8, 12, 38]. Relative biases are identified by comparing backscatter over the calibration target with a reference or expected value. In this thesis, we employ homogeneous targets for estimating  $G'$ , using the Amazon and Congo rainforests as calibration targets. Using more than one target allows us to identify possible locational dependency in the bias.

Data selection masks that represent homogeneous regions within the rainforests are used for selecting the OSCAT data used to estimate  $G'$ . The masks are produced as follows. All high-resolution QuikSCAT SIR  $\sigma^0$  images of the Amazon and Congo rainforests from the 2009 dataset are selected. Pixels statistics are computed in time and pixels which have a standard deviation  $< 0.5$  dB and a mean within 0.5 dB of the mean  $\sigma^0$  of the region are selected. A median filter is then applied to produce continuity between selected pixels. The resulting areas are shown in Figure 3.1. Due to its size, the Amazon region is divided into two separate masks.

Isotropy and long-term temporal stability are important characteristics for calibration targets. Isotropy allows azimuthal biases to be identified while stability allows long-term

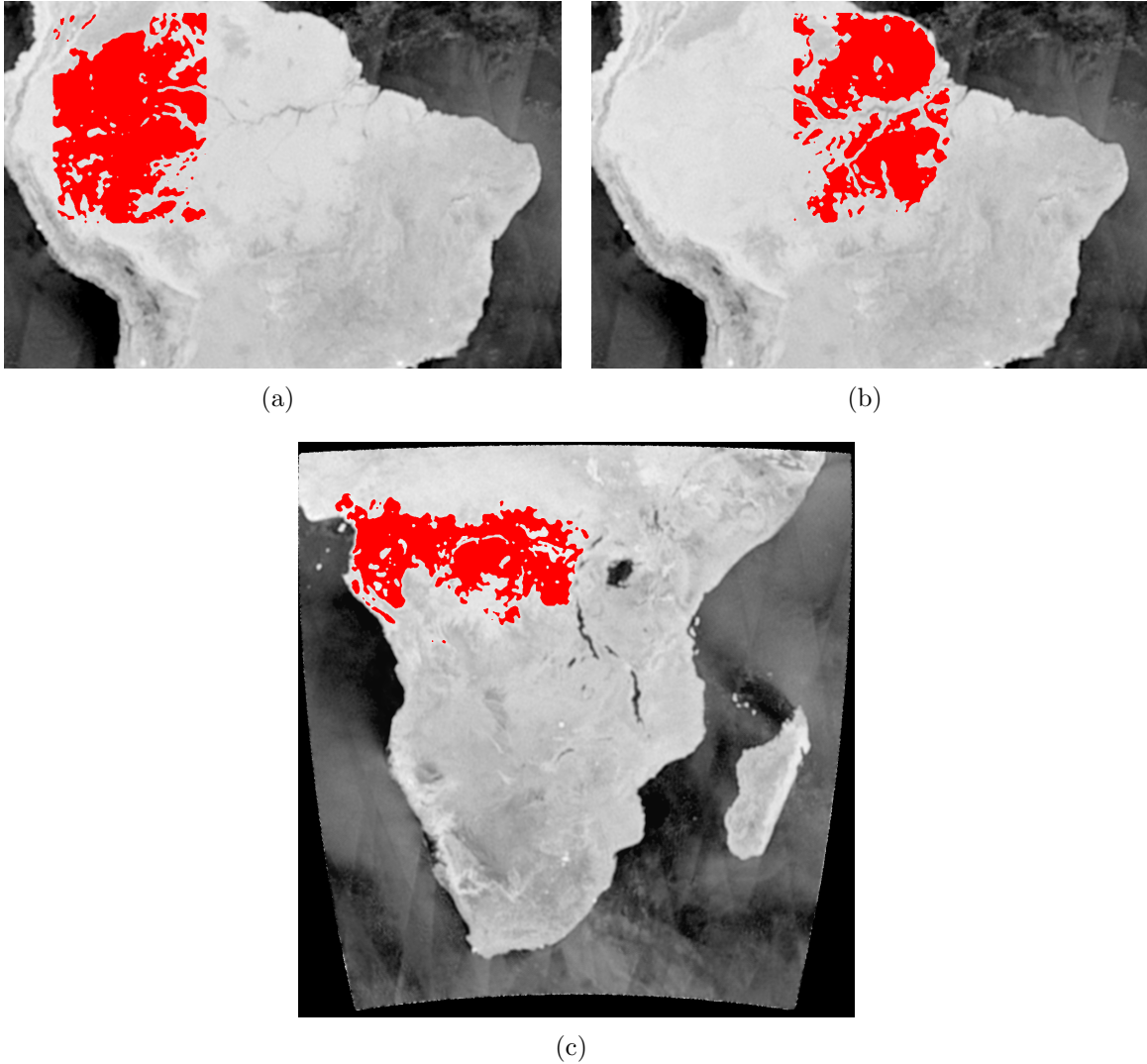


**Figure 3.1:** Regional data selection masks for (a) the West Amazon, (b) the East Amazon, and (c) the Congo rain forests.

drifts in backscatter to be identified. To test the assumptions of isotropy and stability over our chosen calibration targets, we examine all QuikSCAT data selected by the masks. In Figure 3.2, QuikSCAT backscatter is plotted against the antenna azimuth angle for the East Amazon region. The relatively flat response of backscatter over the azimuth range supports the assumption of isotropy. In Appendix B, we examine in greater detail the azimuth response of QuikSCAT over the calibration targets.

Any observed anisotropy over these regions in the corresponding OSCAT data is characterized as measurement bias. We model this bias using a low-order Fourier series and

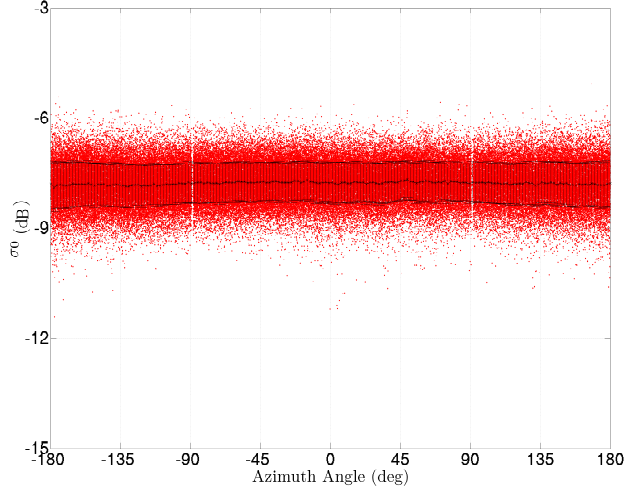


**Figure 3.2:** Azimuth response of H-pol, descending QuikSCAT  $\sigma^0$  for the East Amazon region. Data is selected from JD 1-20, 2009.

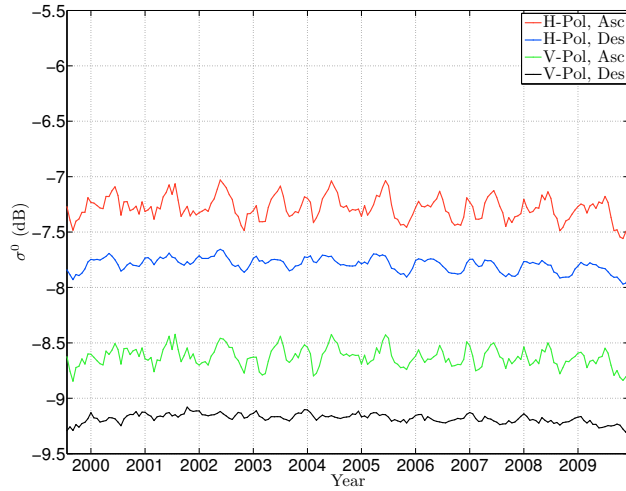


**Figure 3.3:** 20-day mean QuikSCAT  $\sigma^0$  for the East Amazon region.

suggest a method to remove it from the OSCAT data. The calibration targets are large enough to be sampled by the full range of azimuth angles, which is necessary to accurately estimate the Fourier components [30]. Chapter 4 summarizes the results of this method and examines time and location dependencies of the azimuthal bias.

The long-term stability of the calibration targets is illustrated in Figure 3.3. In the figure, 20-day average backscatter values are plotted over QuikSCAT's mission life for the East Amazon region. Although there are seasonal cycles in  $\sigma^0$  ranging up to 0.5 dB, the

**Table 3.1:** Summary of 2000-2008 year averages over calibration targets where  $\mu$  is the mean and  $\sigma$  is the standard deviation. Units are in dB.

Target	H-pol, Asc.		H-pol, Des.		V-pol, Asc.		V-pol, Des.	
	$\mu$	$\sigma$	$\mu$	$\sigma$	$\mu$	$\sigma$	$\mu$	$\sigma$
E. Amazon	-7.27	0.023	-7.78	0.028	-8.62	0.015	-9.17	0.020
W. Amazon	-7.18	0.029	-7.72	0.029	-8.53	0.023	-9.10	0.019
Congo	-6.92	0.030	-7.49	0.031	-8.23	0.026	-8.84	0.021

mean backscatter remain stable year to year. As a side note, the difference in ascending and descending backscatter suggests the presence of diurnal phenomena, which will be considered when estimating  $F$ . The statistics of the year-averaged backscatter for the complete years of QuikSCAT’s mission life (2000-2008) are shown in Table 3.1. The remarkably low inter-annual variability of the year averages indicates that the calibration targets are indeed stable.

In Chapter 4, we examine the time series of OSCAT backscatter over the calibration targets. Using 2012 data as a reference, any observed drift in the year means that is greater than the inter-annual variability values in Table 3.1 is characterized as bias. Calibration constants are calculated from the OSCAT data for each year previous to 2012.

### 3.3 Contributions to $F$

We note that the measurement model in Eq. 3.2 is appropriate for coincident QuikSCAT and OSCAT measurements. Under coincident conditions,  $F$  represents the difference in backscatter resulting from the incidence response of the surface. However, because the sensors’ orbits differ in swath location and ascending nodes, there are other contributing factors to the difference in backscatter. Without knowledge of the true  $\sigma^0$ , the difference in backscatter that arises from orbit differences is indistinguishable from that of the incidence response. We therefore redefine the model term  $F$  as simply the *relative calibration*, or the difference in QuikSCAT and OSCAT measurements resulting from the different sensor incidence angles and orbits. The following describes how orbit differences contribute to the relative calibration.

QuikSCAT and OSCAT have sun-synchronous orbits designed so that their swaths are approximately fixed relative to the surface. The fixed swaths do not perfectly overlap

each other, which causes a difference in the azimuth angles of the sensors when observing the same point on the surface. For anisotropic regions (where backscatter is dependent on azimuth angle), a difference in QuikSCAT and OSCAT backscatter can arise from both the incidence response and the anisotropy of the region. For simplicity, we assume complete isotropy over the Earth’s surface when using the sensors’ data to estimate  $F$ . This allows collocated backscatter measurements to be compared without regard to their azimuth angles. The same assumption of isotropy is made in SIR image formation [37], so we expect the results of comparison to be applicable to SIR images as well.

Since the ascending/descending nodes of the QuikSCAT and OSCAT orbits differ, the local times of day (LTD) at which a location is measured by each sensor may differ by several hours. For example, equatorial regions have an approximate 6-hour LTD difference between QuikSCAT and OSCAT measurement times. Because of this, diurnal changes in backscatter that occur between measurement times may also contribute to the relative calibration  $F$ . Examples of diurnal phenomena that can lead to backscatter differences include changes in dew concentration and leaf orientation at different times of day [12]. When estimating the relative calibration, we compare corresponding flavors of backscatter, that is, QuikSCAT H-pol, ascending data is compared with OSCAT H-pol, ascending data, etc. This choice is arbitrary; QuikSCAT ascending data could be compared with OSCAT descending data as well. In any case, each flavor exhibits an LTD difference of approximately 6 hours at the equator; thus, diurnal phenomena may contribute to the relative calibration.

In Appendix A, we identify regions that are anisotropic and exhibit diurnal phenomena. In summary, desert and mountain regions exhibit the strongest anisotropy, while the remainder of land surfaces exhibit near-isotropic characteristics. The contribution of anisotropy to the relative calibration may exceed a few tenths of a decibel over anisotropic regions. Diurnal phenomena produce variations in  $\sigma^0$  of several tenths of a decibel over tropical rainforest regions, which contribute to the relative calibration. Most other regions exhibit little or no diurnal phenomena.

### 3.4 Methodology of Estimating $F$

To estimate the relative calibration  $F$ , a simple comparison of simultaneous, collocated QuikSCAT and OSCAT backscatter measurements can be made. This approach is taken in [22] where data from the temporally-overlapping period of the sensor mission lives were compared. However, because the amount of data that can be used in this approach is sparse (approximately one month’s worth), resolving temporal and locational dependencies in  $F$  is not possible. To overcome this, we use data from temporally-disjoint portions of the QuikSCAT and OSCAT datasets to estimate  $F$ . Doing so allows us to compare data from all locations and under different seasonal conditions.

Care must be taken in comparing temporally-disjoint QuikSCAT and OSCAT measurements to estimate the relative calibration because there are several factors that may add bias or variability to the estimate. Because the sensors’ measurement times can differ by a year or more, the inter-annual variability of surface will have an effect on the estimate. Inter-annual variability for a region is primarily caused by inter-year seasonal shifts of the scattering properties. Environmental variables such as vegetation density, freeze-thaw status, and soil moisture all affect backscatter and are prone to seasonal shifts in time [4, 28, 39]. We present methods in the following section that attempt to overcome these effects.

Long-term changes in backscatter, such as those caused by human activities or climate change, can also bias the relative calibration estimate. For example, backscatter changes that arise from deforestation or long-term drought between QuikSCAT and OSCAT measurement times may be incorrectly attributed to differences between the sensors. For simplicity, the long-term mean scattering characteristics of the surface are assumed to be stable between the QuikSCAT and OSCAT measurement times.

#### 3.4.1 Methods

Given the considerations above, we present direct and model-based comparison methods for determining the relative calibration between the sensors. These methods focus on reducing potential bias and variance in the estimate resulting from seasonal variability. Given the vast extent of the Earth’s land surfaces and the numerous environmental variables that affect scattering, we limit the application of the methods to small geographic areas in most

cases. Chapter 5 summarizes the results of these methods and the advantages and disadvantages of each.

Direct comparison of QuikSCAT and OSCAT backscatter is a simple means of estimating the relative calibration between sensors. The technique calculates the relative calibration as the average difference between collocated backscatter measurements. QuikSCAT and OSCAT backscatter are averaged over both short, 20-day intervals and year-long intervals and directly compared. Comparing over short intervals may resolve seasonal variability in the relative calibration, however inter-annual seasonal shifts increases the variability of the estimate with this method. Using year-averaged backscatter to estimate  $F$  is not as susceptible to seasonal variability, however it does not resolve possible seasonal trends in the relative calibration.

To further resolve the seasonal variability of  $F$ , its estimate can be conditioned on environmental variables that give rise to seasonal trends in backscatter, rather than short time intervals. Though several variables exist that affect radar scattering, for simplicity we examine only a few that are hypothesized to be the dominant factors in backscatter seasonal variability, including vegetation density and freeze-thaw status. Through statistical and regression analyses, the backscatter is modeled as a function of the environmental variables and the relative calibration is given by

$$\hat{F}(\gamma) = \sigma_{OS}^0(\gamma) - \sigma_{QS}^0(\gamma), \quad (3.5)$$

where  $\gamma$  is the environmental variable. This method may allow seasonal trends in  $F$  to be identified more readily at the expense of using auxiliary information about the environment.

### 3.5 Summary

A simple measurement model relating backscatter at QuikSCAT and OSCAT geometries has been presented. This model provides the framework for the following chapters. The model describes the OSCAT measurement error, which results from incorrect calibration and inaccurate determination of radar equation parameters. This error is identified using homogeneous, isotropic rainforest targets. The model also describes the relative cali-

bration between QuikSCAT and OSCAT measurements. Anisotropy and diurnal phenomena contribute to the relative calibration and are examined in Appendix A. Temporally-disjoint QuikSCAT and OSCAT measurements are used to estimate the relative calibration in order to resolve its possible seasonal trends, though doing so may introduce bias and variability in the estimate. Direct-comparison and model-based techniques for estimating the relative calibration are described. The following chapters summarize the results.

## Chapter 4

### OSCAT Measurement Bias

OSCAT measurements contain a variable bias,  $G'$ , that results from inaccurate calibration or determination of radar equation parameters. Removing the bias is essential for the accuracy of land and ocean wind studies. Researchers have previously identified components of the bias, including drifts in mean backscatter [21, 22], as well as an azimuth-dependent bias [22, 23], both on the order of several tenths of a dB. However, these studies do not provide much detail of temporal and locational dependencies of the bias.

In this chapter, we estimate OSCAT drift and azimuth biases and examine their temporal and locational variation using the methods described in Chapter 3. Using the Amazon and Congo rainforests as calibration targets, we estimate the bias as the difference between the measured and expected backscatter. Temporal and spatial variations are found in the bias. These variations may be caused by changes in either the OSCAT measurement system or the calibration targets, though it is not possible to determine the cause by relative calibration methods alone. Comparing OSCAT bias estimates with those of QuikSCAT measurements may help in identifying the cause of bias variability. We examine the drift in Section 4.1 and the azimuth bias in Section 4.2. Corrections to remove the bias are suggested.

#### 4.1 Inter-annual Drift

As noted in Chapter 3, the mean backscatter over rainforest targets is especially stable year to year (within 0.03 dB as measured by QuikSCAT). Therefore, large inter-annual changes in OSCAT backscatter are likely caused by measurement error instead of changes in the calibration targets. We identify backscatter drift in Figure 4.1, where a time-series of  $\sigma^0$  over the East Amazon is plotted. The plot is discontinuous for times when data is not available. We note the large drop in backscatter occurring during 2010, which has

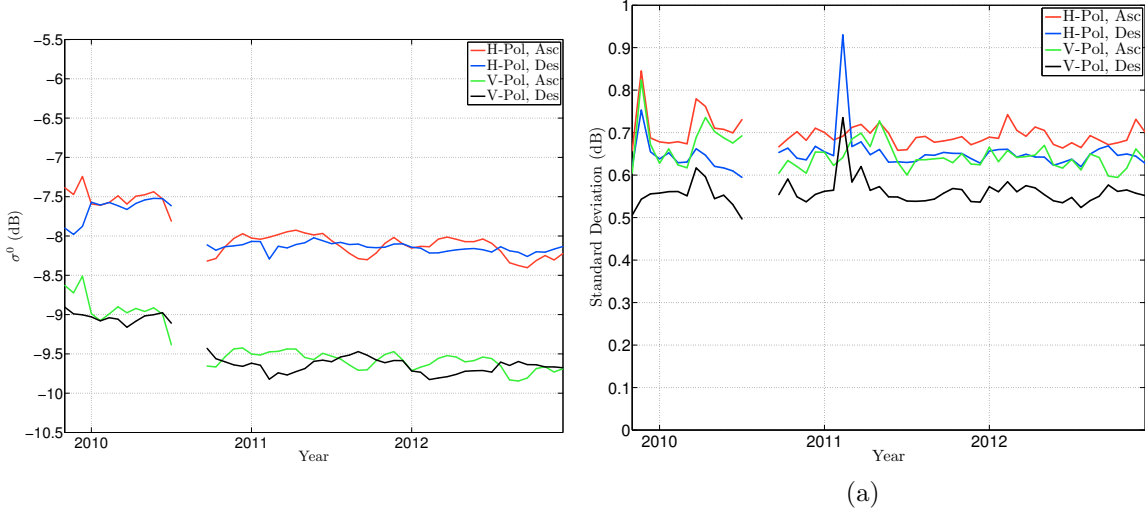


**Figure 4.1:** Mean and standard deviation of OSCAT backscatter for the East Amazon region.

**Table 4.1:** Drop in backscatter between 2010 and 2012. Data from JD 1-180 over all calibration regions are used. Units are in dB.

Flavor	Difference by Region		
	E. Amazon	W. Amazon	Congo
H-Pol, asc.	-0.55	-0.55	-0.61
H-pol, des.	-0.60	-0.61	-0.61
V-Pol, asc.	-0.62	-0.61	-0.68
V-pol, des.	-0.70	-0.73	-0.76

been attributed to power fluctuations [22]. The large drop is summarized in Table 4.1, where the change in mean backscatter between JD 1-180, 2010 and JD 1-180, 2012 is calculated for the calibration regions. The change is found to be approximately constant across the rainforest targets, however it differs between ascending and descending data. We note that the values in Table 4.1 are slightly larger than the 0.5 dB drop reported in [21] where ocean measurements were used instead of land measurements.

To promote consistency in the OSCAT dataset, we arbitrarily choose OSCAT 2012 data as a reference and calculate annual calibration offsets for the years 2009-2011. The results for the East Amazon are shown in Table 4.2. The offsets exceed the expected inter-annual variability of 0.03 dB in almost all cases, which, excluding unexpected environmental

**Table 4.2:** 2012 Reference mean and year calibration offsets calculated from the East Amazon data. Units are in dB.

Flavor	2012 Reference	2011 Calibration	2010 Calibration	2009 Calibration
H-Pol, asc.	-8.17	-0.10	-0.44	-0.82
H-pol, des.	-8.18	-0.07	-0.42	-0.27
V-Pol, asc.	-9.65	-0.11	-0.49	-1.05
V-pol, des.	-9.71	-0.08	-0.48	-0.73

change, indicates system change over time. Though not shown in the table, the offsets are found to be fairly location-independent, with each target’s offset being within 0.08 dB of each other, except in the case of 2009 data, where the offsets vary by as much as 0.2 dB with location. We attribute the 2009 variability to the small amount of available data and possible power fluctuations.

Many of the calibration values in Table 4.2 are close to or exceed 0.5 dB, which is the operational accuracy requirement for wind retrieval set by ISRO [22]. Consequences of uncompensated drift bias include inaccurate backscatter-derived ocean winds and land measurements. Applying an additive constant to the data to cancel the offsets may mitigate these consequences.

## 4.2 Azimuthal Bias

After the launch of the OSCAT, a difference of 30° between the antenna azimuth angle and the reading of the scan-angle encoder was discovered. The spacecraft was rotated about the yaw axis to partially compensate for the difference, however, a 10° offset still remains [35]. The offset causes an uncompensated Doppler frequency shift that depends on the antenna azimuth angle, as well as the latitudinal position and ascending/descending state of the sensor. Given the available processing bandwidth and the bandwidth of a single pulse, a portion of the received signal may be shifted outside of the processor’s passband at certain ranges of azimuth angle [35,40]. This can introduce an azimuth-dependent bias in  $\sigma^0$  measurement. This section focuses on quantifying and modeling observed azimuthal biases in OSCAT backscatter using rainforest calibration targets.

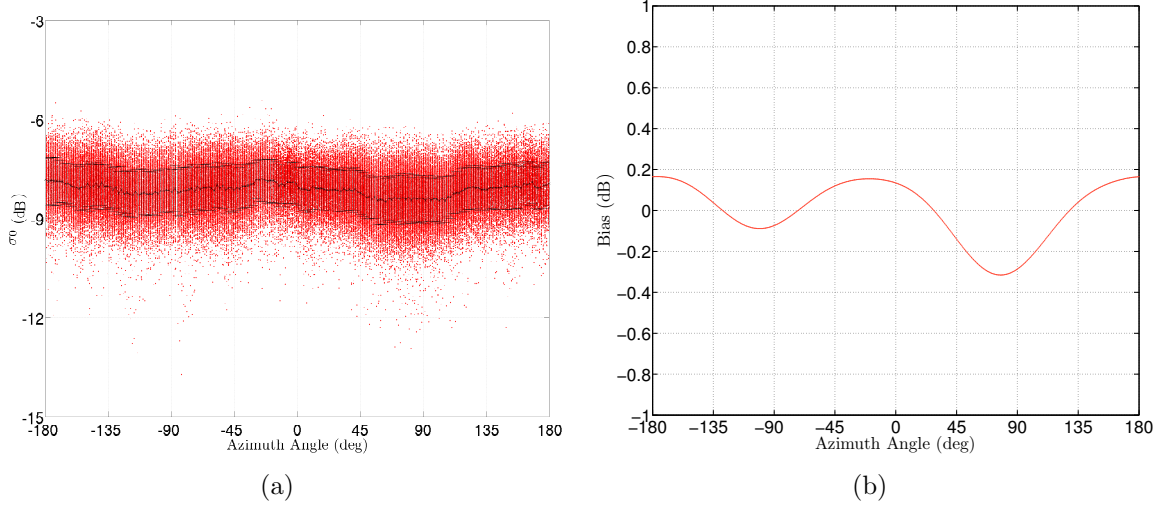


**Figure 4.2:** (a) Azimuth response of OSCAT H-pol, ascending  $\sigma^0$  for the East Amazon region. Data is selected from JD 1-20, 2012. (b) The estimated measurement bias using a  $N = 4$  Fourier model.

As noted in the previous chapter, rainforest calibration targets have an isotropic backscatter response, which is confirmed with QuikSCAT measurements as shown in Appendix B. There is, however, a definite azimuthal dependence in OSCAT data collected for these regions. To illustrate, Figure 4.2(a) shows the varying OSCAT azimuth response over a rainforest target. Following previous research [29,30], the backscatter-azimuth dependence is modeled using a  $N^{\text{th}}$ -order Fourier series of the form

$$\sigma_{OS}^0(\theta) = A + \sum_{k=1}^N [I_k \cos k\phi + Q_k \sin k\phi]. \quad (4.1)$$

The least-squares solution of the coefficients  $A$ ,  $I_k$ , and  $Q_k$  are determined from reported backscatter and antenna azimuth angle measurements.  $A$  represents the mean backscatter of the target and the periodic terms represent the azimuthal bias. The tradeoff in choosing the model order  $N$  is between simplicity and accuracy. The Fourier model is applied to OSCAT 2012 data for several choices of  $N$  and the resulting mean-squared error values are shown in Table 4.3. We choose to use  $N = 4$  for the remainder of this chapter because it offers a good balance in model order and mean-squared error.

**Table 4.3:** Comparison of Fourier model orders. OSCAT 2012 V-Pol, ascending data from the Amazon East region were used. The variance of the unmodeled data is  $\sigma^2 = 0.414$ .

$N$	Mean-Squared Error
2	0.372
4	0.366
8	0.364
12	0.364
16	0.363
32	0.362

The resulting estimated bias of the data in Figure 4.2(a) is shown in Figure 4.2(b). The maximum change in the bias over the azimuth range is approximately 0.5 dB. Such variation in the OSCAT data may cause wind retrieval accuracy to be worse than the 2 m/s, 20° accuracy requirement defined by ISRO [22]. The azimuth bias can also negatively affect OSCAT SIR images, where isotropy in backscatter is generally assumed. The goal of this section is to characterize the temporal and locational variability of the azimuth bias so that it can be removed, thereby attaining more accurate wind and backscatter measurements.

#### 4.2.1 Temporal Variation

To examine the temporal variation of the azimuth bias, we divide the data into 20-day intervals and apply the Fourier model. A 20-day interval is long enough to capture data covering the entire azimuth range and to reduce noise, and is short enough to resolve seasonal variation. The resulting bias estimates for the East Amazon region are plotted in Figure 4.3. We see that the curves vary from each other by 0.2 dB in some instances. The variation of the bias with time may be caused by inhomogeneous seasonal changes in the rainforest or gain changes within the OSCAT system. The time variability across all azimuth angles is typically below 0.07 dB in the 2010-2012 OSCAT data, which is on the same order as the variability of the apparent QuikSCAT azimuth bias (see Appendix B); thus we attribute the majority of temporal variation in the azimuth bias to the calibration targets for these years. OSCAT 2009 bias estimates have a higher temporal variability ( $>0.11$  dB), especially in the

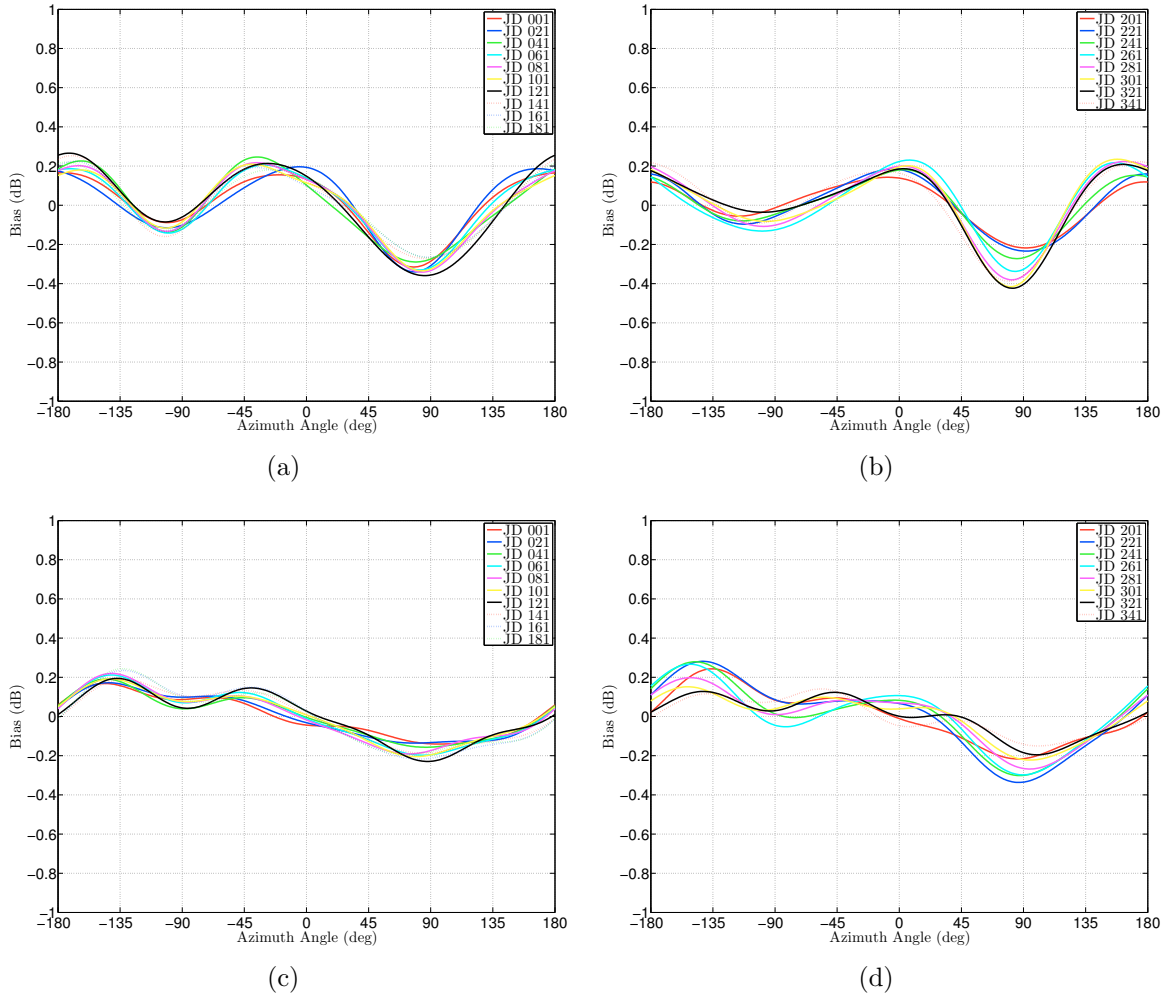


**Figure 4.3:** Azimuth bias of OSCAT 2012 data for the East Amazon region. (a)-(b) H-pol, ascending. (c)-(d) H-pol, descending.

H-pol data, which may be caused by the power fluctuations noted above. These results are insensitive to our choice of  $N$ ; similar results were found when using  $N = 32$  Fourier model.

As shown in Figure 4.3, the difference in the bias between the ascending and descending data can be large, exceeding 0.2 dB at some angles. The corresponding differences in QuikSCAT data are less than 0.08 dB. Since we expect the surface azimuth response to remain constant between ascending and descending passes, the difference is attributed to the OSCAT system. A possible explanation for the ascending/descending difference follows from [35], where it is explained that the uncompensated Doppler shift of the received signal differs between ascending and descending passes. In addition, it may be that the temper-

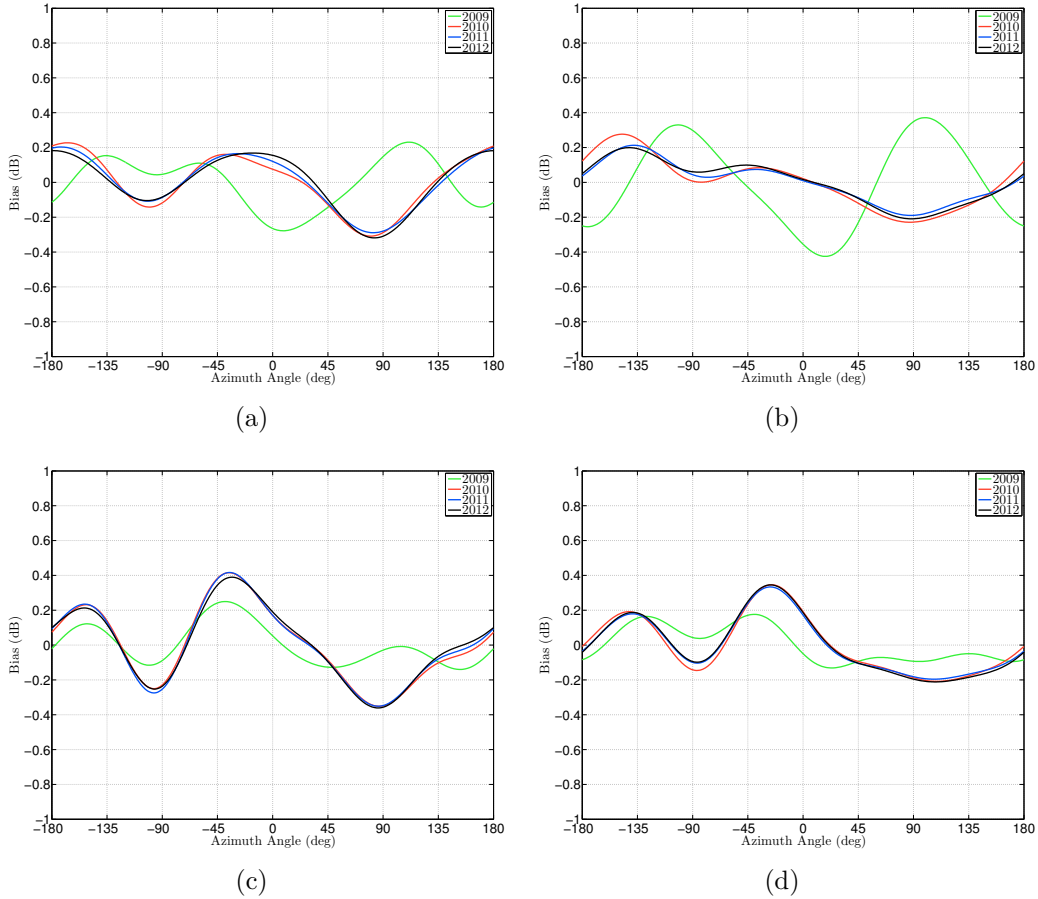


**Figure 4.4:** Azimuth biases of OSCAT data. (a) H-pol, ascending, (b) H-pol, descending, (c) V-pol, ascending, (d) V-pol, descending.

ature change OSCAT experiences as it passes from sunlight (descending pass) to shadow (ascending pass) in its orbit introduces fluctuations in the data [8].

Inter-annual variations in the azimuth bias are examined in Figure 4.4, where the bias for each year of OSCAT’s mission life is shown. The bias is relatively stable between 2010 and 2012; however there are fluctuations in the 2009 data.

#### 4.2.2 Locational Variation

We examine the locational dependence on the azimuth bias by comparing the results from each calibration target. Figure 4.5 shows the biases of the targets calculated using 2012 data. The differences between regions exceed 0.2 dB at certain azimuth angles, compared to a typical difference of  $<0.04$  dB in the QuikSCAT data. The cause of this locational

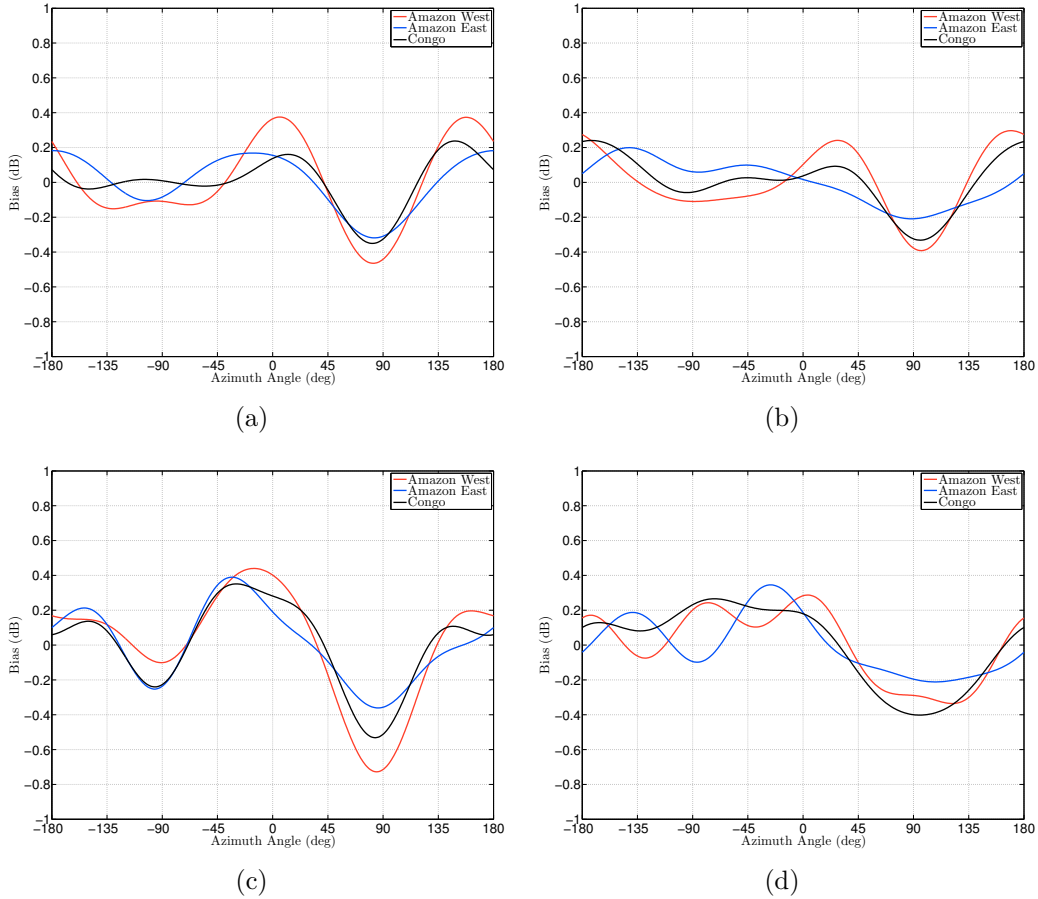


**Figure 4.5:** Azimuth bias of OSCAT 2012 data. (a) H-pol, ascending, (b) H-pol, descending, (c) V-pol, ascending, (d) V-pol, descending.

dependency is not immediately clear. The uncompensated Doppler shift described above possesses a latitude-dependent term, however it is not the cause of the locational dependence seen here since the rainforest targets reside at approximately the same latitude.

Assuming the OSCAT system is the cause of the locational dependency of the azimuthal bias, more calibration regions are needed to describe this dependency. However, because of the high seasonal variability for most regions, there is a lack of suitably large and stable isotropic land targets that may be used. Given the similarities of the biases between regions and their relative insensitivity to time, the locational dependence may be simple enough to be represented by a low-order model that is periodic with longitude. We test this hypothesis by fitting a second-order Fourier model to the coefficients  $I_k$  and  $Q_k$  computed

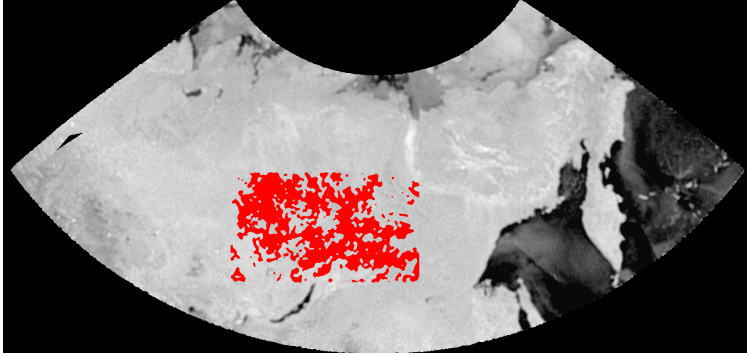


**Figure 4.6:** Data selection mask for Siberia.

for the calibration regions. For example, the coefficient  $I_k$  is modeled as

$$I_k(\varphi) = \sum_{n=0}^2 [L_n \cos n\varphi + M_n \sin n\varphi], \quad (4.2)$$

where  $\varphi$  is the average longitude in radians of the calibration region, and  $L_n$  and  $M_n$  are parameters to be solved for in the least-squared error sense. The purpose of the model is to predict  $I_K$  and  $Q_k$  over the range of longitudes outside of the original calibration targets.

To test the efficacy of the model, the predicted coefficients  $I_K$ ,  $Q_k$  are compared against the actual coefficients for an isotropic location. A good choice of location would be the rainforest regions of Indonesia since it is isotropic and widely differs in longitude from the other calibration targets, however OSCAT does not sample the area over the full range of azimuth angles. The Boreal forest of Siberia is generally isotropic and large enough for sufficient coverage of the azimuth range [9]. Using the same procedure described in Chapter 3, a data selection mask is formed for Siberia, shown in Figure 4.6. All OSCAT 2012 measurements from the mask are selected and the fourth-order  $I_K$ ,  $Q_k$  coefficients are computed.

In Figure 4.7, we compare the predicted and actual coefficients for Siberia. The figure also shows the coefficients for the Amazon and Congo calibration regions and the locational relationship described in Eq. 4.2. The actual low-order  $I_1$  and  $Q_1$  terms differ from the model prediction typically by 0.1 dB or more, however the higher-order terms differ by 0.04 dB or less. These results are consistent for all flavors of OSCAT backscatter. We see that modeling

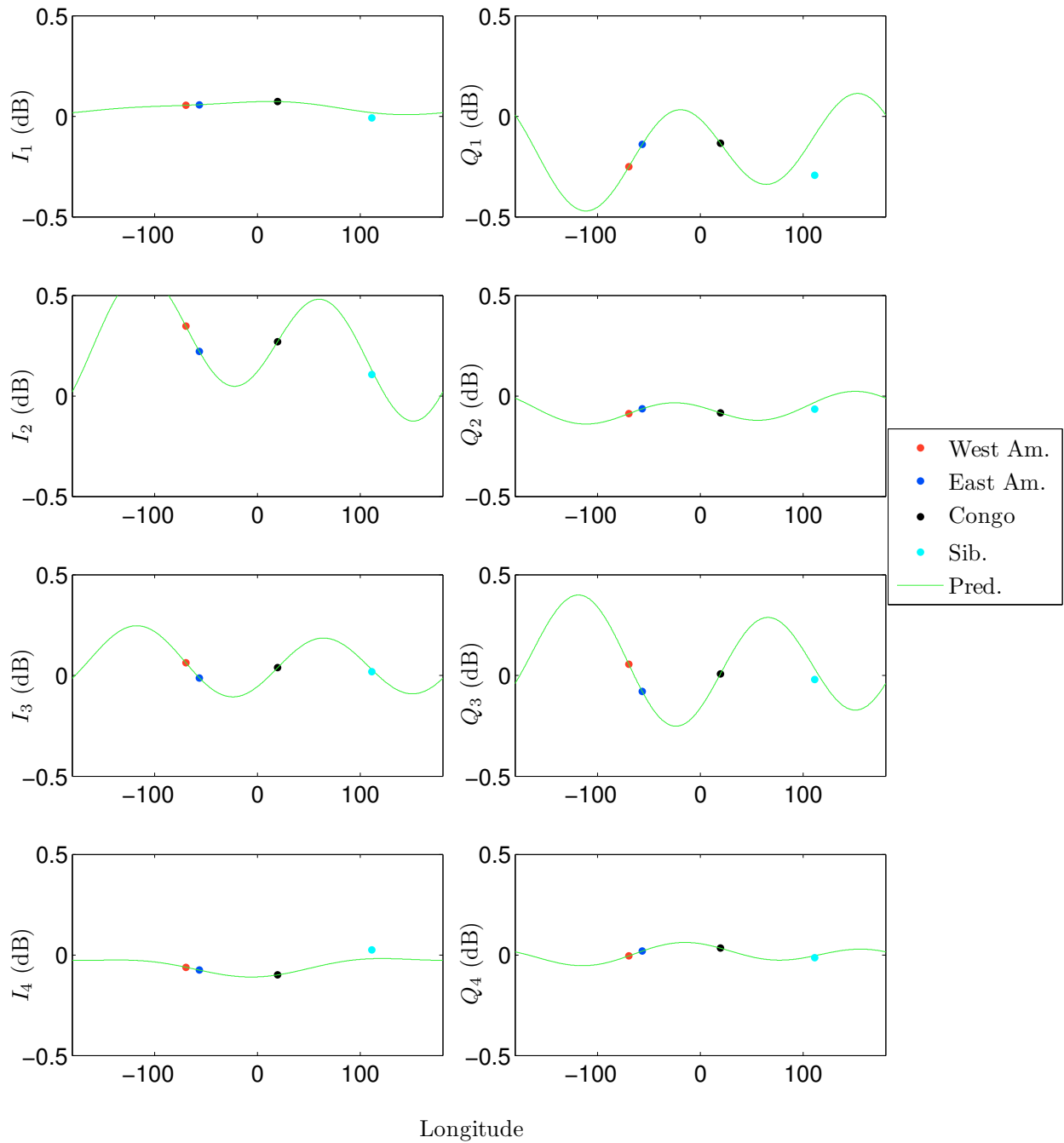


**Figure 4.7:** Actual  $I_K, Q_k$  coefficients computed from V-pol, ascending data for the calibration regions. The green curves represent the least-squares fit of the model in Eq. 4.2 to the Amazon and Congo coefficients.

the locational dependence of the azimuthal bias in this way is somewhat beneficial, however it is unknown if the model choice is appropriate or what the cause of the deviation in the low-order terms is.

As a side note, the locational dependence of the azimuthal bias can adversely effect the accuracy of wind retrieval measurements. Though characterizing the bias over land is difficult because of the lack of calibration targets, doing so over the ocean can be done more simply. A method employed in [41] uses a wind-to-backscatter GMF to convert wind vectors derived from computational models to equivalent  $\sigma^0$  values. By comparing the measured  $\sigma^0$  with the GMF output over the range of azimuth angles, the azimuthal bias can be described at all ocean locations where there is sufficient wind data available. It is not clear if the results of this procedure would apply to land measurements, given the large difference in backscatter magnitude between ocean and land.

### 4.2.3 Correction

Though the azimuthal bias varies by location, there are low-order similarities between each of the original calibration regions. For simplicity, we combine OSCAT 2012 data from all calibration targets and solve for  $I_k$  and  $Q_k$  in Eq. 4.1. The resulting coefficients are listed in Table 4.4. The bias is removed from the OSCAT backscatter measurement,  $z_n$ , as

$$z'_n = z_n - \sum_{k=1}^4 [I_k \cos k\phi_n - Q_k \sin k\phi_n], \quad (4.3)$$

where  $z'_n$  is the corrected measurement. The correction is demonstrated in Figure 4.8, where we plot the combined 2012 calibration target data before and after applying the correction. The magnitude of the corrections exceeds 0.2 dB at some azimuth angles in the H-pol data, and 0.4 dB in the V-pol data. It is found that the total variability of  $\sigma^0$  over the calibration targets decreases by up to 7.2% with the applied correction.

To illustrate the effect of the correction, we compare SIR images of the Amazon region produced from the biased and corrected backscatter data in Figure 4.9. The faint diagonal streaks apparent in the left image are mainly caused by the azimuth bias. The streaks are minimized in the corrected image, thus giving a more accurate view of backscatter for the

**Table 4.4:** Global 2012 Coefficients  $I_k$  and  $Q_k$ . Units are in dB.

k	H-pol, Asc.		H-pol, Des.		V-pol, Asc.		V-pol, Des.	
	$I_k$	$Q_k$	$I_k$	$Q_k$	$I_k$	$Q_k$	$I_k$	$Q_k$
1	-0.009	-0.053	-0.032	-0.074	0.059	-0.193	0.085	-0.240
2	0.253	-0.084	0.090	0.025	0.303	-0.085	0.078	-0.013
3	0.040	0.103	-0.044	0.071	0.038	0.007	-0.021	0.027
4	-0.003	-0.002	-0.041	-0.005	-0.048	-0.009	-0.002	-0.007

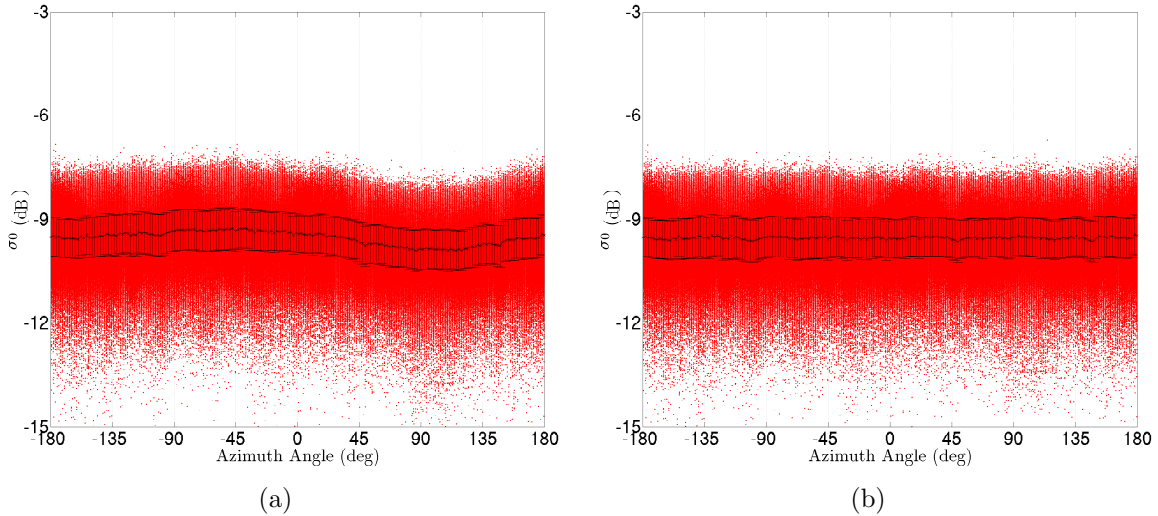


**Figure 4.8:** (a) Uncorrected 2012 OSCAT backscatter. (b) Corrected 2012 backscatter.

region. The difference image shows that the corrections result in a difference of several tenths of a decibel at some locations.

In the ideal case where the locational dependencies of the azimuth bias are known, the bias should be removed from the OSCAT data prior to intercalibration with QuikSCAT. Since the bias is not fully understood, we hesitate in applying a correction to the data as it may introduce errors for locations outside of the calibration regions. In Chapter 5, for comparison, we use both azimuth-corrected and uncorrected OSCAT data in the intercalibration techniques with QuikSCAT data. It will be seen in Section 5.1.2 that the globally-averaged coefficients in Table 4.4 offer improvement in  $\sigma^0$  accuracy for surfaces outside of the calibration regions.

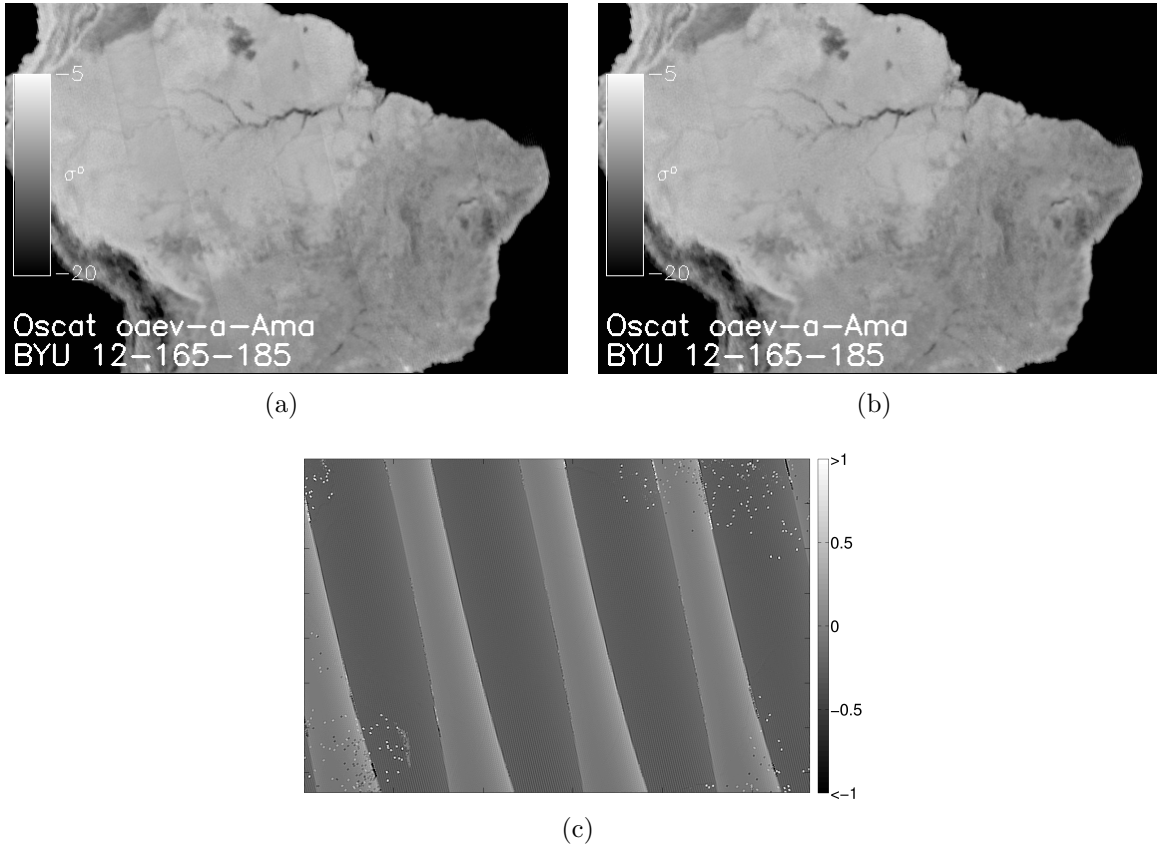


**Figure 4.9:** 20-day SIR images using (a) original data and (b) corrected data, and (c) their difference. The units of the colorscale are decibels.

### 4.3 Summary

An inter-annual drift and azimuth bias in OSCAT backscatter have been estimated using rainforest calibration targets. Using the QuikSCAT backscatter statistics over these regions as a reference, we determine the expected variability of the calibration targets and attribute additional variability in the estimated bias to temporal and locational changes in OSCAT gain. In summary, the inter-annual drift is not constant with time, but is independent of location. The drift, measured using 2012 data as a reference, approaches 0.5 dB in some cases. The azimuthal bias is observed to be dependent on location and differs from ascending to descending pass. Intra-year temporal variability of the bias is attributed to the calibration targets for 2010 to 2012, while additional variation in 2009 data is most likely due to power fluctuations. The magnitude of the bias exceeds 0.4 dB at certain azimuth

angles. Though locational dependencies are observed, we present evidence that a low-order model may aid in predicting the azimuth bias for regions outside of the calibration targets. Corrections are made using model coefficients derived from data combined over the calibration targets and are found to reduce measurement variance and improve SIR imagery over the calibration regions. For comparison, both uncorrected and corrected OSCAT data are used with QuikSCAT data for determining the relative calibration in Chapter 5.

## Chapter 5

### QuikSCAT/OSCAT Relative Calibration

This chapter focuses on estimating the QuikSCAT/OSCAT relative calibration and describing its dependence on time and location. As mentioned previously, the small overlapping portion of the QuikSCAT and OSCAT datasets from late 2009 is insufficient to completely describe temporal and locational variations in the relative calibration. To overcome this limitation, we compare data from the temporally-disjoint portions of the datasets. There are many environmental variables that give rise to differences in temporally-disjoint QuikSCAT and OSCAT backscatter besides the relative calibration; thus, care must be taken to avoid bias and variability in the estimate. To minimize such effects, direct and model-based comparisons were proposed in Chapter 3. We present the results of the techniques in this chapter.

Unfortunately, as shown in Chapter 4, the OSCAT dataset exhibits fluctuations in the measurements and gaps in the data during the initial years of operation. For most of the analyses of this chapter, we choose to employ only OSCAT data from 2012 because it represents the most recent and complete year of data. The OSCAT data are compared with QuikSCAT 2000-2008 data to estimate the relative calibration. The implications of using only a single year of OSCAT data in the comparisons include less certainty in the relative calibration estimate due to the inter-annual variability of the surface. The extensive QuikSCAT dataset allows us to estimate this inter-annual variability, which provides an idea of the accuracy of the relative calibration estimate. As more OSCAT data becomes available, multi-year versions of the techniques employed here will yield more accurate results.

In this chapter, the original OSCAT data and the azimuth-corrected data derived in Chapter 4 are used in comparisons with QuikSCAT data and the resulting differences are noted. Section 5.1 directly compares QuikSCAT and OSCAT data on regional and global

scales and at different time intervals to estimate the relative calibration. We note the impact of inter-annual surface variability on the accuracy of the estimate with the direct-comparison method. We find that the inter-annual variability and lack of data is prohibitive to resolving the possible seasonal variation in the true relative calibration for many regions. To resolve possible seasonal variations of the relative calibration, a model-based approach is taken in Section 5.2. There, we use auxiliary information about the surface to derive a backscatter model which is then used in Eq. 3.5 to estimate the relative calibration. The limitations of this method are the unknown effects of other environmental variables that are not considered, as well as inter-annual variability of the surface.

## 5.1 Direct Comparison

Direct comparison of QuikSCAT and OSCAT backscatter is a simple method of estimating the relative calibration. In this section, we compare the sensors' backscatter over short and long time intervals and on regional and global scales. Using short time intervals on the scale of a few weeks may allow seasonal variations of the relative calibration to be resolved for some regions; however, the estimate is susceptible to noise from the inter-annual variability inherent to the targets. Using year-long intervals may decrease the inter-annual variability of the target, but information on the seasonal trends of the relative calibration is lost.

### 5.1.1 Short-Term Comparison

We first compare QuikSCAT and OSCAT backscatter using 20-day intervals of time. Comparison of the data on global scales at these intervals is tedious; instead, we choose several arbitrary locations that represent different terrains in South America and compare their average backscatter. The regions are outlined in Figure 5.1 and documented in Table 5.1. Though the regions do not represent all terrain and climate conditions encountered in the backscatter datasets, the consequences of inter-annual surface variability seen over these locations apply to most other locations as well.

The 20-day average backscatter is computed for both sensors and the inter-annual variability of the means is computed from the QuikSCAT data. This information is plotted

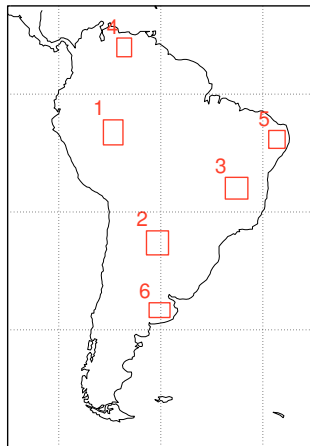


**Figure 5.1:** Regions of interest for short-term direct-comparison study.

**Table 5.1:** Regions of Interest for Direct Comparison of 20-day average backscatter.

No.	Terrain
1	Rainforest
2	Dry Forest
3	Savanna
4	Savanna
5	Desert and Shrubland
6	Temperate Grassland

in Figure 5.2 using the original, uncorrected OSCAT data. From the figure, we see that for forest and savanna regions, the mean backscatter from both sensors follows the same seasonal trends. The inter-annual variability for these regions (denoted by the red dotted lines) is relatively small, especially over the rainforest. For the desert and temperate grassland regions, the trends in the backscatter exhibit some similarities between sensors; however, because the inter-annual variability over these regions is large and time dependent, there are wide deviations in the OSCAT data from the seasonal trends of QuikSCAT.

The estimated relative calibration is the difference between the backscatter means. In Figure 5.3, the estimate is plotted for the regions of interest. Since only OSCAT 2012 is used in the difference, we expect some error in the estimate due to inter-annual variability and noise. To give an idea of the accuracy of the relative calibration estimate in the plot, we include the red dotted lines which are the inter-annual variability values from the previous

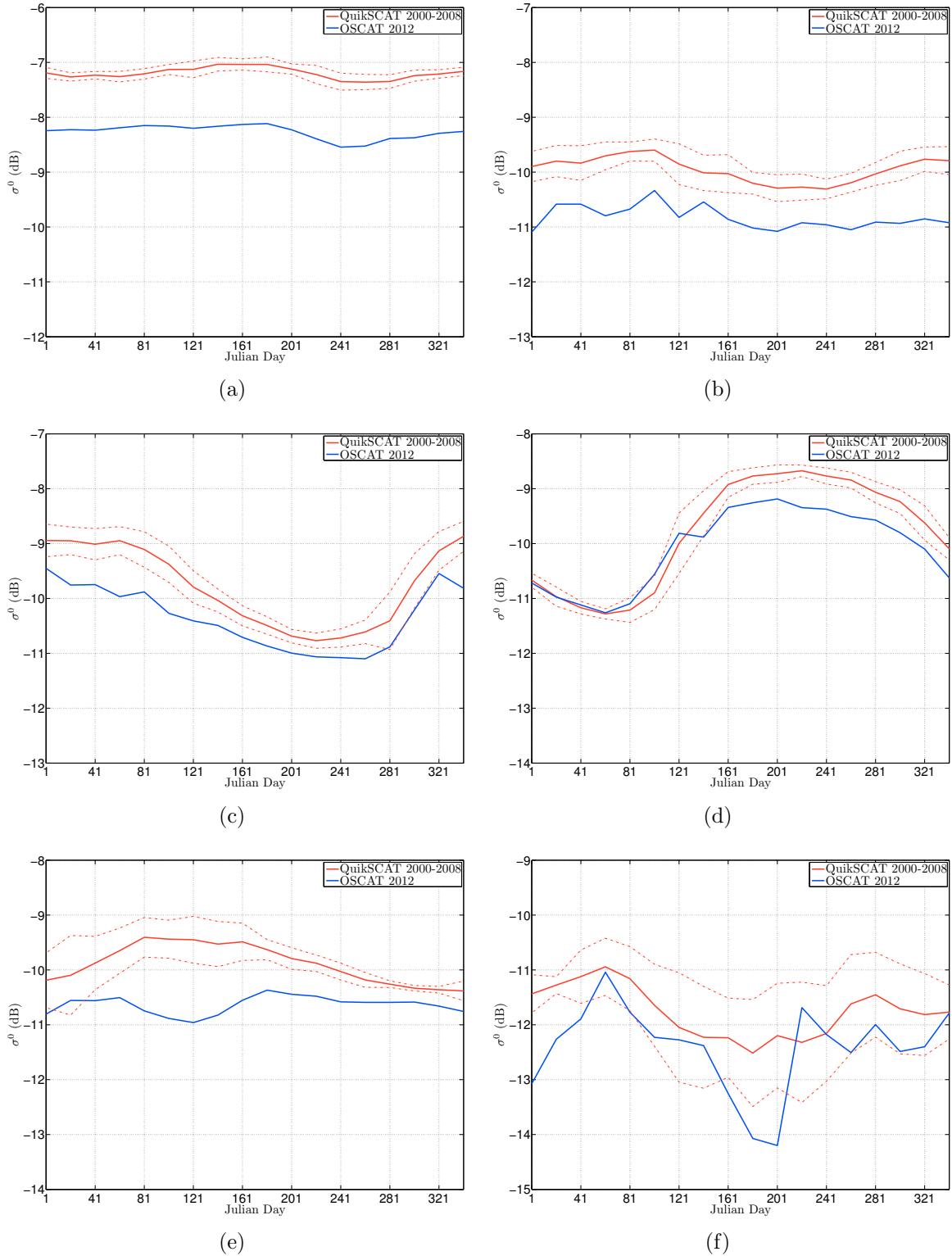


**Figure 5.2:** OSCAT 2012 and QuikSCAT 2000-2008 H-pol, ascending backscatter for the regions in Figure 5.1. (a)-(f) correspond to regions 1-6, respectively. The solid lines represent the mean backscatter and the dotted lines represent the inter-annual variability seen in the QuikSCAT data.

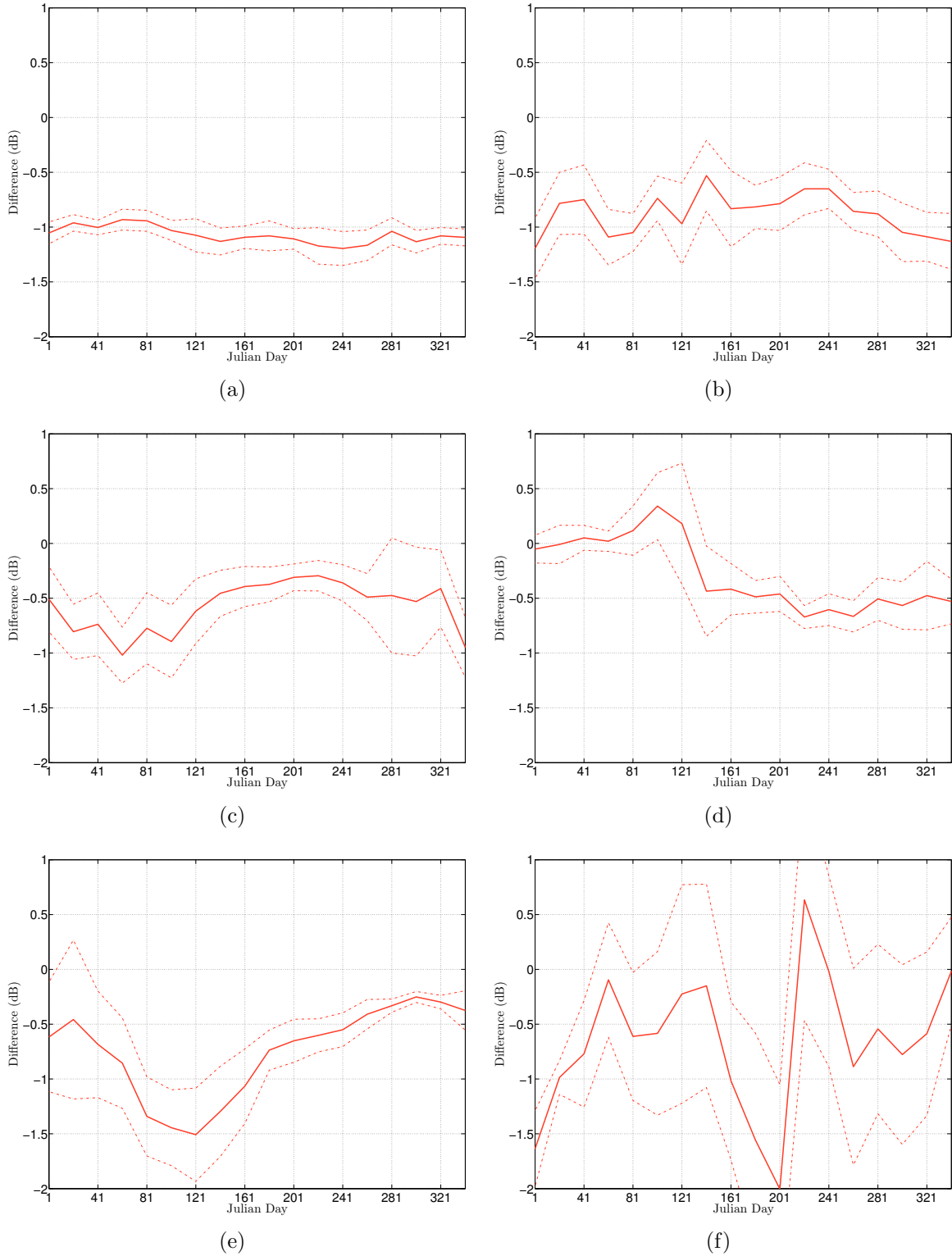


**Figure 5.3:** The difference between OSCAT 2012 and QuikSCAT 2000-2008 H-pol, ascending backscatter for the regions in Figure 5.1. (a)-(f) correspond to regions 1-6, respectively. The solid line represents the difference in average backscatter. The dotted lines are the inter-annual variability in QuikSCAT data and are provided to give an idea of the accuracy of the relative calibration estimate.

plot. We note from Figure 5.3(a) that the relative calibration appears to be relatively constant at approximately -1 dB over the rainforest region. In this region, a constant value for the relative calibration could be assumed for the entire year and still be within the observed inter-annual variability. We expect the same result for other rainforest regions as well, given the observed stability of these locations. For the other regions in Figure 5.3, it is difficult to discern whether the time dependency of the relative calibration estimate is representative of the true value or an artifact of using only OSCAT 2012 data in the comparison. The erratic time behavior of the estimate in Figure 5.3(f) is most likely due to the large inter-annual variability inherent to the location, and is not representative of the true relative calibration. Similar results hold when using the azimuth-corrected OSCAT data from Chapter 4. In this case, the relative calibration estimates differ only slightly from those in Figure 5.3.

Thus, given the limited amount of reliable OSCAT data and the QuikSCAT-observed inter-annual variability, directly comparing temporally-disjoint backscatter on short time-scales to estimate the relative calibration can yield unreliable results, at least for some regions. As future years of OSCAT data become available, averaging the data on short time scales can yield a more accurate estimate of the seasonal trends in OSCAT backscatter. Temporal variations in the relative calibration may then be resolved more accurately.

### 5.1.2 Long-Term Comparison

The inter-annual variability of the surface may be reduced if the time interval for averaging is increased. Comparing year-averaged backscatter may yield a more accurate relative calibration estimate, even when only a year of OSCAT data is used. However, averaging backscatter over a year causes information about possible short-term temporal variations in the relative calibration to be lost. Following a similar procedure from above, QuikSCAT and OSCAT data are collocated and their year averages are computed and compared. To compare backscatter over the entire globe, we bin the measurements on a  $0.1^\circ$  grid. Average backscatter maps are created for all backscatter flavors from each sensor. Differencing the respective maps from each sensor yields a relative calibration map, as shown in Figures 5.4-5.5. We note the diagonal streaks in the images which are artifacts of the azimuthal

bias in the original OSCAT data. Applying the azimuthal correction to the OSCAT data using the coefficients in Table 4.4 yields the maps in Figures 5.6-5.7, where the artifacts are substantially reduced. This is evidence that although there is locational variability in the observed OSCAT azimuthal biases, the low-order components of the bias are similar over global scales.

The inter-annual variability of the QuikSCAT year-averaged backscatter is also computed and the resulting maps are shown in Figures 5.8-5.9. These maps give an indication of the accuracy of the relative calibration maps; higher variability in the year averages for certain regions indicates that the relative calibration estimate may be inaccurate when using only a year of OSCAT data.

From the maps in Figures 5.6-5.7, we note a few interesting things. Overall, the relative calibration estimate typically ranges from -2 to 0 dB, which coincides with our understanding of the incidence response of land surfaces. Values above 0 dB generally correspond to the variable (darker) regions in Figures 5.8-5.9. The large positive estimate over regions in Greenland is most likely due to the large melt event that occurred in 2012 [42], and is not representative of the true relative calibration. There is a large difference in the estimate between ascending and descending data for certain regions. These regions are among those that exhibit diurnal phenomena, such as the equatorial rainforests (see Appendix A). The effects of surface anisotropy and differing incidence responses are especially visible in the Sahara desert and Arabian peninsula, where the relative calibration estimate is generally lower than the surrounding regions.

The similar relative calibration values for tropical rainforests result from similar scattering characteristics and diurnal phenomena. The average relative calibration for rainforest and other regions is listed in Table 5.2. The effect of diurnal phenomena is readily seen in the ascending and descending values. Antarctica exhibits a relative calibration of roughly -1.4 dB, independent of ascending or descending data. The low inter-annual variability of rainforests and Antarctica make them good candidates for future calibration sites. Averaging over all land surfaces, excluding Antarctica and Greenland, the relative calibration is -0.70 dB and -0.54 dB for ascending and descending data respectively.

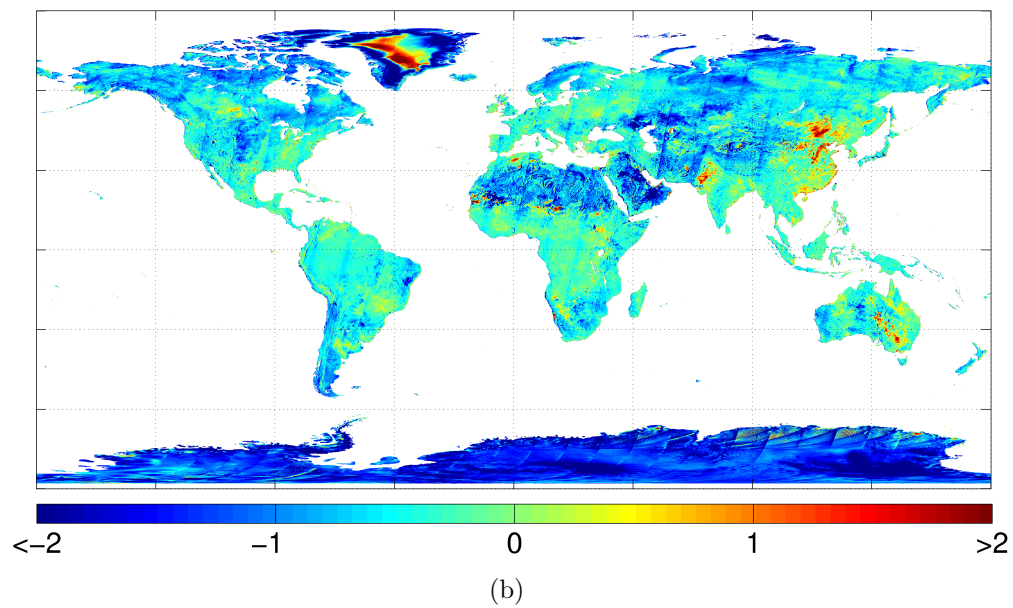
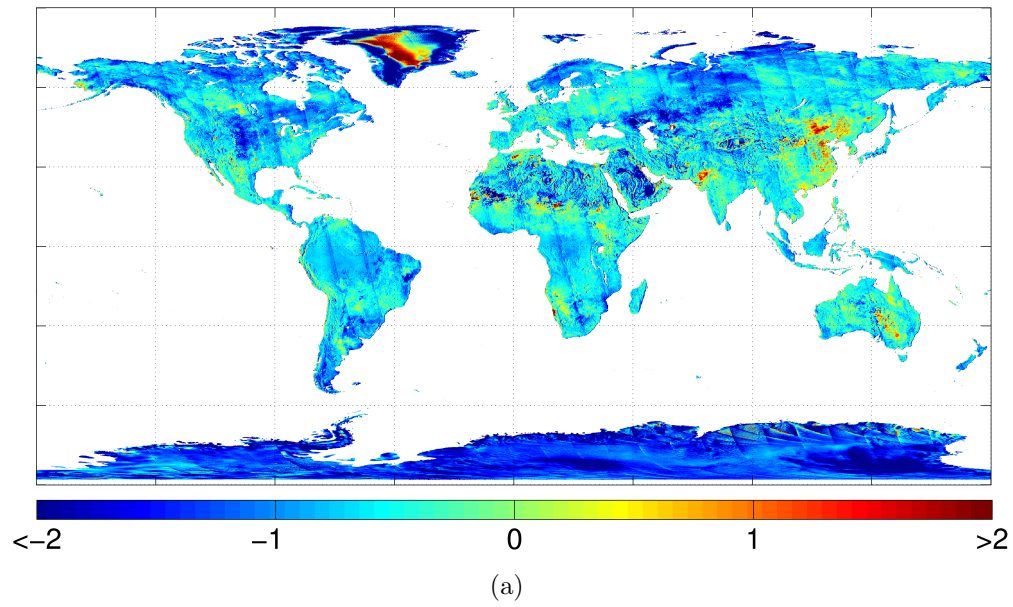


**Figure 5.4:** Difference of OSCAT 2012 and QuikSCAT 2000-2008 H-pol backscatter. The colorscale units are dB. (a) H-pol, ascending, (b) H-pol, descending.

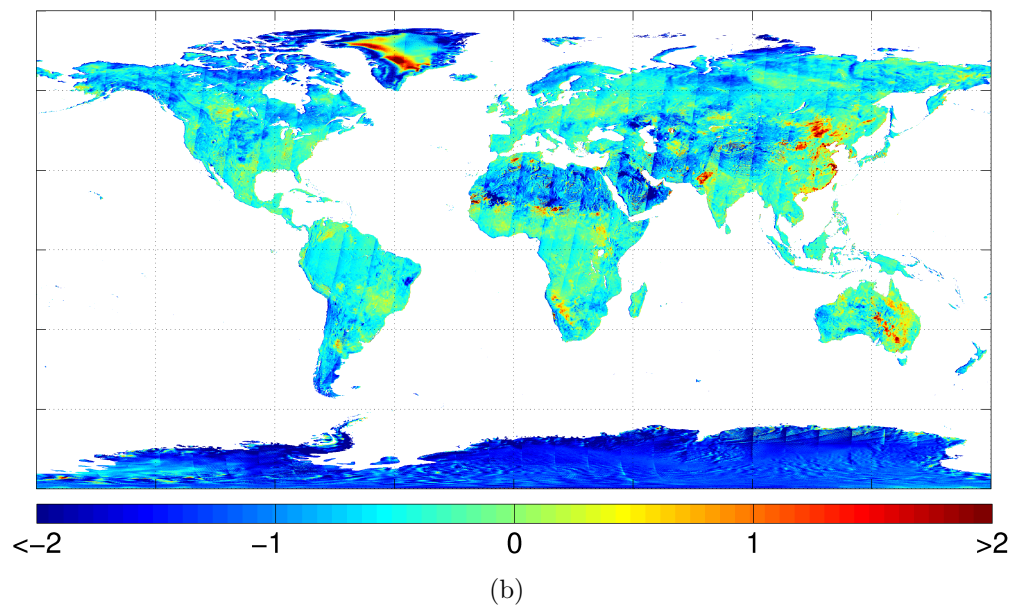
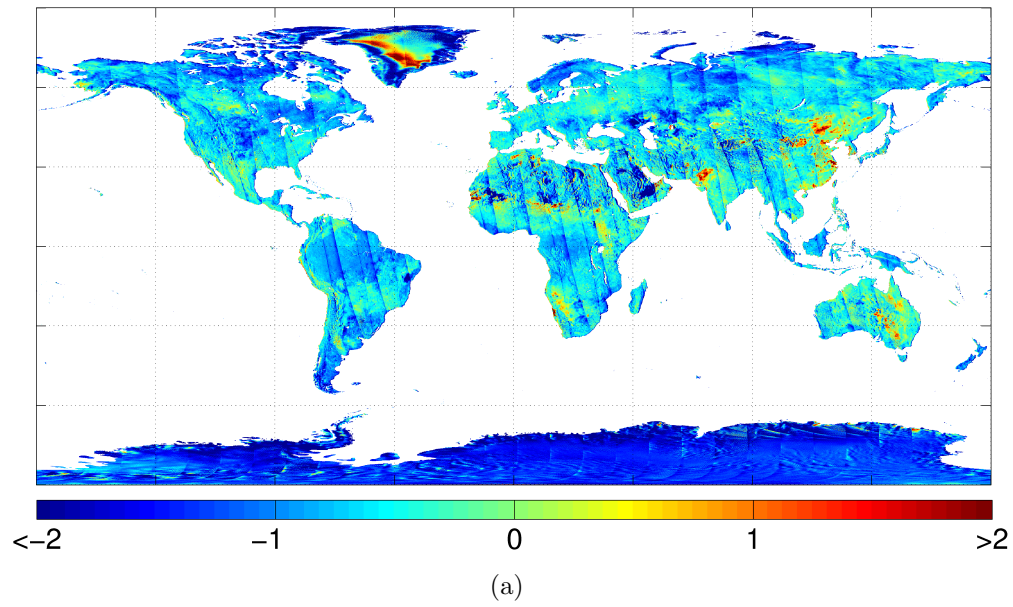


**Figure 5.5:** Difference of OSCAT 2012 and QuikSCAT 2000-2008 V-pol backscatter. The colorscale units are dB. (a) V-pol, ascending, (b) V-pol, descending.

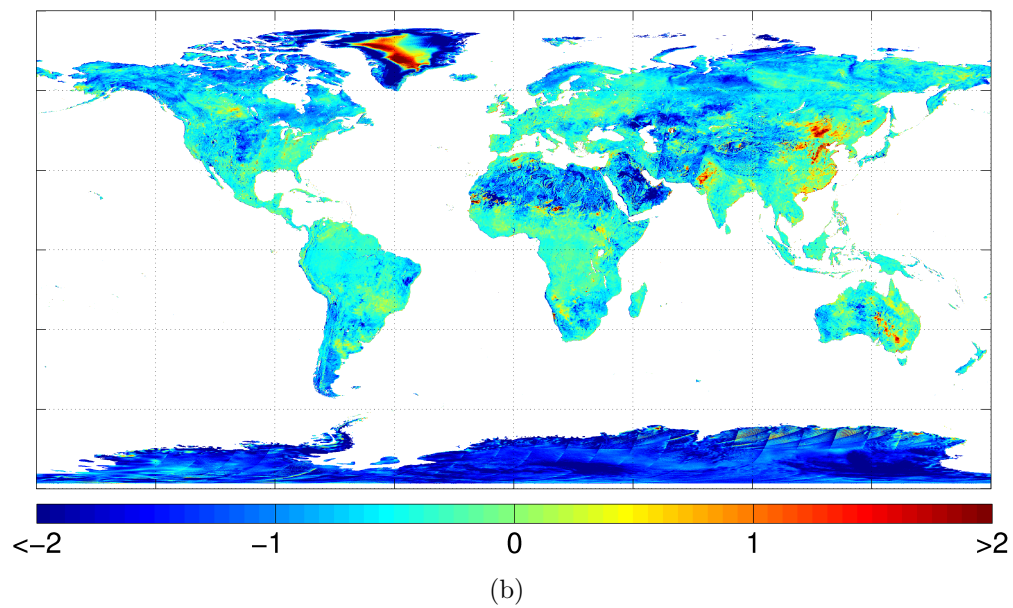
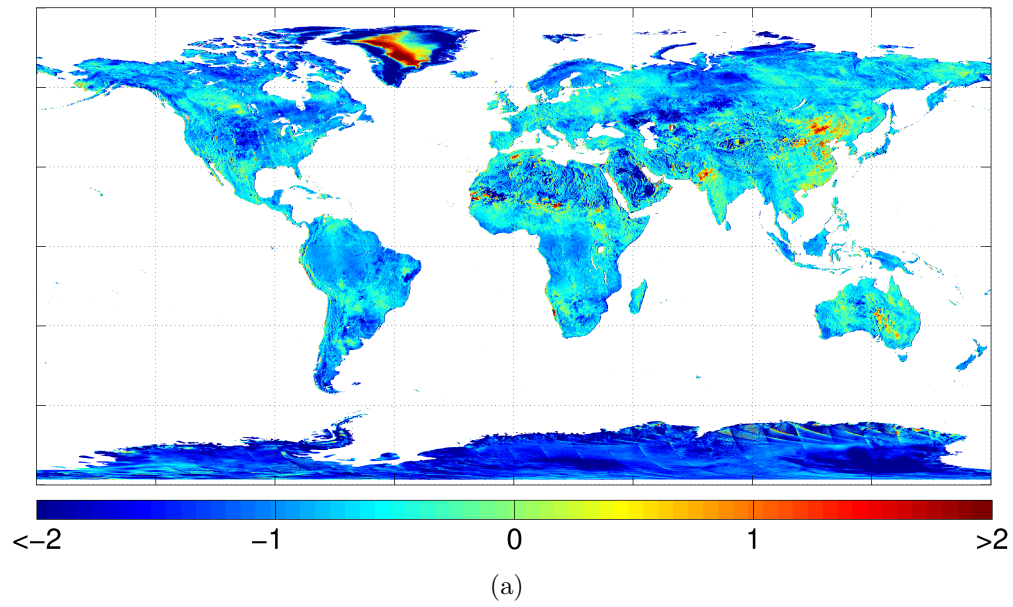


**Figure 5.6:** Difference of azimuth bias-corrected OSCAT 2012 and QuikSCAT 2000-2008 H-pol backscatter. The colorscale units are dB.(a) H-pol, ascending, (b) H-pol, descending.

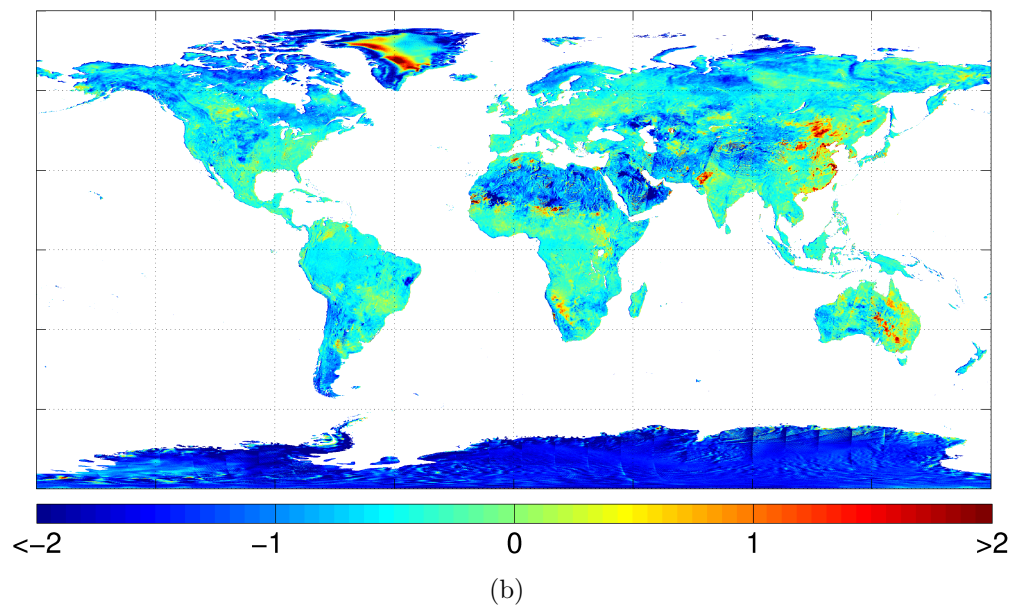
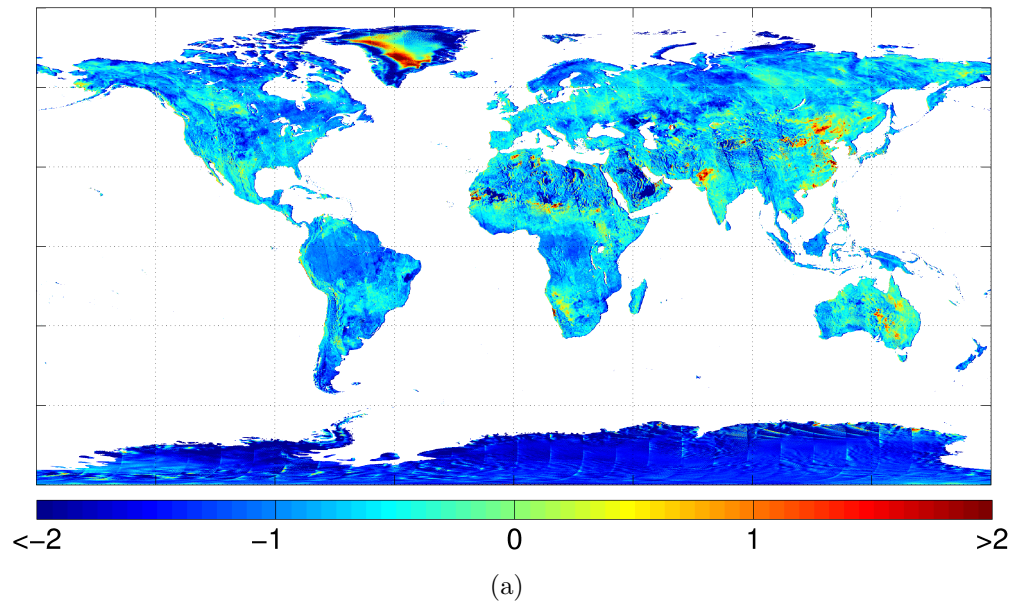
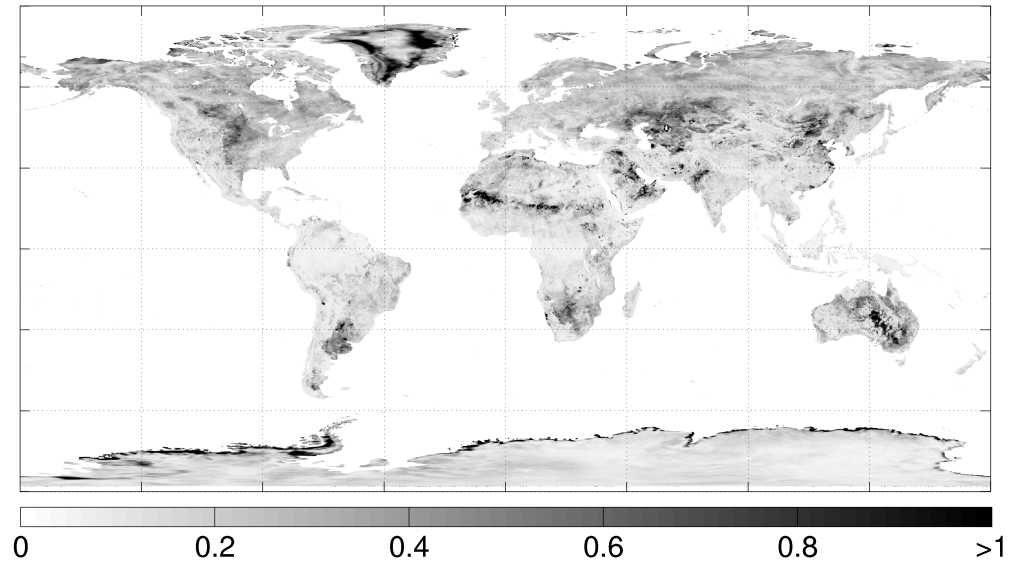
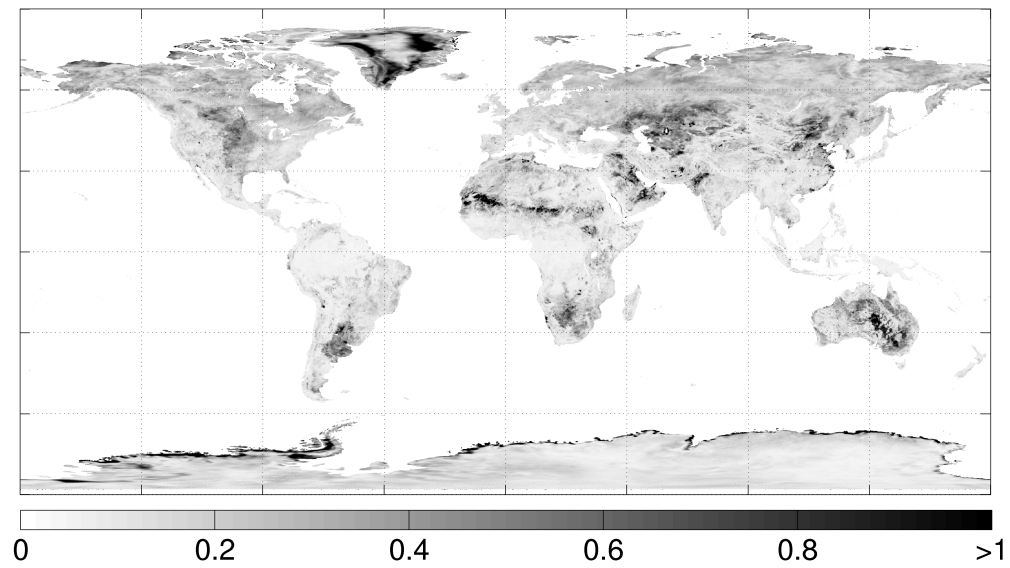


**Figure 5.7:** Difference of azimuth bias-corrected OSCAT 2012 and QuikSCAT 2000-2008 V-pol backscatter. The colorscale units are dB.(a) V-pol, ascending, (b) V-pol, descending.

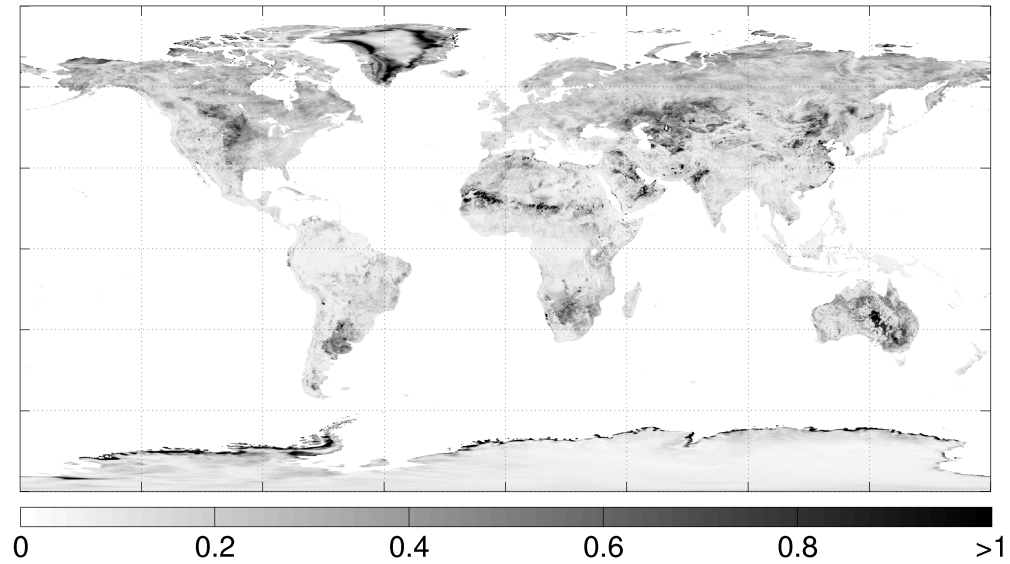


(a)

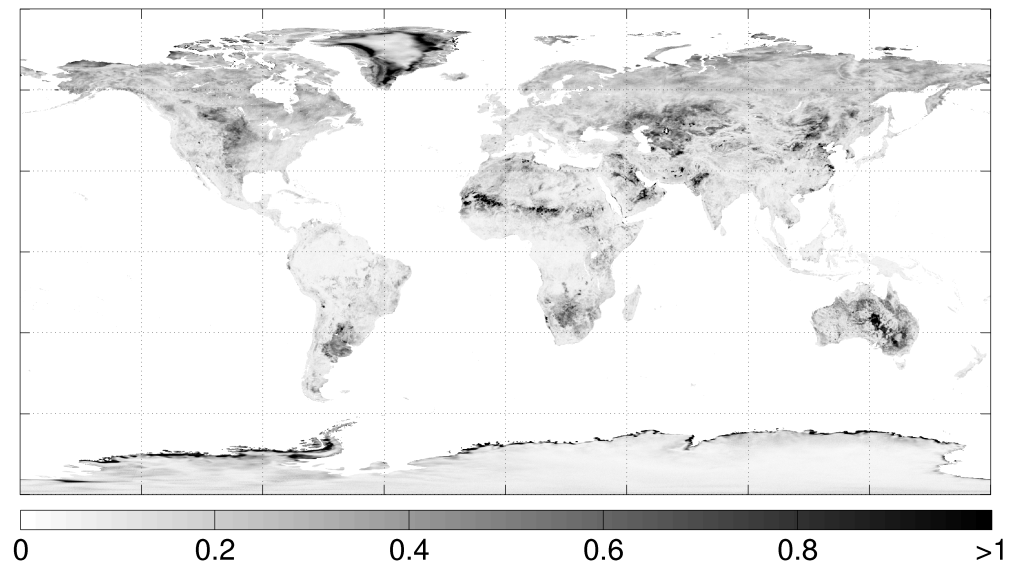


(b)

**Figure 5.8:** Standard deviation of annual means of QuikSCAT backscatter. The colorscale units are dB. (a) H-pol, ascending, (b) H-pol, descending.



(a)



(b)

**Figure 5.9:** Standard deviation of annual means of QuikSCAT backscatter. The colorscale units are dB. (a) V-pol, ascending, (b) V-pol, descending.

**Table 5.2:** Relative calibration numbers for several regions. Units are in dB.

Target	Relative Calibration			
	H-pol, Asc.	H-pol, Des.	V-pol, Asc.	V-pol, Des.
Amazon	-0.79	-0.39	-0.91	-0.51
Congo	-0.87	-0.29	-0.97	-0.43
Indonesia	-0.78	-0.22	-0.92	-0.34
Antarctica	-1.44	-1.43	-1.40	-1.31
World	-0.70	-0.54	-0.70	-0.54

## 5.2 Model-Based Approach

As seen above, the high inter-annual variability of certain regions prohibits using direct-comparison methods to understand the seasonal variation of the relative calibration. In this section, we model the backscatter as a function of environment variables in order to resolve seasonal variation of the relative calibration. There are several environmental factors that affect seasonal backscatter trends and their effects may be coupled. We take a simplistic approach and consider only a few variables assumed to be the dominant factor in seasonal backscatter variability. Specifically, we examine the effects of vegetation density in Section 5.2.1 and freeze-thaw status in Section 5.2.2, respectively. Using collocated backscatter and environmental data, we derive backscatter models and calculate the relative calibration as in Eq. 3.5.

### 5.2.1 Seasonal Effects of Vegetation on Relative Calibration

A primary contributor to the backscatter of tropical and subtropical regions is volume backscatter from vegetation. Different vegetation and terrain types have different scattering characteristics which create locational variation in the QuikSCAT and OSCAT backscatter and relative calibration of the surface [31]. Because vegetation density and its scattering characteristics vary seasonally, some regions may exhibit a relative calibration that is time dependent. In this section we identify regions whose backscatter is sensitive to vegetation changes and model the backscatter/vegetation relationship to estimate the seasonal relative calibration. We use collocated  $\sigma^0$  and vegetation data over several locations that are representative of common terrain types.

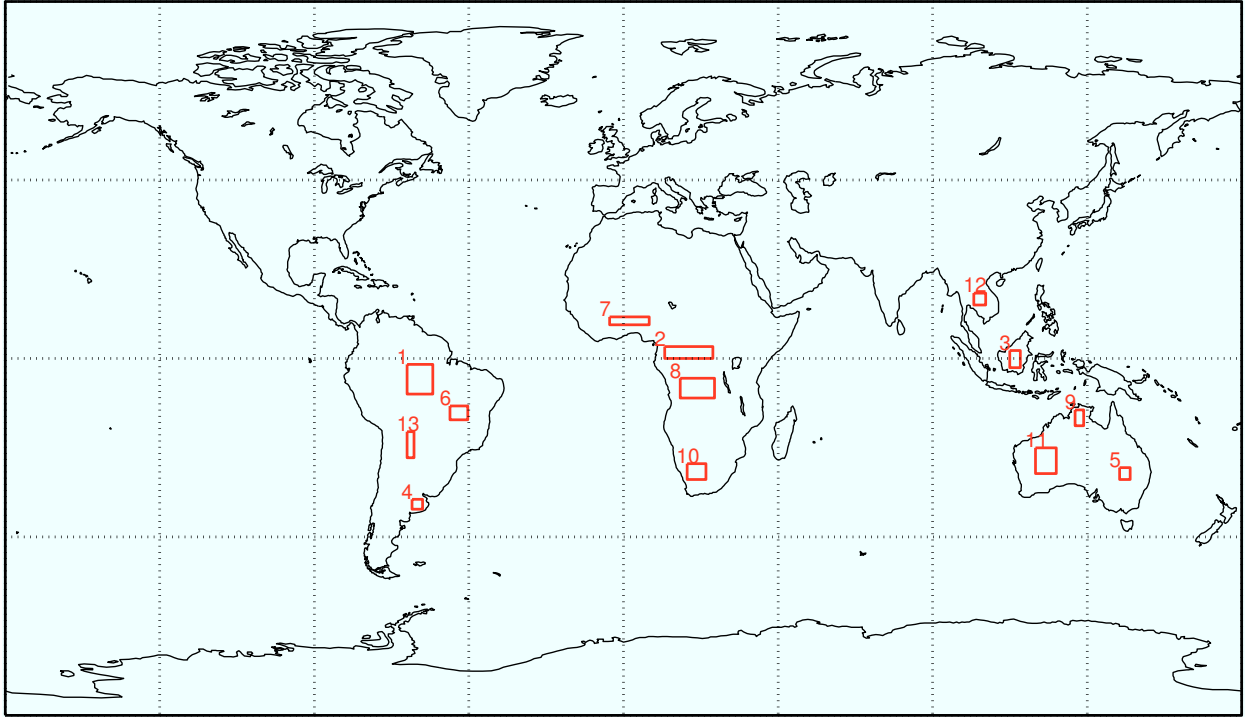


**Figure 5.10:** Regions of interest comprising different terrain types.

## Regions of Interest

The regions chosen for this study are limited to the tropic and subtropic latitudes to avoid the effects of other environmental variables such as freeze-thaw. Several regions representing major vegetation classes in the tropics and subtropics are selected. Using a map delineating the various ecoregions of the world [43], we choose regions covered by tropical rain and dry broadleaf forests, grasslands, savannas, and deserts. These regions are outlined in Figure 5.10 and documented in Table 5.3. They are similar to those chosen by Kennett and Li in their study of global scattering characteristics [31]. The sizes of the regions are chosen to be small enough to capture homogeneous terrain while allowing enough measurements to be statistically useful.

## Vegetation Data

For vegetation data, we use the Normalized Difference Vegetation Index (NDVI). Though there are many environmental factors which influence NDVI [44, 45], it has been

**Table 5.3:** Tropical and Subtropical Regions of Interest.

No.	Region	Terrain	Latitude (°)		Longitude (°)	
1	Amazon Basin	Tropical	1.5S	9.0S	63.0W	55.5W
2	Congo Basin	rainforest	3.0N	0.0N	12.0E	26.0E
3	Borneo		2.0N	2.5S	112.5E	115.5E
4	Argentine Pampas	Temperate	35.5S	38.0S	61.5W	56.5W
5	E. Australia	grassland/savanna	27.5S	30.5S	144.5E	147.5E
6	S. Brazil		12.0S	15.5S	50.5W	45.5W
7	N. Africa	Tropical	10.5N	8.5N	4.0W	7.5E
8	Mid-Africa	grassland/savanna	5.0S	10.0S	16.5E	26.5E
9	N. Australia		13.0S	17.0S	131.5E	134.0E
10	S. Africa	Desert	26.5S	30.5S	18.5E	24.0E
11	W. Australia		22.5S	29.0S	120.0E	126.0E
12	Thailand	Tropical	16.5N	13.5N	102.0E	105.5E
13	W. Argentina	dry forest	18.5S	25.0S	63.0W	61.0W

shown to be correlated with green vegetation amount [46, 47]. We use NDVI as a proxy for vegetation density, while recognizing that other environmental variables such as soil moisture and precipitation may affect NDVI. The NDVI is derived from the surface reflectances of the near-infrared and visible spectra due to solar radiation and is defined as

$$\text{NDVI} = \frac{\rho_N - \rho_R}{\rho_N + \rho_R}, \quad (5.1)$$

where  $\rho_N$  and  $\rho_R$  are the reflectances in the near-infrared and visible spectrum respectively. NDVI values range from -1 to 1 with negative and small positive values generally indicating the presence of bare soil and increasing positive values indicating the presence of vegetation.

NDVI data is available from the Terra satellite and is gridded at a 0.05 degree resolution and composited into 16-day intervals [48]. To more closely match the resolution of the scatterometer, the NDVI data is resampled at 30-km resolution, then collocated with corresponding QuikSCAT and OSCAT  $\sigma^0$  measurements for the entire years of 2000-2008 and 2012, respectively, over the regions in Figure 5.10. The collocated data are further analyzed below.

## Analysis

We first note the seasonal dependence of NDVI and backscatter. To illustrate the dependence in the tropical grassland/savanna regions, in Figure 5.11 we plot average NDVI for the South Brazil region over a few years. Figures 5.12-5.13 show the corresponding QuikSCAT backscatter mean and standard deviation. There are seasonal shifts and amplitude differences in the NDVI for each year. This inter-annual variability of the environment adds to the uncertainty of the relative calibration estimate using the direct-comparison methods above. We note in the plots a positive relationship between NDVI and backscatter. Higher NDVI values correspond with a higher mean and lower deviation in  $\sigma^0$ . These trends are common among all tropical grassland/savanna regions studied. Though not shown here, we examined NDVI and  $\sigma^0$  time series for the other regions of interest in Figure 5.10. We found that for rainforest regions, NDVI and backscatter mean and variance remain approximately constant throughout the year. Desert regions exhibit slight seasonal increases and decreases in NDVI and backscatter, though their peaks and troughs are not aligned. Temperate grassland/savanna and tropical dry forest regions exhibit mixed results. For regions that are highly cultivated, such as the Argentine Pampas and Thailand, NDVI and backscatter trends follow each other. The relationship between NDVI and backscatter is unclear for less-cultivated regions such as western Argentina and Australia.

The correlation coefficient,  $\rho$ , between NDVI and backscatter is calculated for each region and shown in Table 5.4. Only data that lie within  $\pm 1$  standard deviation of the seasonal mean NDVI value are considered in the calculation to avoid the effect of outliers. Rainforest and desert regions exhibit a correlation coefficient less than 0.3. Tropical grassland/savanna regions have a correlation consistently between 0.5 to 0.8. Correlation in temperate grasslands and tropical dry forests is dependent on whether the region is highly cultivated.

The low correlation coefficients for rainforest and desert regions in Table 5.4 indicate that QuikSCAT and OSCAT backscatter are relatively insensitive to NDVI and therefore the relative calibration is insensitive to NDVI as well. For rainforest regions, the NDVI values are likely saturated and independent of the actual vegetation amount and scattering characteristics [49, 50]. As noted above, there appears to be very little seasonal dependence in the

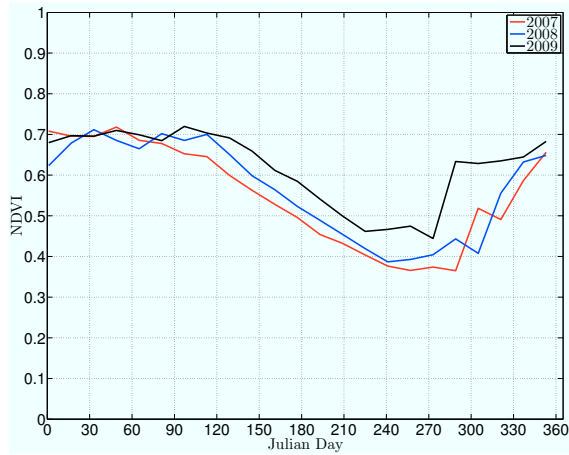


**Figure 5.11:** Seasonal NDVI response over region 6, South Brazil savanna.

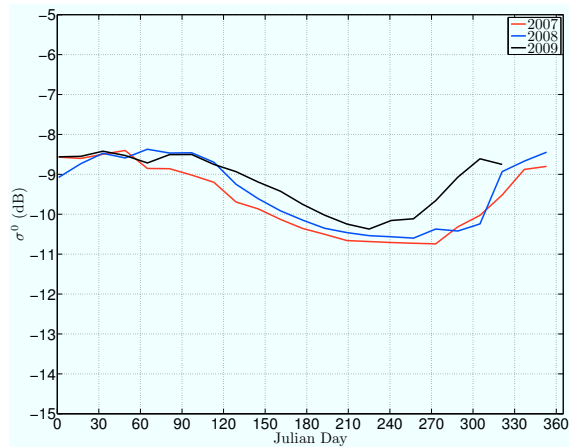


**Figure 5.12:** Seasonal QuikSCAT-measured  $\sigma^0$  over region 6, South Brazil savanna. Only H-Pol, ascending measurements are used in this plot, though similar trends exist for all flavors of  $\sigma^0$ .

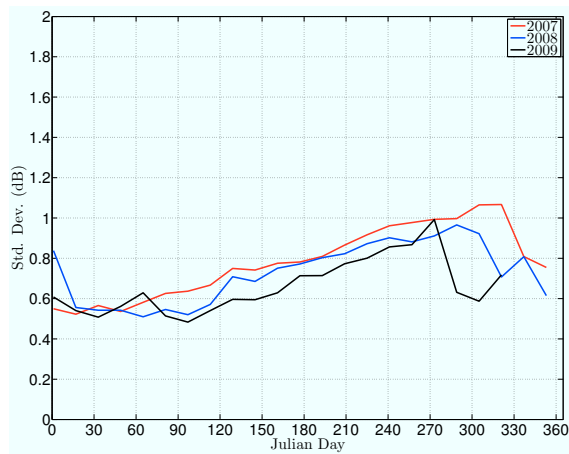


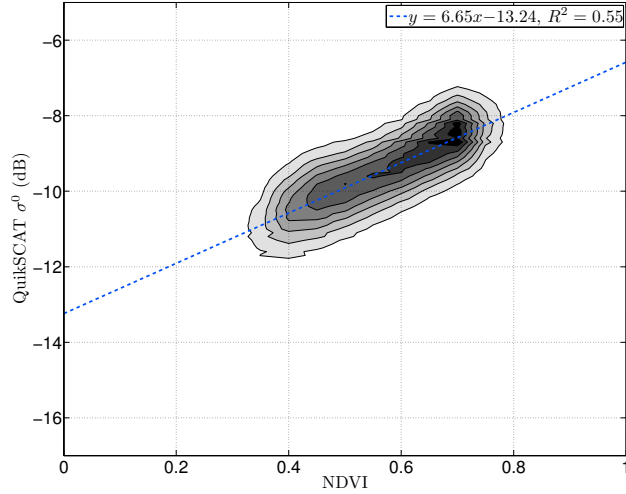
**Figure 5.13:** Standard deviation in QuikSCAT H-Pol, ascending  $\sigma^0$  over South Brazil savanna.

**Table 5.4:** Correlation coefficients between NDVI and ascending backscatter. Uncorrected OSCAT backscatter is used here, though similar results hold for azimuth-corrected data.

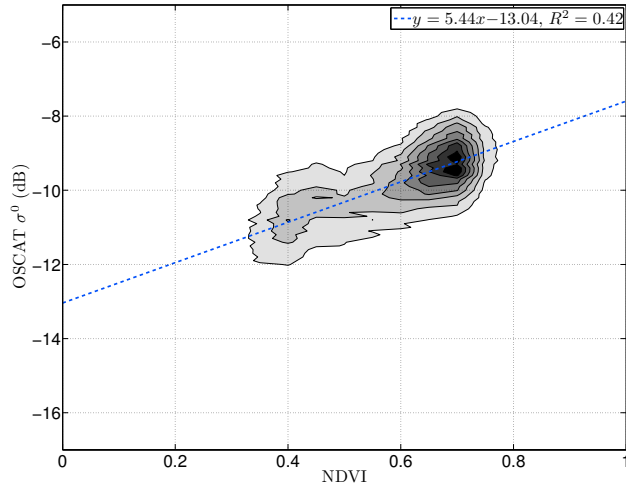
No.	Region	NDVI/QS $\rho$		NDVI/OS $\rho$	
		H-Pol	V-Pol	H-Pol	V-Pol
1	Amazon Basin	0.22	0.23	0.25	0.21
2	Congo Basin	0.05	0.05	-0.02	0.18
3	Borneo	0.25	0.30	0.15	0.20
4	Argentine Pampas (cultivated)	0.46	0.64	0.59	0.70
5	E. Australia	0.34	0.36	0.20	0.22
6	S. Brazil	0.74	0.74	0.65	0.67
7	N. Africa	0.80	0.79	0.71	0.67
8	Mid-Africa	0.70	0.66	0.57	0.51
9	N. Australia	0.60	0.62	0.50	0.59
10	S. Africa	0.01	-0.02	0.08	0.16
11	W. Australia	-0.17	-0.23	-0.08	-0.14
12	Thailand (cultivated)	0.81	0.88	0.66	0.72
13	W. Argentina	0.18	0.01	0.07	-0.09

relative calibration over rainforest regions, so we do not consider rainforest regions further in our analysis here. Desert regions also have low correlation because the peaks and troughs of NDVI and backscatter are often not aligned. Other environmental variables may be at work in the desert's backscatter response which need to be considered to obtain an accurate estimate of the relative calibration. For these reasons, we do not consider desert regions further in the following analysis. Cultivation appears to increase the correlation between NDVI and backscatter for temperate grassland and tropical dry forest regions. Therefore, NDVI may be useful in estimating the relative calibration for cultivated regions. Less-cultivated regions exhibit lower correlation, implying that NDVI is not as useful for this purpose. The higher correlation between NDVI and backscatter over tropical grassland/savanna regions indicates that NDVI information may aid in relative calibration estimation for these regions. The remainder of this section considers only tropical grassland/savanna regions.

Linear regression is performed on collocated NDVI-backscatter data for tropical grassland/savannas. A typical result is shown in Figure 5.14 for the South Brazil region. Here we see a positive trend in QuikSCAT and OSCAT backscatter and different coefficients in the best-fit lines. Assuming that no other environmental variables affect the scattering of this



(a)



(b)

**Figure 5.14:** Scatterplot and regression line of (a) NDVI/QuikSCAT backscatter and (b) NDVI/uncorrected-OSCAT backscatter for South Brazil savanna. Backscatter is H-pol, ascending.

region, the difference of the two lines is the relative calibration as a function of NDVI. We express this as

$$\begin{aligned}
 F(\text{NDVI}) &= (m_{OS} - m_{QS}) \times \text{NDVI} + (b_{OS} - b_{QS}) \\
 &= M \times \text{NDVI} + B,
 \end{aligned}
 \tag{5.2}$$

**Table 5.5:** Summary of the relative calibration of H-pol, ascending backscatter as a function of NDVI for tropical grassland/savanna regions.

No.	Region	NDVI/QS $R^2$	NDVI/OS $R^2$	$M$ (dB/NDVI)	$B$ (dB)	Avg. $F$ (dB)
6	S. Brazil	0.55	0.42	-1.21	0.20	-0.48
7	N. Africa	0.64	0.50	-0.65	-0.08	-0.37
8	Mid Africa	0.49	0.33	-1.12	-0.06	-0.81
9	N. Australia	0.37	0.25	-1.38	-0.01	-0.58

**Table 5.6:** Summary of the relative calibration of V-pol, ascending backscatter as a function of NDVI for tropical grassland/savanna regions.

No.	Region	NDVI/QS $R^2$	NDVI/OS $R^2$	$M$ (dB/NDVI)	$B$ (dB)	Avg. $F$ (dB)
6	S. Brazil	0.55	0.45	-1.61	0.47	-0.44
7	N. Africa	0.63	0.45	-1.02	-0.02	-0.48
8	Mid Africa	0.43	0.26	-1.98	0.50	-0.82
9	N. Australia	0.38	0.36	-1.13	0.24	-0.23

where  $F$  is the relative calibration with units of dB and the  $m$  and  $b$  variables are the individual best-fit linear coefficients.

Using uncorrected OSCAT data, the  $M$  and  $B$  coefficients and  $R^2$  values of the fitted lines are calculated and shown in Tables 5.5-5.6 for ascending data. All collocated NDVI values are used in Eq. 5.2 and the results are averaged to produce a seasonally-averaged estimate of  $F$ , also shown in the tables. We note that the  $M$  and  $B$  coefficients vary by region, indicating that the relative calibration is possibly dependent on vegetation type.  $M$  is a measure of how sensitive the relative calibration is to NDVI. For high  $M$  values, seasonal fluctuations in vegetation cause large fluctuations in the relative calibration. Using azimuth-corrected OSCAT data to calculate  $M$  and  $B$  coefficients produces similar results. We find that the difference in  $M$  and  $B$  coefficients between uncorrected and corrected data produces a change less than 0.05 dB in the estimated relative calibration over the range of NDVI values.

## Discussion

Because only OSCAT 2012 data is used in the analysis above, the inter-annual variability of the coefficients  $m$  and  $b$  affects the accuracy of the results in Tables 5.5-5.6. Using QuikSCAT 2000-2008 data and corresponding NDVI data, the variability of yearly  $m$  and  $b$  coefficients are calculated. It is found that for the tropical savanna regions studied above, the variability of  $m$  and  $b$  is approximately 0.5 dB/NDVI and 0.3 dB respectively. These values can create an error in the relative calibration estimate as large as 0.7 dB over the range of typical NDVI values. Other environmental variables such as soil moisture exist which influence the backscatter and relative calibration for a region, especially in tropical and subtropical latitudes. The unknown effects of these variables on  $\sigma^0$  are a limiting factor in estimating the relative calibration and its temporal variation. We thus conclude that, while linear relationships between backscatter and NDVI exist, the use of only a year of OSCAT data and the inter-annual variability of average NDVI prohibits estimating the seasonal relative calibration reliably.

### 5.2.2 Effects of Freeze-Thaw on Relative Calibration

Approximately 50 million km<sup>2</sup> of the Earth's land surface above 40° latitude undergo abrupt transitions from frozen to thawed conditions [28]. These freeze-thaw (FT) cycles can have vary by up to 6 weeks or more between years [51]. The scattering characteristics of the affected land depend greatly on the phase of water at its surface. Because of changes in the dielectric constant between frozen and liquid water, Ku-band backscatter can vary by several dB in some regions [52,53]. In this section, we examine the relationship of freeze-thaw status and the QuikSCAT/OSCAT calibration. This section proceeds similar to the previous section. Several study regions are selected over which QuikSCAT and OSCAT backscatter is collocated with FT data. The relative calibration is analyzed under frozen and thawed conditions and the inter-annual variability of regional backscatter is examined.

### Regions of Interest

We arbitrarily choose several regions to study that possess different terrain characteristics. These regions, shown in Figure 5.15, include Boreal forests, tundra and cultivated

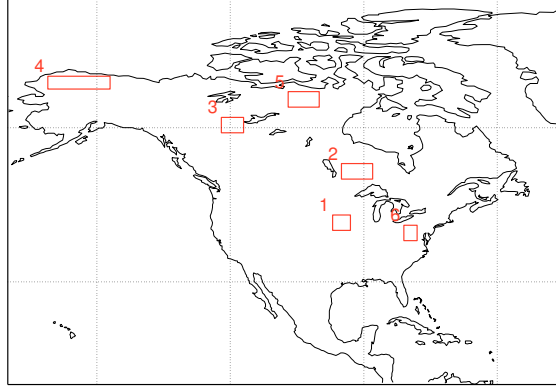


**Figure 5.15:** Regions of interest comprising different terrain types.

**Table 5.7:** Freeze-thaw regions of interest.

No.	Terrain
1	Grassland
2	Boreal Forest
3	Boreal Forest
4	Tundra
5	Tundra
6	Temperate Forest

grasslands. The region type and location are documented in Table 5.7. All regions are known to experience freeze-thaw transitions throughout the year. Having regions that differ by terrain and location allows the possibility of identifying certain locational dependencies in the relative calibration.

### Freeze-Thaw Data

Freeze-thaw data is obtained from the National Snow and Ice Data Center [54]. The data is produced at 25-km resolution and contains a global, daily record of the freeze-thaw status. The status is derived from brightness temperature measurements provided by the AMSR-E radiometer. Quality information is provided that represents the approximate accuracy of classification. We select data that have accuracies better than 90%. The FT dataset ranges from 2002-2011, which does not encompass the contiguous 2012 OSCAT dataset used in the previous analyses. For this section, we employ OSCAT 2011 data and

QuikSCAT 2003-2008 data. As shown in Chapter 4, there is a slight decrease in OSCAT backscatter between 2011 and 2012. Therefore, the relative calibration values obtained here may not be applicable to the most recent OSCAT data, however the results do indicate a general seasonal trend in the relative calibration.

## Analysis

The freeze-thaw and backscatter data described above are collocated over the regions of interest in Figure 5.15 for the day ranges JD 1-21 and JD 181-201. The day ranges are chosen to obtain a sufficient amount of collocations for the freeze and thaw states. Averages are computed for backscatter over frozen and thawed ground. The inter-annual variability of the mean backscatter is also computed using QuikSCAT data. In Figure 5.16, we plot the means of QuikSCAT and uncorrected OSCAT backscatter for the frozen and thawed states. The error bars on the QuikSCAT means represent the observed inter-annual variability in 2003-2008. We first note the general decrease in backscatter between frozen and thawed states for Boreal forest and tundra regions, while the grassland and temperate forest exhibit an increase instead. The inter-annual variability of QuikSCAT data is larger for frozen surfaces than thawed. This may be due to the wide range of snow depth and conditions (i.e. wet/dry snow) that are present under frozen conditions.

A simple model of the relative calibration for a given location as a function of FT state is described as

$$F(\gamma) = \begin{cases} c_f & : \gamma = \text{Frozen} \\ c_t & : \gamma = \text{Thawed} \end{cases}, \quad (5.3)$$

where  $F$  is the relative calibration,  $\gamma$  is the FT state, and  $c_f$  and  $c_t$  are constants. In Figure 5.17, the difference in QuikSCAT and OSCAT backscatter is plotted in for the FT states. The plot includes the same error bars from the previous plot to indicate the accuracy of the relative calibration estimate. For the regions studied,  $c_t$  is generally larger than  $c_f$  for forest and grassland regions. Tundra regions exhibit large inter-annual variability which prohibits accurately resolving seasonal variation in the calibration. Similar results hold when using azimuth-corrected OSCAT data in the comparisons.

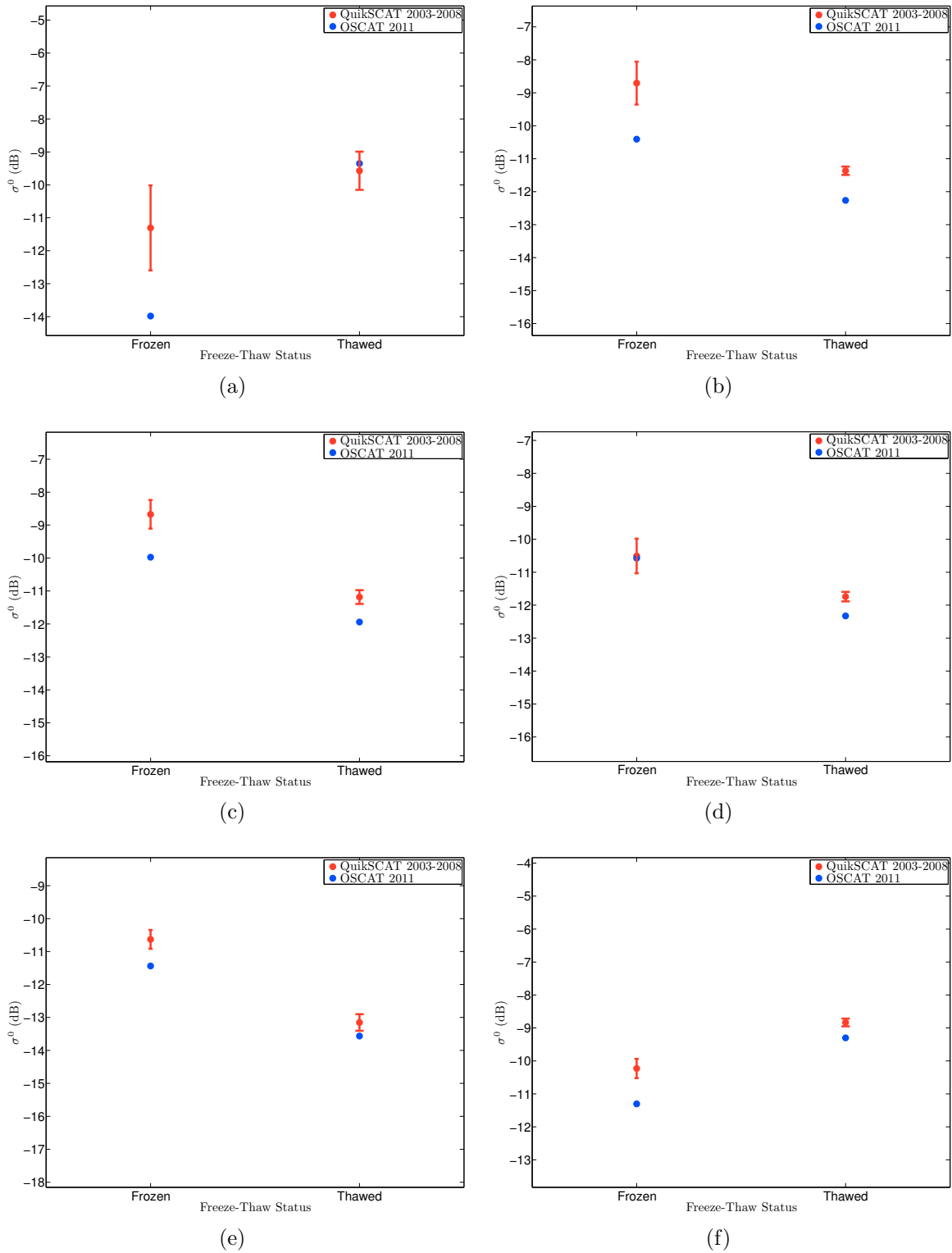


**Figure 5.16:** Average H-pol, ascending backscatter values of uncorrected OSCAT 2011 and QuikSCAT 2003-2008 data for the regions in Figure 5.15. (a)-(f) correspond to regions 1-6, respectively. The red error bars represent inter-annual variability of the QuikSCAT data.

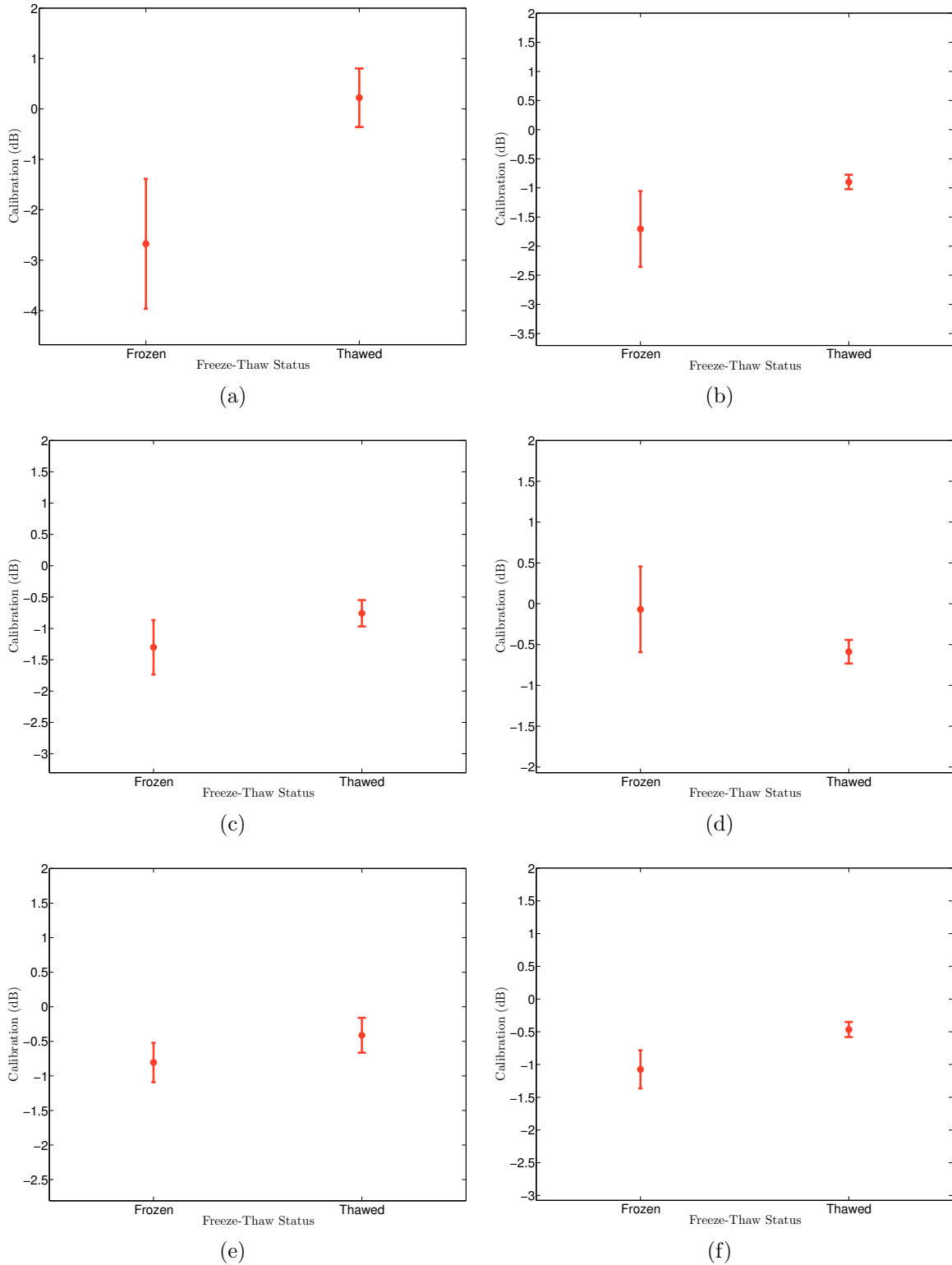


**Figure 5.17:** Relative calibration estimate for H-pol, ascending backscatter values of uncorrected OSCAT 2011 and QuikSCAT 2003-2008 data for the regions in Figure 5.15. (a)-(f) correspond to regions 1-6, respectively. The red error bars represent inter-annual variability and are provided to give an idea of the accuracy of the relative calibration estimate.

With the advent of more FT and calibrated OSCAT data, we expect to resolve the seasonal variation more accurately; however with only one available year of simultaneous OSCAT and FT data, it is difficult to characterize the behavior of the relative calibration based on FT state. We recognize that there are other environmental variables that contribute to radar scattering and possibly the relative calibration. Among these are soil moisture, vegetation, and snow characteristics [4, 55]. A more comprehensive model-based QuikSCAT/OSCAT calibration should consider these additional variables.

### 5.3 Summary

Direct and model-based comparisons of QuikSCAT and OSCAT data are performed to estimate the relative calibration term  $F$  in Eq. 3.2, which generally varies by time and location. Because the amount of OSCAT data available for comparison is small, the accuracy of the estimate is limited by the inter-annual variability of the surface, which is estimated from the extensive QuikSCAT dataset. We expect the relative calibration estimate to be accurate for regions of small inter-annual variability. Direct comparisons are performed on regional and global scales and over intervals of 20 days and one year. For the majority of the regions examined, using 20-day intervals for comparison is prohibitive for resolving the seasonal variation of the relative calibration because of the inter-annual variability of the surface. Evidence of no seasonal variability in the calibration over rainforests is found. Comparing year-averaged backscatter yields relative calibration maps that detail locational dependencies in the calibration. The maps exhibit features consistent with our understanding of scattering that occurs at the surface. The average relative calibration over land surfaces is found to be approximately -0.70 dB and -0.54 dB for ascending and descending data, respectively. Models of the relative calibration as a function of vegetation density and freeze-thaw status are developed to attempt to resolve the seasonal variation of  $F$ . Evidence is found that the calibration depends linearly on vegetation density for certain regions and that there is a change in relative calibration according to FT state. In all cases, the accuracy of relative calibration estimates depend on the inter-annual variability of the surface. With future OSCAT data, a more accurate estimate of OSCAT's seasonal backscatter response

may be produced and more reliable estimates of the relative calibration may be derived from the methods of this chapter.

## Chapter 6

### Conclusion

The ten-year Ku-band data record produced by QuikSCAT has proven its utility in a variety of land studies. Intercalibrating the QuikSCAT dataset with other scatterometer datasets will enable further geophysical research, particularly in climate studies. The Oceansat-2 scatterometer is similar in function and design to QuikSCAT and its backscatter data may be used to aid in such research. In this thesis, statistical comparisons of temporally-disjoint QuikSCAT and OSCAT data are performed to estimate the relative calibration, or difference in measurements, between sensors.

This thesis presents a simple measurement model that relates QuikSCAT and OSCAT land measurements. The model terms represent measurement error in the OSCAT system and the relative calibration between the sensor backscatter measurements. OSCAT measurement errors are identified using stable, homogeneous rainforest targets. Specifically, we identify a drift in OSCAT backscatter which includes a large drop in  $\sigma^0$  during 2010, and a subsequent decrease in backscatter from 2010 to 2012. Yearly calibration constants are calculated that can be applied to the OSCAT data to lessen the effects of drift. An azimuthal bias is also identified in OSCAT backscatter. This bias is modeled with a low-order Fourier series. Aside from small deviations due to seasonal effects, the azimuthal bias is found to be temporally stable over 2010-2012. Comparison with QuikSCAT data indicates that the OSCAT azimuthal bias is locationally dependent. The low-order similarities of the bias between locations indicate that a global correction to the data will increase the overall backscatter accuracy, though there may be regions where residual azimuthal biases exist, even after correction. The improvement in accuracy is demonstrated by comparing SIR imagery formed from original and azimuth-corrected backscatter data.

The relative calibration between QuikSCAT and OSCAT land measurements is composed of contributions due to the incidence and azimuthal responses of the land, as well as possible diurnal phenomena of the surface. Regions of the Earth that exhibit surface anisotropy and diurnal phenomena are identified. The relative calibration is estimated through direct and model-based comparisons of the backscatter data. Using direct-comparison methods, we find that comparing data over short time intervals cannot accurately resolve seasonal variation in the relative calibration for most regions because of the inter-annual variability of the land backscatter. Using year-long intervals for comparison provides a more accurate estimate of the relative calibration, especially for stable rainforest and polar regions. Locational dependencies are present in the relative calibration that correlate with different terrain and climates. Using model-based comparisons, evidence is presented that suggest seasonal dependencies in the relative calibration which are correlated with environmental variables such as vegetation density and freeze-thaw status. Because of the observed backscatter variability, however, these dependencies are difficult to quantify accurately.

## 6.1 Contributions

The following contributions result from this thesis:

1. Suggested corrections to the OSCAT dataset are provided to reduce the effect of drift and azimuth biases. The corrections improve the consistency among OSCAT land backscatter measurements. The corrections may be easily implemented into existing SIR and wind retrieval algorithms to increase the accuracy of  $\sigma^0$  values and wind vector estimates.
2. The relative calibration procedure and analyses yield medium-resolution maps that indicate the QuikSCAT/OSCAT calibration for each flavor of backscatter. These maps may aid future research that uses QuikSCAT and OSCAT data in tandem. In addition, maps are derived from QuikSCAT data which qualitatively describe the surface anisotropy and diurnal characteristics of global land surfaces. These maps give users an idea of locations where such characteristics contribute to the QuikSCAT/OSCAT calibration.

3. Relationships between  $\sigma^0$  and certain environmental variables have been found. Specifically, an approximate linear relationship of NDVI and backscatter is found over savanna/grassland regions. Knowledge of these relationships may aid future research in understanding the seasonal dependency of the relative calibration.

## 6.2 Future Work

As with all ongoing scatterometer missions, continuing work must be done to ensure consistency in OSCAT backscatter measurements. The following describe possible calibration procedures that follow from the work in this thesis:

1. The effect of the suggested azimuth corrections on OSCAT ocean wind estimates has not been determined. Wind retrieval using the azimuth-corrected backscatter should be performed. The resulting wind vector estimates may be compared against wind vectors derived from the uncorrected data to determine the effects of the azimuth corrections. The corrected wind vectors can also be compared with winds derived from computational models or *in situ* data to determine the change in absolute accuracy of the wind estimates.
2. Inter-annual variability of the surface contributes to the inaccuracy of the relative calibration estimate. We are limited in this thesis since there is a relatively limited amount of OSCAT data available for use. As more OSCAT data becomes available, a more-accurate estimate of the average OSCAT backscatter can be produced which in turn will yield a better estimate of the true relative calibration.
3. This thesis compares temporally-disjoint QuikSCAT and OSCAT data to estimate the relative calibration, which leads to inaccuracies because of surface variability between the sensor measurement times. Surface variability is not a concern for determining the relative calibration from temporally-coincident QuikSCAT and OSCAT measurements. There are a few weeks of coincident data in early 2013 where the QuikSCAT antenna rotated normally before stopping again. The comparison of QuikSCAT and OSCAT data from this period may prove useful in validating the calibration results of this thesis.

4. Sea ice is an important factor in many climatological processes. The QuikSCAT dataset has proven especially useful in sea ice applications. To give continuation to these studies with OSCAT data, an understanding of the relative calibration for the different types of sea ice is needed. Direct comparison of the sensor data for different sea ice types may yield a relative calibration estimate which could allow OSCAT data to be used in such applications.
5. The relative calibration analyses of this thesis were performed using raw  $\sigma^0$  measurements of the sensor L1B products. It has not been determined if the results apply to QuikSCAT and OSCAT SIR images. Similar analyses may be performed using QuikSCAT and OSCAT SIR images to yield relative calibration images. Subtracting the calibration images from OSCAT SIR images will provide an estimate of the QuikSCAT backscatter. In this manner, a consistent, multi-decadal QuikSCAT SIR image set that spans both sensor mission lives may be produced.

## Bibliography

- [1] F. Naderi, M. Freilich, and D. Long, “Spaceborne radar measurement of wind velocity over the ocean—an overview of the NSCAT scatterometer system,” *Proceedings of the IEEE*, vol. 79, no. 6, pp. 850–866, 1991. 1, 8
- [2] Q. P. Remund and D. G. Long, “Sea ice extent mapping using Ku band scatterometer data,” *Journal of Geophysical Research: Oceans (1978–2012)*, vol. 104, no. C5, pp. 11 515–11 527, 1999. 1
- [3] Q. Remund, D. Long, and M. Drinkwater, “An iterative approach to multisensor sea ice classification,” *Geoscience and Remote Sensing, IEEE Transactions on*, vol. 38, no. 4, pp. 1843–1856, 2000. 1
- [4] W. Wagner and K. Scipal, “Large-scale soil moisture mapping in western Africa using the ERS scatterometer,” *Geoscience and Remote Sensing, IEEE Transactions on*, vol. 38, no. 4, pp. 1777–1782, 2000. 1, 8, 21, 64
- [5] G. Chander, T. Hewison, N. Fox, X. Wu, X. Xiong, and W. Blackwell, “Overview of intercalibration of satellite instruments,” *Geoscience and Remote Sensing, IEEE Transactions on*, vol. 51, no. 3, pp. 1056–1080, 2013. 1, 14
- [6] E. Bracalente, D. Boggs, W. Grantham, and J. Sweet, “The scattering coefficient sigma-0 algorithm,” *Oceanic Engineering, IEEE Journal of*, vol. 5, no. 2, pp. 145–154, 1980. 1, 15
- [7] I. Birrer, E. Bracalente, G. Dome, J. Sweet, and G. Berthold, “Sigma-0 signature of the Amazon rain forest obtained from the Seasat scatterometer,” *Geoscience and Remote Sensing, IEEE Transactions on*, vol. GE-20, no. 1, pp. 11–17, 1982. 1, 8, 16, 76
- [8] D. Long and G. Skouson, “Calibration of spaceborne scatterometers using tropical rain forests,” *Geoscience and Remote Sensing, IEEE Transactions on*, vol. 34, no. 2, pp. 413–424, 1996. 1, 7, 8, 15, 16, 30, 76
- [9] J. Zec, W. Jones, and D. G. Long, “NSCAT normalized radar backscattering coefficient biases using homogeneous land targets,” *Journal of Geophysical Research*, vol. 104, no. C5, p. 11, 1999. 1, 32, 76
- [10] M. Freilich, H. Qi, and R. Dunbar, “Scatterometer beam balancing using open-ocean backscatter measurements,” *Journal of Atmospheric and Oceanic Technology*, vol. 16, p. 283, 1999. 1

- [11] A. Stoffelen, “A simple method for calibration of a scatterometer over the ocean,” *Journal of atmospheric and oceanic technology*, vol. 16, no. 2, pp. 275–282, 1999. 1
- [12] L. Kunz and D. Long, “Calibrating SeaWinds and QuikSCAT scatterometers using natural land targets,” *Geoscience and Remote Sensing Letters, IEEE*, vol. 2, no. 2, pp. 182 – 186, 2005. 2, 16, 20
- [13] B. Hicks and D. Long, “Diurnal melt detection on Arctic sea ice using tandem QuikSCAT and SeaWinds data,” in *Proceedings of the IEEE International Geoscience and Remote Sensing Symposium*, 2006, pp. 4112–4114. 2
- [14] T. Lee, O. Wang, W. Tang, and W. T. Liu, “Wind stress measurements from the QuikSCAT-SeaWinds scatterometer tandem mission and the impact on an ocean model,” *Journal of Geophysical Research: Oceans*, vol. 113, no. C12, pp. 1–14, 2008. 2
- [15] W. T. Liu, W. Tang, X. Xie, R. R. Navalgund, and K. Xu, “Power density of ocean surface wind from international scatterometer tandem missions,” *International Journal of Remote Sensing*, vol. 29, no. 21, pp. 6109–6116, 2008. 2
- [16] A. Elyouncha and X. Neyt, “C-band satellite scatterometer intercalibration,” *Geoscience and Remote Sensing, IEEE Transactions on*, vol. 51, no. 3, pp. 1478–1491, 2013. 2
- [17] C. Mears, D. Smith, and F. Wentz, “Detecting rain with QuikScat,” in *Geoscience and Remote Sensing Symposium, 2000. Proceedings. IGARSS 2000. IEEE 2000 International*, vol. 3, 2000, pp. 1235–1237 vol.3. 2
- [18] J. Haarpaintner, R. Tonboe, D. Long, and M. Van Woert, “Automatic detection and validity of the sea-ice edge: an application of enhanced-resolution QuikScat/SeaWinds data,” *Geoscience and Remote Sensing, IEEE Transactions on*, vol. 42, no. 7, pp. 1433–1443, 2004. 2
- [19] M. Owen and D. Long, “Simultaneous wind and rain estimation for QuikSCAT at ultra-high resolution,” *Geoscience and Remote Sensing, IEEE Transactions on*, vol. 49, no. 6, pp. 1865 –1878, 2011. 2
- [20] S. E. L. Howell, J. Yackel, R. De Abreu, T. Geldsetzer, and C. Breneman, “On the utility of SeaWinds/QuikSCAT data for the estimation of the thermodynamic state of first-year sea ice,” *Geoscience and Remote Sensing, IEEE Transactions on*, vol. 43, no. 6, pp. 1338–1350, 2005. 2
- [21] S. Jaruwatanadilok, B. W. Stiles, and A. Fore, “Cross calibration between QuikSCAT and Oceansat-2,” *Geoscience and Remote Sensing, IEEE Transactions on*, submitted 2013. 3, 10, 24, 25
- [22] S. Bhowmick, R. Kumar, and A. Kiran Kumar, “Cross calibration of the OceanSAT-2 scatterometer with QuikSCAT scatterometer using natural terrestrial targets,” *Geoscience and Remote Sensing, IEEE Transactions on*, vol. PP, no. 99, pp. 1–6, 2013. 3, 21, 24, 25, 26, 28

- [23] J. P. Bradley, “Extending the QuikSCAT data record with the Oceansat-2 scatterometer,” Master’s thesis, Brigham Young University, 2012. 3, 11, 24
- [24] P. Yoho, A. Anderson, D. Long, J. Lux, J. Adams, and F. Cheng, “SeaWinds on QuikSCAT calibration using a calibration ground station,” in *Geoscience and Remote Sensing Symposium, 2000. Proceedings. IGARSS 2000. IEEE 2000 International*, vol. 3, 2000, pp. 1039–1041 vol.3. 3, 12
- [25] J. Huddleston, W. Tsai, M. Spencer, B. Stiles, and R. Dunbar, “SeaWinds on QuikSCAT: postlaunch calibration and validation,” in *Geoscience and Remote Sensing Symposium, 2000. Proceedings. IGARSS 2000. IEEE 2000 International*, vol. 3, 2000, pp. 1024–1026 vol.3. 3, 12
- [26] R. Fischer, “Standard deviation of scatterometer measurements from space,” *Geoscience Electronics, IEEE Transactions on*, vol. 10, no. 2, pp. 106–113, april 1972. 7
- [27] M. Satake and H. Hanado, “Diurnal change of Amazon rain forest sigma-0 observed by Ku-band spaceborne radar,” *Geoscience and Remote Sensing, IEEE Transactions on*, vol. 42, no. 6, pp. 1127–1134, 2004. 7, 76
- [28] S. W. Running, J. B. Way, K. C. McDonald, J. S. Kimball, S. Frohling, A. R. Keyser, and R. Zimmerman, “Radar remote sensing proposed for monitoring freeze-thaw transitions in boreal regions,” *Eos, Transactions American Geophysical Union*, vol. 80, no. 19, pp. 213–221, 1999. 8, 21, 59
- [29] H. Stephen and D. Long, “Azimuth modulation of backscatter from SeaWinds and ERS scatterometers over the Saharo-Arabian deserts,” in *Geoscience and Remote Sensing Symposium, 2002. IGARSS '02. 2002 IEEE International*, vol. 5, 2002, pp. 2808–2810 vol.5. 8, 27
- [30] D. Long and M. Drinkwater, “Azimuth variation in microwave scatterometer and radiometer data over Antarctica,” *Geoscience and Remote Sensing, IEEE Transactions on*, vol. 38, no. 4, pp. 1857–1870, 2000. 8, 18, 27
- [31] R. Kennett and F. Li, “Seasat over-land scatterometer data. I. Global overview of the Ku-band backscatterer coefficients,” *Geoscience and Remote Sensing, IEEE Transactions on*, vol. 27, no. 5, pp. 592–605, 1989. 8, 15, 51, 52
- [32] D. Long and P. Hardin, “Vegetation studies of the Amazon basin using enhanced resolution Seasat scatterometer data,” *Geoscience and Remote Sensing, IEEE Transactions on*, vol. 32, no. 2, pp. 449–460, 1994. 8
- [33] J. Bradley and D. Long, “Estimation of the OSCAT spatial response function using island targets,” *IEEE Transactions on Geoscience and Remote Sensing*, to appear, 2013. 9, 10
- [34] C. Wu, Y. Liu, K. Kellogg, K. Pak, and R. Glenister, “Design and calibration of the SeaWinds scatterometer,” *Aerospace and Electronic Systems, IEEE Transactions on*, vol. 39, no. 1, pp. 94–109, 2003. 9, 12

- [35] T. Misra, P. Chakraborty, A. Misra, J. Rao, D. Dave, C. Rao, N. Desai, and R. Arora, "Oceansat-II scatterometer: Sensor performance evaluation, sigma-0 analyses, and estimation of biases," *Geoscience and Remote Sensing, IEEE Transactions on*, vol. PP, no. 99, pp. 1–6, 2013. 11, 26, 29
- [36] J. Zec, W. Jones, and D. Long, "SeaWinds beam and slice balance using data over Amazonian rainforest," in *Geoscience and Remote Sensing Symposium, 2000. Proceedings. IGARSS 2000. IEEE 2000 International*, vol. 5, 2000, pp. 2215–2217 vol.5. 12
- [37] D. Long, P. Hardin, and P. Whiting, "Resolution enhancement of spaceborne scatterometer data," *Geoscience and Remote Sensing, IEEE Transactions on*, vol. 31, no. 3, pp. 700–715, 1993. 12, 20
- [38] W. Tsai, J. Graf, C. Winn, J. Huddleston, S. Dunbar, M. Freilich, F. Wentz, D. Long, and W. Jones, "Postlaunch sensor verification and calibration of the NASA scatterometer," *Geoscience and Remote Sensing, IEEE Transactions on*, vol. 37, no. 3, pp. 1517–1542, 1999. 16
- [39] W. Wagner, G. Lemoine, M. Borgeaud, and H. Rott, "A study of vegetation cover effects on ERS scatterometer data," *Geoscience and Remote Sensing, IEEE Transactions on*, vol. 37, no. 2, pp. 938–948, 1999. 21
- [40] K. Padia and S. Team, "Oceansat-2 scatterometer algorithms for sigma-0, processing and products format," *Advanced Image Processing Group, Signal and Image Processing Area, Space Applications Centre, Gujarat, India*, vol. 6, p. 49, 2010. 26
- [41] S. Soisuvarn, K. Ahmad, Z. Jelanak, J. Sienkiewicz, and P. S. Chang, "NOAA assessment of the Oceansat-2 scatterometer," May 2011, slides presented at IOVWST, Annapolis, MD, USA. [Online]. Available: [http://coaps.fsu.edu/scatterometry/meeting/docs/2011/First%20OSCAT%20Results/IOVWST2011\\_NOAA\\_OSCAT\\_rev5.pdf](http://coaps.fsu.edu/scatterometry/meeting/docs/2011/First%20OSCAT%20Results/IOVWST2011_NOAA_OSCAT_rev5.pdf) 34
- [42] S. V. Nghiem, D. K. Hall, T. L. Mote, M. Tedesco, M. R. Albert, K. Keegan, C. A. Shuman, N. E. DiGirolamo, and G. Neumann, "The extreme melt across the Greenland ice sheet in 2012," *Geophysical Research Letters*, vol. 39, no. 20, pp. 1–6, 2012. 44
- [43] D. M. Olson, E. Dinerstein, E. D. Wikramanayake, N. D. Burgess, G. V. Powell, E. C. Underwood, J. A. D'amico, I. Itoua, H. E. Strand, J. C. Morrison, *et al.*, "Terrestrial ecoregions of the world: A new map of life on Earth: A new global map of terrestrial ecoregions provides an innovative tool for conserving biodiversity," *BioScience*, vol. 51, no. 11, pp. 933–938, 2001. 52
- [44] T. N. Carlson and D. A. Ripley, "On the relation between NDVI, fractional vegetation cover, and leaf area index," *Remote Sensing of Environment*, vol. 62, no. 3, pp. 241–252, 1997. 52
- [45] J. Wang, P. M. Rich, and K. P. Price, "Temporal responses of NDVI to precipitation and temperature in the central Great Plains, USA," *International Journal of Remote Sensing*, vol. 24, no. 11, pp. 2345–2364, 2003. 52

- [46] R. Myneni, F. Hall, P. Sellers, and A. Marshak, “The interpretation of spectral vegetation indexes,” *Geoscience and Remote Sensing, IEEE Transactions on*, vol. 33, no. 2, pp. 481–486, 1995. 53
- [47] C. J. Tucker, “Red and photographic infrared linear combinations for monitoring vegetation,” *Remote Sensing of Environment*, vol. 8, no. 2, pp. 127 – 150, 1979. 53
- [48] MOD13C1 dataset. NASA Land Processes Distributed Active Archive Center, 2000-2012. [Online]. Available: <https://lpdaac.usgs.gov/> 53
- [49] A. A. Gitelson, Y. J. Kaufman, and M. N. Merzlyak, “Use of a green channel in remote sensing of global vegetation from EOS-MODIS,” *Remote Sensing of Environment*, vol. 58, no. 3, pp. 289 – 298, 1996. 54
- [50] O. Mutanga and A. K. Skidmore, “Narrow band vegetation indices overcome the saturation problem in biomass estimation,” *International Journal of Remote Sensing*, vol. 25, no. 19, pp. 3999–4014, 2004. 54
- [51] S. Frolking, K. C. McDonald, J. S. Kimball, J. B. Way, R. Zimmermann, and S. W. Running, “Using the space-borne NASA scatterometer (NSCAT) to determine the frozen and thawed seasons,” *Journal of Geophysical Research: Atmospheres*, vol. 104, no. D22, pp. 27 895–27 907, 1999. 59
- [52] J. Kimball, K. McDonald, A. Keyser, S. Frolking, and S. Running, “Application of the NASA scatterometer (NSCAT) for determining the daily frozen and nonfrozen landscape of Alaska,” *Remote Sensing of Environment*, vol. 75, no. 1, pp. 113 – 126, 2001. 59
- [53] J. Kimball, K. McDonald, S. Frolking, and S. Running, “Radar remote sensing of the spring thaw transition across a boreal landscape,” *Remote Sensing of Environment*, vol. 89, no. 2, pp. 163 – 175, 2004. 59
- [54] Y. Kim, J. Kimball, K. McDonald, and J. Glassy, “Developing a global data record of daily landscape freeze/thaw status using satellite passive microwave remote sensing,” *Geoscience and Remote Sensing, IEEE Transactions on*, vol. 49, no. 3, pp. 949–960, 2011. 60
- [55] S. Nghiem and W. Tsai, “Global snow cover monitoring with spaceborne Ku-band scatterometer,” *Geoscience and Remote Sensing, IEEE Transactions on*, vol. 39, no. 10, pp. 2118–2134, 2001. 64

## Appendix A

### Geographic Regions that Exhibit Anisotropy and Diurnal Phenomena

As explained in Chapter 3, the difference between collocated QuikSCAT and OSCAT measurements ( $F$  in Eq. 3.2) is due the incidence response of the surface as well as orbital differences in the sensors. The different orbit tracks of QuikSCAT and OSCAT cause them to sample the surface at different azimuth angles and local times of day. Because of this, anisotropy and diurnal phenomena can contribute to the calibration for certain regions. In this appendix, we perform statistical analyses of QuikSCAT data to identify geographic regions that exhibit anisotropy and diurnal phenomena. We note that the contributions to the QuikSCAT/OSCAT calibration from the incidence response and orbital differences cannot be distinguished from each other. Thus, the techniques below are not meant to quantify contributions to the calibration; rather, they identify regions where anisotropy and diurnal phenomena likely contribute to the QuikSCAT/OSCAT relative calibration. The procedures are described in Section A.1. Anisotropic regions are identified in Section A.2 and regions with diurnal phenomena are identified in Section A.3.

#### A.1 Procedure

We use all backscatter measurements from the complete years (2000-2008) of the QuikSCAT dataset. The data are initially separated by polarization and ascending/descending pass and then gridded on a  $0.1^\circ$  plane, which yields four maps. For each grid element of the four maps, the measurements are further binned by azimuth angle into  $90^\circ$  bins. The average measurement count for each azimuth bin of each map is approximately 500 measurements.

To examine anisotropy, statistical analysis of the azimuth bins is performed. The average of each bin is taken, and then the standard deviation of the bin means is computed. These operations are performed for each grid element. The result is a map indicating the amount of spread between the azimuth bins. Four maps are generated corresponding to the four backscatter flavors. High deviation in the azimuth bins is expected for anisotropic regions while low deviation is expected for isotropic regions. We qualitatively analyze the resulting maps in Section A.2.

Diurnal phenomena can be identified by comparing the ascending and descending backscatter for each grid element. Because of QuikSCAT's sun-synchronous orbit, it generally measures each location (excluding high latitudes) at two different local times of day corresponding to the ascending and descending pass. The measurement times are separated by approximately 12 hours at the equator. Diurnal phenomena are detected by large differences in backscatter between ascending and descending passes. Using the gridded maps

described above, we average all measurements in each grid element to produce four maps corresponding to the four backscatter flavors. We then difference the ascending and descending maps to produce one map for each polarization. The resulting maps are used to detect diurnal phenomena in Section A.3.

## A.2 Anisotropic Regions

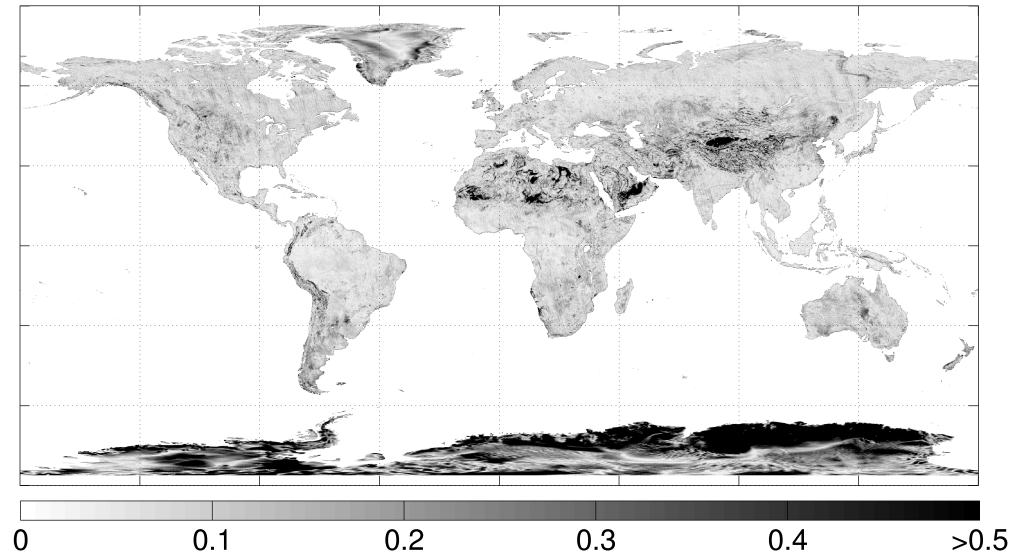
Two of the maps generated by the procedure above are shown in Figures A.1-A.2. The color scale represents the standard deviation in the azimuth bin means in dB. We note values typically less than 0.05 dB over tropical rainforest regions such as the Amazon, Congo, and Indonesian rainforests. These regions are known to be isotropic [7, 8]. Boreal forests in Canada and Siberia have average values typically below 0.09 dB. These forested regions are known to be isotropic as well [9]. Approximately half of the land grid elements (excluding Antarctica and Greenland) have pixel values below 0.09 dB. In contrast, locations that are known to be anisotropic, such as the deserts and mountains of Africa and Asia, have pixel values that typically exceed 0.4 dB. We note that some regions appear darker in one polarization over the other, indicating that the anisotropy of certain regions is polarization dependent. Though we cannot exactly quantify the contribution that a difference in azimuth angle makes to the QuikSCAT/OSCAT relative calibration, the pixel values in Figures A.1-A.2 indicate that the contribution may be on the order of a few tenths of a decibel for anisotropic regions.

## A.3 Regions with Diurnal Phenomena

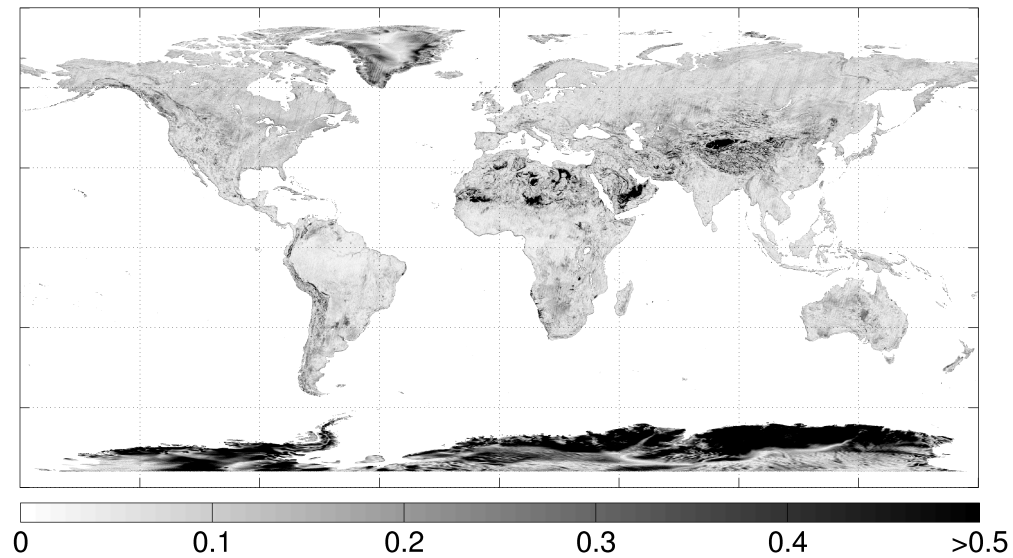
The difference of the mean ascending and mean descending backscatter is shown in Figure A.3. Dark regions indicate a large difference in backscatter and light regions indicate little change. Regions such as the Amazon, Congo, and Indonesian rainforests exhibit a difference between 0.4-0.6 dB. This difference is most likely caused by changes in dew concentration between ascending and descending passes [7, 27]. In contrast, the Boreal forest regions in Siberia and Canada exhibit a difference of between 0.1-0.2 dB. There are a few desert and mountain regions that also exhibit large differences in ascending and descending backscatter, however these differences arise from anisotropy, rather than diurnal phenomena. The diurnal phenomena evident in Figure A.3 are sampled at a 12-hour period at the equator. It is likely that they contribute to the QuikSCAT/OSCAT relative calibration, which is defined by a six-hour LTD difference at the equator.

## A.4 Summary

In this appendix, we have performed statistical analyses of QuikSCAT data to identify regions that exhibit anisotropy and diurnal phenomena. The relative calibration of QuikSCAT and OSCAT over such regions likely contains a contribution resulting from these effects. We have noted several qualitative results. Anisotropy is found to occur mainly in desert and mountainous regions, while approximately half of the land surfaces appear to be isotropic. Tropical rainforests are found to be especially isotropic. Given the variability in the azimuth bin averages over anisotropic regions, the relative calibration due to anisotropy may be on the order of a few tenths of a decibel. Diurnal phenomena are found to occur



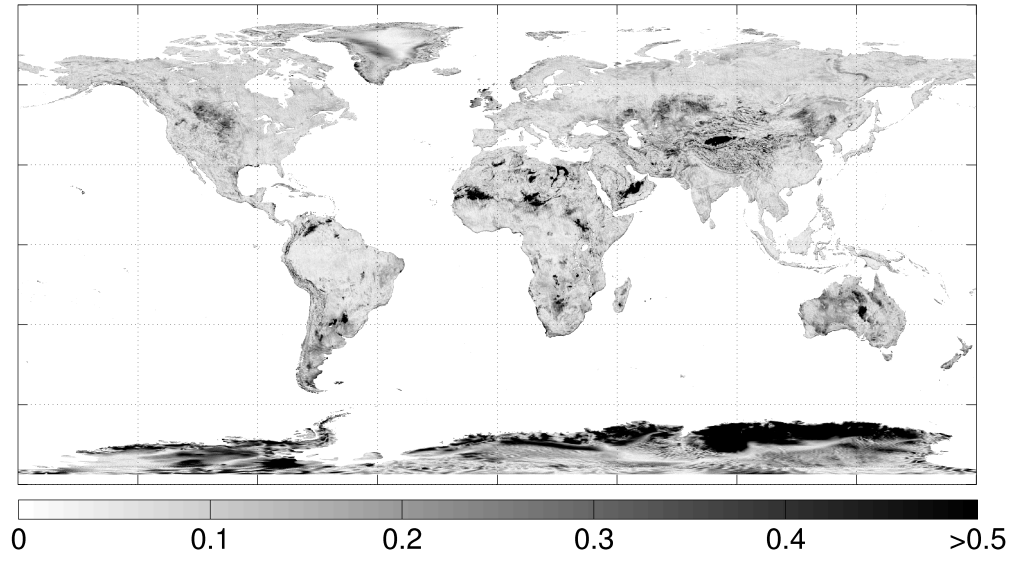
(a)



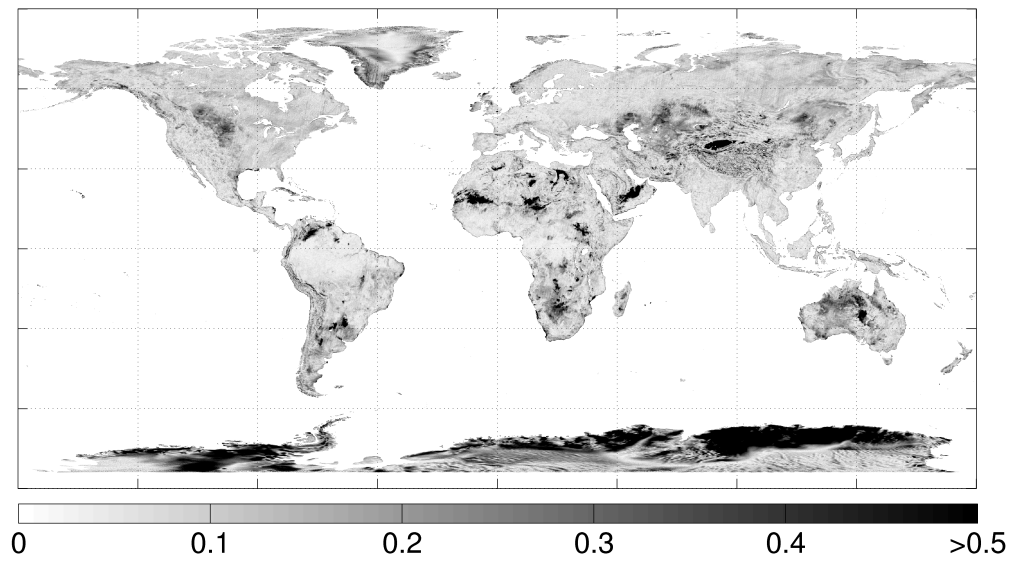
(b)

**Figure A.1:** Standard deviation (in dB) of the azimuth bin means of H-pol (a) ascending and (b) descending data.

mainly in tropical rainforest regions. Due to the approximate six-hour LTD difference between QuikSCAT and OSCAT passes, it is likely that diurnal phenomena contributes to the QuikSCAT/OSCAT relative calibration as well.



(a)



(b)

**Figure A.2:** Standard deviation (in dB) of the azimuth bin means of V-pol (a) ascending and (b) descending data.

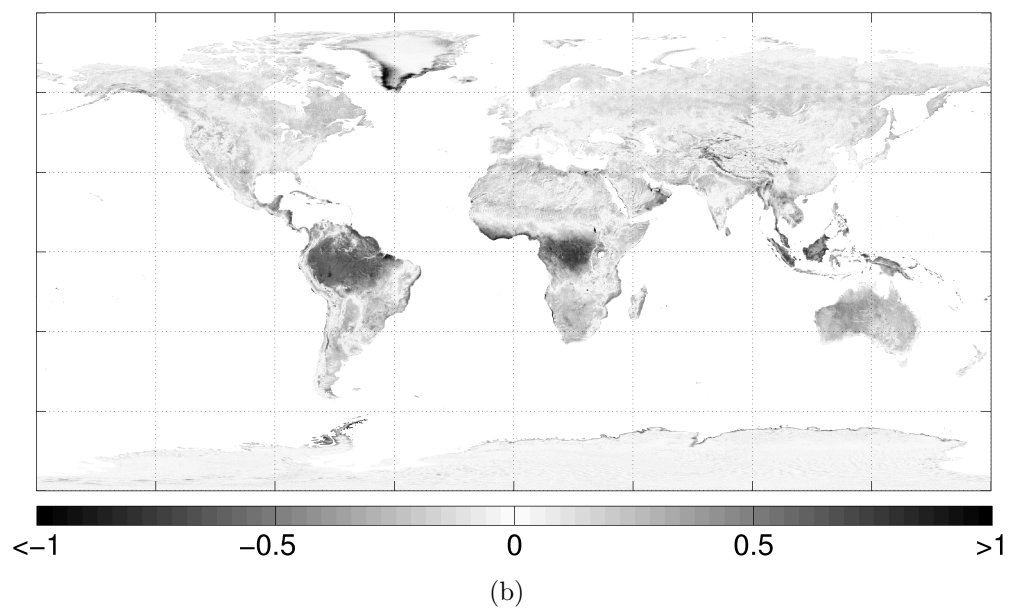
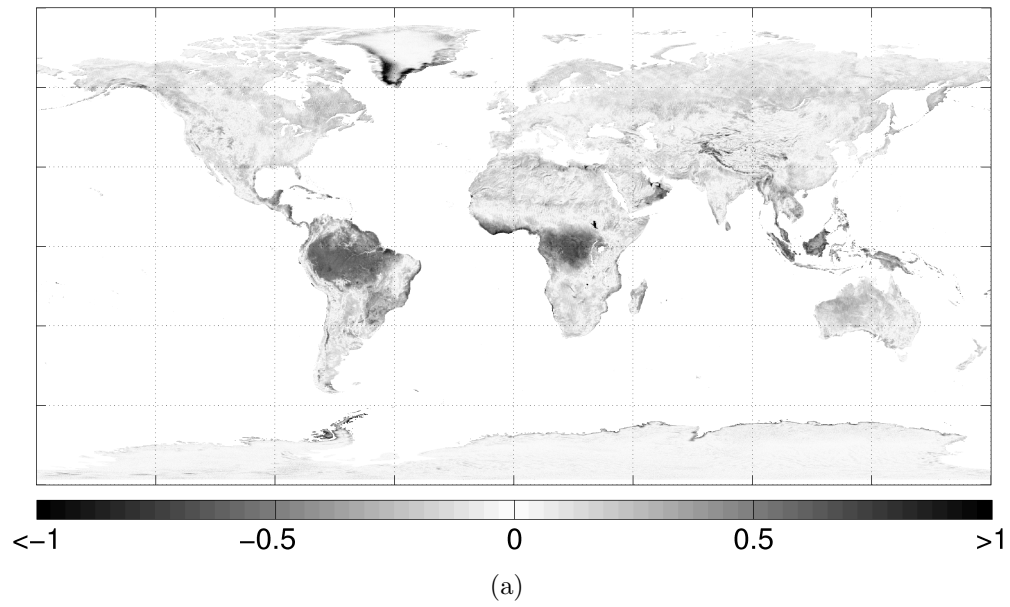


**Figure A.3:** Difference (in dB) of ascending and descending backscatter. (a) H-pol backscatter  
(b) V-pol backscatter.

## Appendix B

### QuikSCAT Azimuth Response

In Chapter 4 we examine the dependence of OSCAT backscatter on antenna azimuth angle over rainforest calibration targets. It is found that the azimuth dependence varies over time and location. It cannot be determined from the data alone if the cause of this variability is due to OSCAT system changes or time-varying inhomogeneities in the calibration targets. In this appendix, we perform a similar analysis of azimuth dependence using QuikSCAT data and note temporal and spatial variation. Assuming that the QuikSCAT system remains stable throughout its mission life, the variability in the azimuth dependence is attributed to the calibration target. This variability is expected in the OSCAT results as well; any additional variability found in the OSCAT azimuth dependence is assumed to be caused by OSCAT system changes.

#### B.1 Temporal and Locational Variability

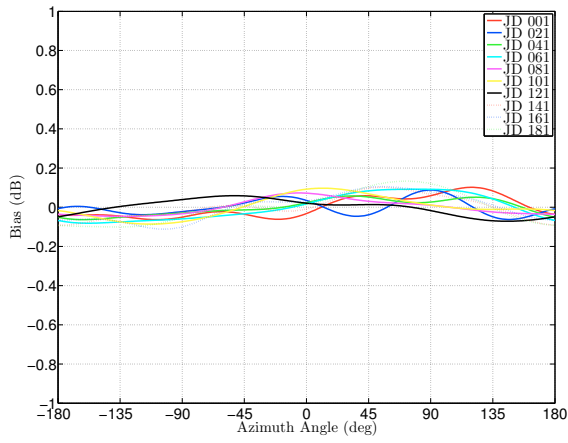
We divide the QuikSCAT data into 20-day intervals and perform a 4<sup>th</sup>-order Fourier series fit. Figure B.1 shows the azimuthal dependence for each interval in 2008 for the East Amazon region. The variability of the curves is typically found to be less than 0.05 dB. Based on our assumption of a well-calibrated QuikSCAT, we attribute this variability to surface changes in the calibration target. The average difference between ascending and descending bias is less than 0.08 dB, indicating that diurnal phenomena over the calibration targets (see Appendix A) do not substantially affect the azimuth dependence.

The inter-annual variability of the azimuthal dependence is examined in Figure B.2, where the Fourier curves of each year's data from 2000-2008 are plotted. The variability of the curves never exceeds 0.02 dB, indicating that both the calibration targets and the QuikSCAT azimuth response remain stable.

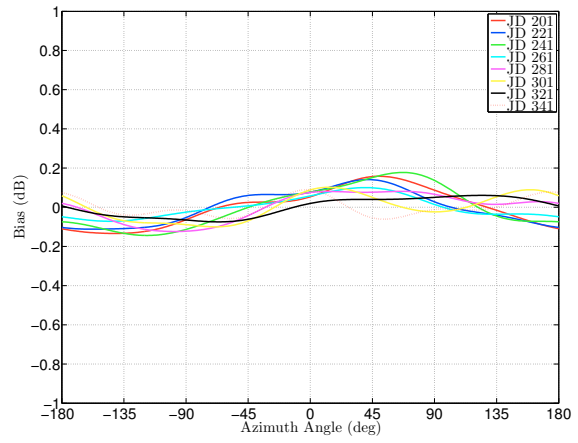
Figure B.3 shows the average azimuthal dependence for all calibration targets for 2008. The maximum difference between region biases does not exceed 0.04 dB. Similar results hold for all other years of QuikSCAT's mission life. This indicates possibly anisotropic differences between calibration targets is relatively small.

#### B.2 Summary

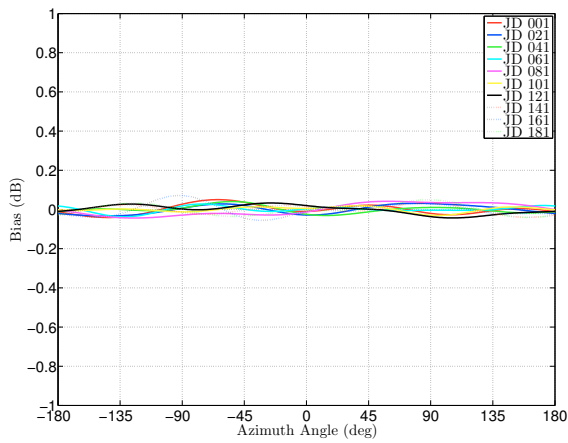
We have shown that the variability of QuikSCAT azimuthal dependence over time and location is small. Assuming that the QuikSCAT system is temporally stable, we attribute the temporal and locational variability to the calibration targets. Any additional variability found in the OSCAT results of Chapter 4 is attributed to system changes.



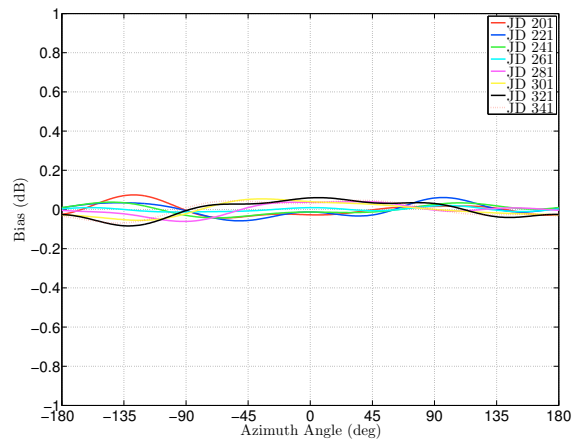
(a)



(b)



(c)



(d)

**Figure B.1:** Azimuth response of QuikSCAT 2008 data for the East Amazon region. (a)-(b) H-pol, ascending. (c)-(d) H-pol, descending.

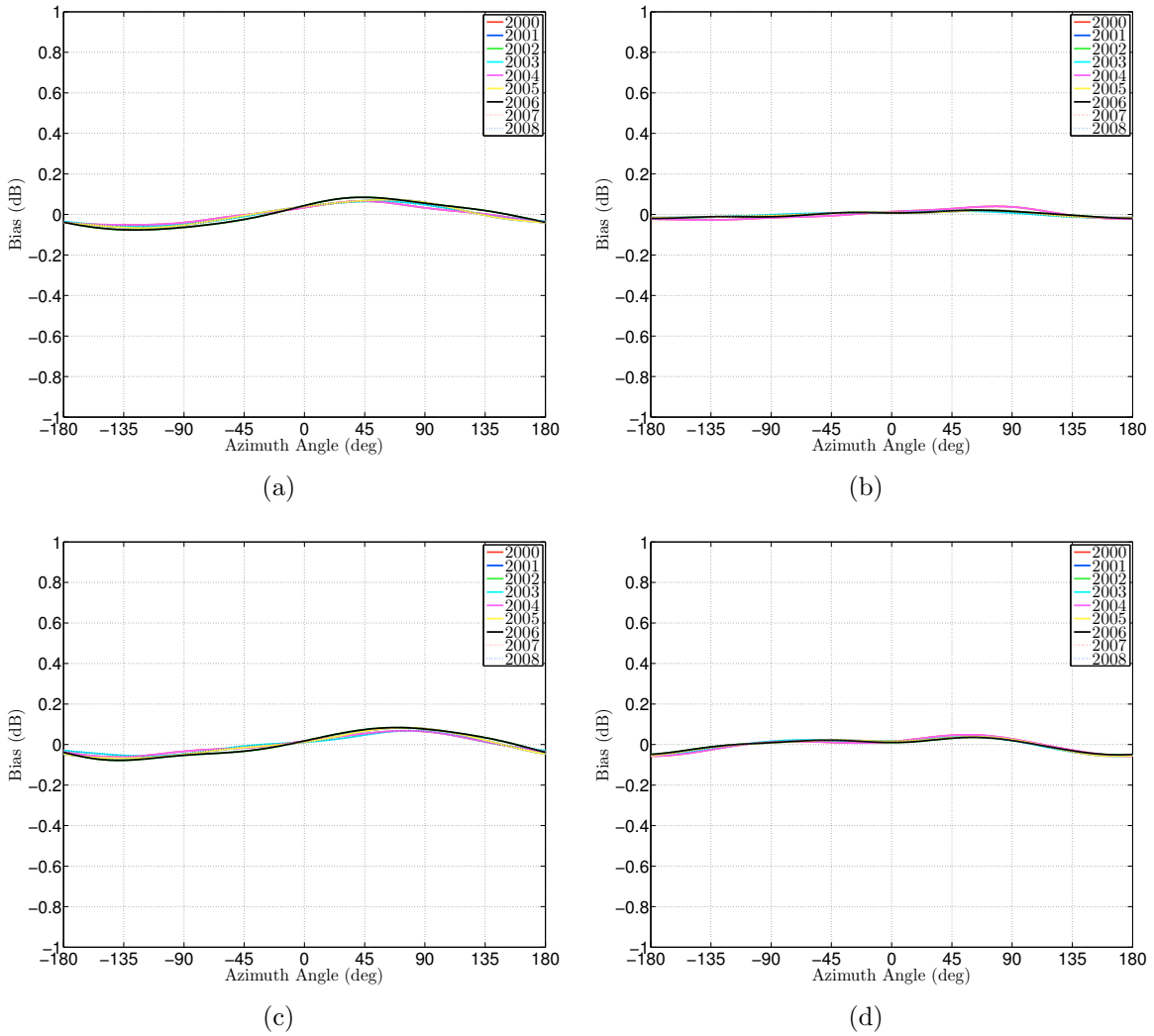


**Figure B.2:** Yearly mean azimuth responses of QuikSCAT 2000-2008 data for the East Amazon region. (a)-(b) H-pol, ascending. (c)-(d) H-pol, descending.

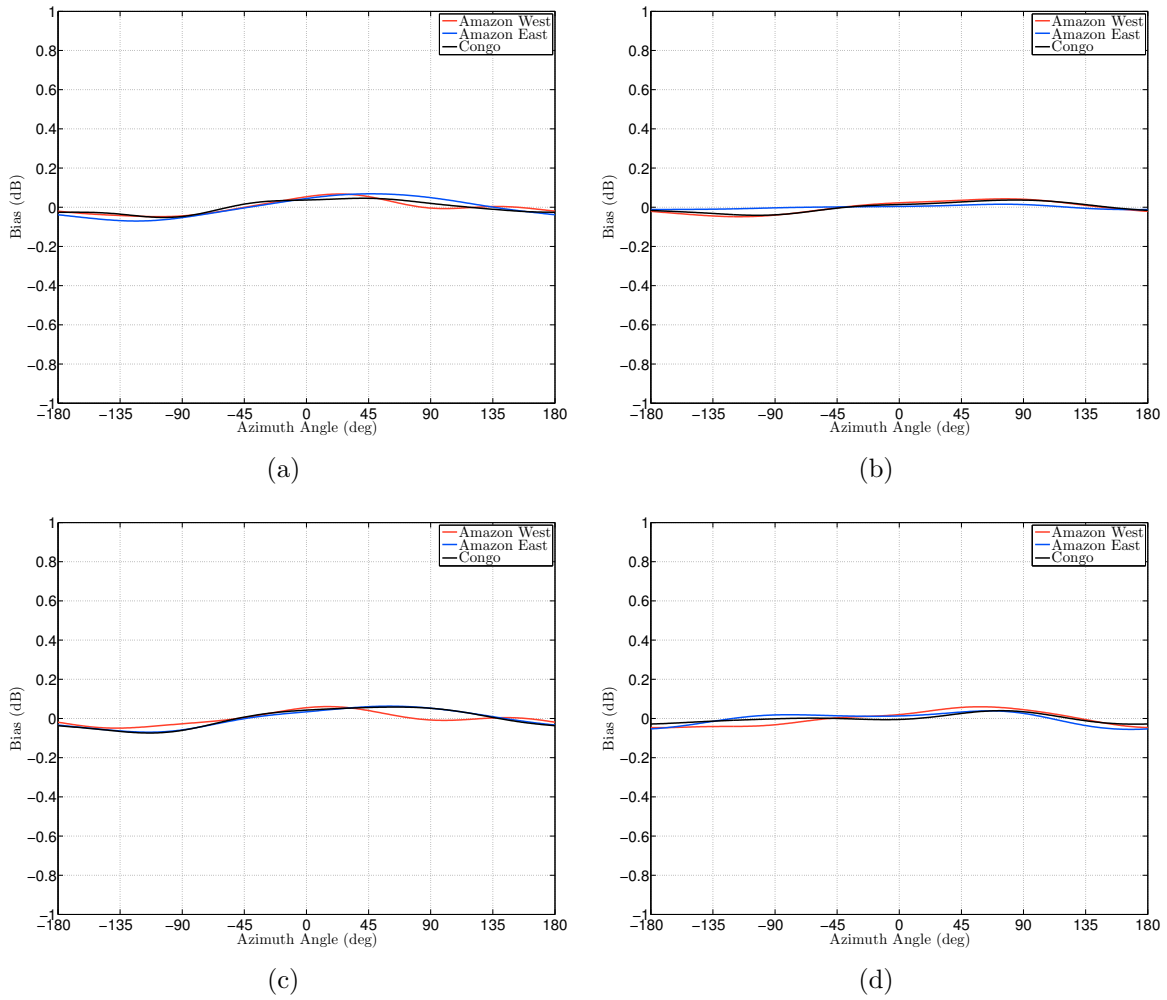


**Figure B.3:** Azimuth response of QuikSCAT 2008 data for all calibration regions. (a) H-pol, ascending, (b) H-pol, descending, (c) V-pol, ascending, (d) V-pol, descending.